Aalto University
School of Science

Master's Programme in Mathematics and Operations Research

Impact of Seismic Source Zones and Maximum Magnitude in Probabilistic Seismic Hazard Analysis in Finland

Eeli Asikainen

Master's Thesis
2026

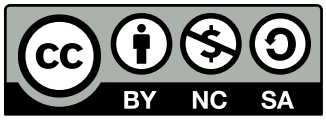

Aalto University
School of Science

Author Eeli Asikainen

Title Impact of Seismic Source Zones and Maximum Magnitude in Probabilistic Seismic Hazard Analysis in Finland

Degree programme Mathematics and Operations Research

Major Systems and Operations Research

Supervisor Prof. Ahti Salo

Advisors M.Sc. (Tech.) Juhana Vehmas, Ph.D. Päivi Mäntyniemi

Collaborative partner Fortum Power and Heat Oy

Date 18 March 2026 **Number of pages** 72+35 **Language** English

Abstract

Nuclear power plants (NPPs) are part of the critical infrastructure of modern society, and the risks associated with them are therefore modelled with particular care. One essential component of this process is probabilistic seismic hazard analysis (PSHA), which is used to estimate the probabilities of earthquake-induced ground motions at the plant site. In regions like Finland, however, significant earthquakes are very rare, which makes their accurate modelling challenging.

This thesis examines, based on previous studies, selected key uncertainties in the seismic hazard assessments for the Loviisa and Olkiluoto NPPs. The work focuses on seismic source zones (SSZs), which describe the spatial distribution of seismicity, and on the maximum magnitude, which defines the largest possible earthquake assumed for the region. The SSZ model and its parameters are updated in line with the model developed in 2025, with particular attention to the Loviisa host zone.

Differences and suitability among the alternative model versions are assessed by analysing the clustering of earthquake observations and by comparing magnitude distributions under different zoning configurations. In addition, the Bayesian probability distribution used to estimate the maximum magnitude is redefined using an updated stable continental region (SCR) earthquake catalogue, in order to obtain more comprehensive data for assessing rare events and to better account for the seismic and geological characteristics of Fennoscandia in the distribution's formulation.

The results show that the delineation of SSZs has substantial and differing effects, particularly on the seismic hazard estimate for Loviisa. Because of the limited data, no single model can be selected justifiably, and therefore alternative zone configurations are proposed to be used in parallel. Updating the maximum magnitude distribution, in turn, reduces the hazard estimates moderately at both plants, as the revised distribution places greater weight on smaller magnitude values.

Keywords Probabilistic seismic hazard analysis, Nuclear safety, Seismic hazard estimate, Seismic source zones, Maximum magnitude, Bayesian modelling, Loviisa, Olkiluoto

Aalto University
School of Science

Tekijä Eeli Asikainen

Työn nimi Seismisten lähdealueiden ja maksimimagnitudin vaikutus todennäköisyysperusteisessa seismisessä hasardianalyysissä Suomessa

Koulutusohjelma Mathematics and Operations Research

Pääaine Systems and Operations Research

Työn valvoja Prof. Ahti Salo

Työn ohjaajat DI Juhana Vehmas, FT Päivi Mäntyniemi

Yhteistyötaho Fortum Power and Heat Oy

Päivämäärä 18.3.2026 **Sivumäärä** 72+35 **Kieli** englanti

Tiivistelmä

Ydinvoimalaitokset ovat osa modernin yhteiskunnan kriittistä infrastruktuuria, ja siksi niihin kohdistuvia riskejä pyritään mallintamaan erityisen huolellisesti. Yksi keskeinen osa tätä kokonaisuutta on todennäköisuusperusteinen seisminen hasardianalyysi (PSHA), jolla arvioidaan maanjäristyksestä aiheutuvien maanliikkeiden todennäköisyyksiä laitosalueella. Suomen kaltaisilla alueilla merkittävät maanjäristykset ovat kuitenkin hyvin harvinaisia, mikä tekee niiden tarkasta mallintamisesta hankalaa.

Tässä diplomityössä tarkastellaan aiempien selvitysten perusteella valittuja merkittäviä epävarmuuksia Loviisan ja Olkiluodon seismisissä hasardiarvioissa. Työssä keskitytään seismisyyden alueellista jakautumista kuvaaviin lähdealueisiin sekä maksimimagnitudiin, joka määrittää alueelle oletetun suurimman mahdollisen maanjäristyksen. Lähdealuejako ja siihen liittyvät parametrit päivitetään vuonna 2025 laaditun mallin mukaiseksi kiinnittäen erityistä huomiota Loviisan lähdealueen erityispiirteisiin.

Eri malliversioiden välisiä eroja ja tarkoituksenmukaisuutta arvioidaan analysoimalla maanjäristyshavaintojen klusteroitumista sekä vertailemalla magnitudijakaumia vaihtoehtoisilla aluejaoilla. Lisäksi maksimimagnitudin estimointiin käytetty bayesiläinen todennäköisyysjakauma uudelleenmääritetään käyttämällä päivitettyä stabiilien manneralueiden (SCR) maanjäristyskatalogia, jotta harvinaisten tapahtumien arviointiin saataisiin aiempaa kattavampi havaintoaineisto ja Fennoskandian seismiset sekä geologiset olosuhteet huomioitaisiin paremmin jakauman muodostamisessa.

Työn tulosten perusteella lähdealueiden määrittämisellä on huomattavia ja erisuuntaisia vaikutuksia etenkin Loviisan seismiseen hasardiarvioon. Aineiston rajallisuuden takia yksittäistä mallia ei voida kuitenkaan perustellusti valita, joten vaihtoehtoisia aluejakoja esitetään käytettäväksi rinnakkain. Maksimimagnitudijakauman päivittäminen puolestaan laskee hasardiarviota maltillisesti molemmilla laitoksilla, sillä uusi jakauma painottuu aiempaa pienempiin magnitudiarvoihin.

Avainsanat Todennäköisyysperusteinen seisminen hasardianalyysi, ydinturvallisuus, seisminen hasardiarvio, seismiset lähdealueet, maksimimagnitudi, bayesiläinen mallintaminen, Loviisa, Olkiluoto

Preface

This thesis was carried out in cooperation with Fortum Power and Heat Oy, Teollisuuden Voima Oyj, and the Institute of Seismology at the University of Helsinki. I am sincerely grateful for the collaboration and for the supportive environment these organizations provided throughout the work.

I would like to express my deepest thanks to my advisors, Juhana Vehmas and Päivi Mäntyniemi, for their guidance, encouragement, and valuable feedback. I am also especially thankful to Jukka Koskenranta, who continued to offer insightful comments and support even while on parental leave. I would further like to thank Johannes Suikkanen for his thoughtful input and discussions, as well as Timo Kukkola and Ilmari Ranta for their participation and contributions during our meetings. Many thanks also to my supervisor, Ahti Salo, for his constructive feedback and for guiding me through the practicalities of completing this work.

Lastly, as this thesis marks the end of my studies at Aalto University, I wish to thank my family and friends for their support through the highs and lows of this unforgettable journey.

Espoo, 18 March 2026

Eeli Asikainen

Contents

Symbols and abbreviations

Symbols

$m_{\max}$	Maximum magnitude
$\mathrm{M_L}$	Local magnitude scale
$\mathrm{M_S}$	Surface-wave magnitude scale
$\mathrm{m_b}$	Body-wave magnitude scale
$\mathrm{M_W}$	Moment magnitude scale
m_i	Magnitude of earthquake i
$\bar{m}$	Mean observed magnitude
$m_{\max}^{\mathrm{obs}}$	Maximum observed magnitude
m^u	Candidate value for $m_{\max}$ in the Bayesian formulation
m_c	Completeness magnitude
$m_{\min}$	Minimum magnitude considered in the PSHA calculations
$n(m)$	Cumulative number of earthquakes with magnitude $\geq m$
N_i	Total number of earthquake recordings in zone i
N^{corr}	Completeness-corrected number of earthquakes
N_c	Number of earthquakes with magnitude $\geq m_c$
t, T	Time interval length
λ	Mean rate of occurrence
a, α	Intercept in the Gutenberg–Richter law, $\alpha = a \cdot \ln(10)$
b, β	Slope in the Gutenberg–Richter law, $\beta = b \cdot \ln(10)$
g	Acceleration of free fall ($\mathrm{g} = 9.81\mathrm{m/s^2}$)
c, C	Ground motion characteristic
$v(C > c)$	Rate of exceedance
$\hat{\mu}$	Sample mean
$\hat{\sigma}$	Sample standard deviation
$d_{\mathrm{obs},i}, d_{\mathrm{exp},i}$	Observed and expected mean nearest neighbour distance of earthquake epicentres in zone i
R_i	Nearest neighbour clustering test statistic of zone i
$D_{n_1 n_2}$	Two-sample K–S test statistic with sample sizes n_1 and n_2
$\mathcal{N}(\mu, \sigma)$	Normal distribution with mean μ and standard deviation σ

Abbreviations

AFE	Annual Frequency of Exceedance
CDF	Cumulative Distribution Function
CI	Confidence Interval
CUVI	Cumulative Visual Inspection
DBE	Design Basis Earthquake
DN	Domain
EPRI	Electric Power Research Institute
FENCAT	Fennoscandian Earthquake Catalogue
GMPE	Ground Motion Prediction Equation
GR	Gutenberg–Richter
ISC	International Seismological Centre
K–S	Kolmogorov–Smirnov
LP	Lower Proterozoic
LS	Least Squares
MLE	Maximum Likelihood Estimation
MP	Middle Proterozoic
NMESE	Non-Mesozoic and Younger Extension
NPP	Nuclear Power Plant
PDF	Probability Density Function
PGA	Peak Ground Acceleration
PSHA	Probabilistic Seismic Hazard Analysis
SA	Spectral Acceleration
SCR	Stable Continental Region
SENSEI	Sensitivity Study of Seismic Hazard Prediction in Finland
SSZ	Seismic Source Zone
STUK	Radiation and Nuclear Safety Authority (Säteilyturvakeskus)
TVO	Teollisuuden Voima Oyj
UH	University of Helsinki
UHRS	Uniform Hazard Response Spectrum

1 Introduction

Ensuring the safe operation of nuclear power plants (NPPs) requires exceptionally high standards of risk management because of the potential of large-scale accidents, which may have prolonged environmental, societal, and economic consequences. Among numerous risks, external hazards—particularly earthquakes—have emerged as significant contributors to overall risk, even in regions of relatively low seismicity such as Finland.

This is also noted by the Radiation and Nuclear Safety Authority (STUK) in their regulatory guide YVL B.7 [1], which outlines the procedure of seismic hazard assessment in Finland. According to the guide, the licensee—that is the organisation or company that holds the legal authorisation to operate a nuclear facility—is responsible for demonstrating that the plant can withstand at least the effects of a design basis earthquake (DBE). This corresponds to a seismic event with an annual frequency of exceedance (AFE) of 10^{-5} at the median confidence level, meaning that the likelihood of experiencing stronger ground motions than the DBE is less than once in 100 000 years.

The effects of the DBE at a nuclear site are modeled with a ground response spectrum, which represents the peak vibrations of idealised single-degree-of-freedom systems across a range of natural frequecies at the base of a structure [2]. However, because of the numerous sources of uncertainty surrounding the modeling of the location and severity of future earthquakes, a probabilistic approach is required in the formulation of this spectrum [3]. Probabilistic seismic hazard analysis (PSHA) is the internationally recognised approach for this purpose and forms the basis for seismic design and safety assessments, including those for nuclear installations.

In Finland, the two operating NPP sites—Loviisa on the southern coast and Olkiluoto on the southwestern coast—undergo regular PSHA updates to reflect new data and evolving scientific understanding. Recent sensitivity studies [4–6] and reviews of Loviisa's seismic hazard assessment [7, 8] have shown that small adjustments in certain model parameters can have profound impacts on the total seismic hazard. Consequently, it is essential not only to apply rigorously justified values for these parameters, but also to maintain a clear understanding of which factors exert the strongest influence on the hazard results. Parameters with high sensitivity must therefore be defensible and based on sound evidence rather than rough estimates.

Recent efforts to enhance PSHA in Finland have focused on refining the most sensitive input parameters. In 2024, Juhana Vehmas' Master's thesis [9] presented new earthquake recurrence parameters based on an updated earthquake catalogue [10]. This revision notably reduced the overall seismic hazard for both NPP sites.

This thesis aims to contribute to the ongoing PSHA development by addressing two of the next most sensitive model details: the maximum magnitude ($m_{\max}$) and the configuration of seismic source zones (SSZs). SSZs define the spatial distribution of seismicity in the region and $m_{\max}$ is a parameter that dictates the largest earthquake

considered within these zones. Choosing which magnitudes to include and how to weight them can significantly shape the hazard curves. However, there is currently no universally approved method for computing a distribution for $m_{\max}$, particularly in low-seismicity regions, which complicates the modeling process.

Similar challenges also affect the definition of the SSZs, where the lack of rigorous rules for zone boundaries has paved the way for the creation of multiple zoning approaches. The zoning model for Finland and its neighboring areas was updated by Mäntyniemi et al. in 2025 [11] based on refined interpretations of regional tectonics and seismicity patterns. From the standpoint of PSHA for NPPs, the definition of seismic source zones often requires periodic re-evaluation, particularly in the vicinity of the site of interest, where the influence of zoning decisions is greatest. This is particularly evident in the Loviisa region, where clustering in the earthquake catalogue intuitively suggests that further subdivision could be justified [4].

The goals of this thesis are to develop and implement a well-justified weighting scheme for $m_{\max}$ for Finland and its neighboring areas and to explore the implications of the updated source zone divisions, with a particular focus on the potential subdivision of the Loviisa source zone. Part of the research also contributes to a broader study by Mäntyniemi et al. [12], which discusses the basis of the Fennoscandian $m_{\max}$ distribution in more detail.

The following chapters present the background, methodology, and findings of this thesis in detail. Chapter 2 introduces the principles of probabilistic seismic hazard analysis and reviews relevant earlier research on the treatment of seismic source zones and maximum magnitude. Chapters 3 and 4 describe the earthquake catalogues and zoning models used in this work, together with the methods employed to incorporate them into the hazard calculations. The results of the modeling and analysis are presented in Chapter 5, including statistical comparisons of the zoning models, the updated maximum magnitude distribution, and the evaluation of hazard sensitivity to these inputs. Finally, Chapter 6 discusses the implications of the findings and suggests areas for future improvements.

2 Probabilistic Seismic Hazard Analysis

PSHA is a methodology developed to quantify the likelihood of various levels of earthquake-induced ground shaking at a specific location over a given time period. Since its inception in the 1960s by Carl Allin Cornell [3], PSHA has become the standard tool for estimating the seismic hazard. This widespread adoption is also reflected in international nuclear safety guidelines [13] that explicitly mandate the use of the method.

The primary goal of PSHA is to integrate knowledge of seismic sources, their recurrence characteristics, and ground motion models to estimate the AFE for different ground motion levels. Unlike deterministic approaches, which consider a single worst-case scenario, PSHA accounts for the full range of possible earthquakes and their probabilities. The results are typically presented as hazard curves, uniform hazard response spectra (UHRS), and graphs showing peak ground acceleration (PGA) or spectral acceleration (SA) for various frequencies. [14]

The UHRS represent the spectral acceleration values at different vibration periods that have the same probability of exceedance. PGA refers to the maximum ground acceleration expected at a site during an earthquake, whereas SA measures the maximum acceleration of a single-degree-of-freedom oscillator at a specific period and damping. The computation of these metrics is usually highly sensitive to the underlying modeling and parameter choices, which can be difficult to validate because of data limitations and the uncertainties related to seismic events [15]. PSHA aims to address this by integrating a multitude of alternative assumptions through the use of logic trees, which help capture this epistemic uncertainty in a structured manner [16].

Despite these and other methodological safeguards, the mathematical and physical validity of PSHA has long been a subject of extensive debate [17]. Critics often point to instances where devastating earthquakes have occurred in regions previously classified as low risk, arguing that such discrepancies reveal fundamental flaws in the methodology [18, 19]. On the other hand, proponents of PSHA emphasise that probabilistic assessments are inherently long-term and that individual events over short time spans are insufficient to invalidate the approach [14]. They also underline that a low seismic hazard estimate does not imply zero risk of large earthquakes. Furthermore, as no alternative methods capable of quantitatively integrating uncertainties into hazard assessment exist, PSHA is likely to remain the dominant framework in seismic hazard assessment for the foreseeable future [17].

2.1 Earthquake Catalogues

As probabilistic hazard estimates rely heavily on historical earthquake records, compiling a comprehensive parametric catalogue is essential. To maintain catalogue quality and avoid overfitting, the data should represent the study region as closely as possible. Before use in hazard calculations, the catalogue must undergo processing to ensure magnitude consistency, event independence, and completeness.

2.1.1 Magnitude Homogenisation

The size and energy release of an earthquake are typically expressed using a magnitude scale. The first widely used scale was introduced by Charles Richter in 1935 [20], commonly known as the Richter scale. Although the name persists in popular culture, the method itself is correctly referred to as the local magnitude scale (M_L). As this term suggests, M_L measures the maximum amplitude of local earthquake seismograms and assigns a magnitude value on a logarithmic scale [21]. However, the original M_L formulation was calibrated for the geological and instrumental conditions of southern California, meaning that its use in other regions requires re-determining several empirical parameters to account for local attenuation characteristics and station corrections. As a result, M_L values determined in different parts of the world are difficult to compare directly [22].

Other scales include the surface-wave magnitude (M_S) and the body-wave magnitude (m_b), originally defined by Beno Gutenberg in 1945 [23, 24], as well as the moment-magnitude scale (M_W) that was introduced by Hanks and Kanamori [25]. The M_S scale measures the amplitude of long-period surface waves that travel along the Earth's surface, making it suitable primarily for shallow earthquakes. In contrast, the m_b scale is based on high-frequency body waves that propagate through the Earth's interior, and it was specifically developed to quantify deep-focus earthquakes, which often generate only weak or poorly observable surface waves.

Although both M_S and m_b are still reported by agencies such as the International Seismological Centre (ISC), M_W remains by far the most preferred alternative in scientific contexts [22]. Unlike the amplitude-based scales, M_W measures the total seismic moment of the earthquake—a physical parameter that does not saturate for large magnitudes or vary depending on the location of the event [25]. Importantly, M_W preserves the logarithmic structure of earlier magnitude scales, and values determined by different methods typically differ by less than one magnitude unit [26].

Hazard assessments require a uniform magnitude measure; therefore, the various scales present in earthquake catalogues are converted to a single scale. This process is known as magnitude homogenisation and it relies on empirical conversion formulas derived from extensive global datasets where events have been recorded using multiple magnitude scales. These relations are relatively straightforward to establish between M_W, M_S, and m_b [26], which are among the most commonly reported magnitudes in global catalogues used, for example, in maximum magnitude assessments.

2.1.2 Declustering and Completeness Assessment

In addition to using a uniform magnitude scale, PSHA commonly assumes that earthquake occurrences follow a stationary Poisson process, meaning that events are independent in time and space and occur at a constant rate [27]. Although this assumption does not fully capture the behaviour of real seismicity—particularly at small magnitudes—it remains the standard framework for large-scale hazard modelling because of the lack of widely adopted alternatives [28].

To meet this assumption when using an empirical earthquake catalogue, dependent events such as foreschocks and aftershocks must be removed through a procedure known as declustering. One of the most widely used declustering algorithm is that of Gardner and Knopoff [29], which applies fixed time and distance windows to identify aftershocks associated with larger mainshock events. Additionally, man-made (i.e., anthropogenic) events such as mining- or industry-related blasts, which may be misclassified as natural earthquakes [30, 31], should be removed to the extent possible.

As large-magnitude events are generally easier to detect than smaller ones, the completeness of the earthquake catalogue must be evaluated to ensure that it provides an unbiased view of seismic activity. Here, completeness refers to the time period during which earthquakes of a given magnitude are assumed to have been consistently recorded. This period varies by region and observation method: instrumental records typically offer better completeness than historical data, but their reliability depends on the density and coverage of the seismic network. Historical records, on the other hand, are prone to observational biases—since they rely on human observations, earthquakes in sparsely populated areas are less likely to be documented, and only the most memorable events tend to be recorded.

Completeness analysis aims to determine the starting year after which earthquakes of a given magnitude are fully reported. Two commonly used approaches are the cumulative visual inspection (CUVI) method [32], as cited in [33, 34], and the method proposed by Stepp in 1972 [35]. Both methods rely on the assumption of stationarity in earthquake rates to graphically assess the completeness for different magnitude groups. Stepp's method evaluates the stability of the standard deviation of the activity rate, while the CUVI method plots the cumulative number of earthquakes against time to identify the point after which earthquakes are observed at a constant rate.

In addition to defining completeness intervals, it is necessary to identify the magnitude above which the catalogue is considered fully complete for those intervals. Even in modern instrumental periods, the smallest earthquakes may remain partially undetected because of network limitations or temporal changes in station coverage. The lower bound, above which all events are assumed to be consistently recorded, is represented by the completeness magnitude (m_c).

As proposed by Wyss et al. [36] and Wiemer and Wyss [37], m_c can be estimated graphically using an approach conceptually similar to the CUVI method: rather than plotting the cumulative number of earthquakes against time, the counts are plotted as a function of magnitude. The point at which the curve departs from linearity marks the threshold for completeness, thereby providing an empirically based estimate of m_c.

2.2 Seismic Source Characterisation

Once sufficient knowledge of past seismic activity has been gathered, individual earthquake sources can be identified and characterised. In regions where active faults are well mapped, this process typically integrates earthquake catalogues with geological and geophysical observations to define fault-based sources. In low-seismicity regions

such as Fennoscandia, however, clear evidence of active faulting is sparse or entirely lacking. As a result, seismic sources are represented as zones within which seismicity is assumed to be spatially uniform [14]. These SSZs are therefore conceptual rather than physical: they provide simplified approximations of one or more sources of seismicity whose precise locations, geometries, or activity patterns cannot yet be determined with sufficient confidence.

An early regional SSZ model for Fennoscandia was developed by Mäntyniemi et al. in 1993 [38], which divided the region into eight subzones based primarily on observed seismicity patterns in the available earthquake data at the time. Since then, the model has undergone several updates and modifications to incorporate new data and adapt to different applications (e.g., [39, 40]). A major improvement was achieved in 2015 through an extensive seismological study conducted for Fennovoima Oy [41]. Compared to earlier efforts, the 2015 SSZ model incorporated much larger seismic, geological, and geophysical datasets that were combined to produce as detailed of a model as possible. The motivation behind this approach was to mitigate the limitations of relying on a single, sparse data type, which is why the same methodology forms the basis for the most recent SSZ models as well [11, 42].

Despite the overall scarcity of seismicity, Fennoscandia exhibits several distinctive patterns that justify detailed zoning. One example is the Vyborg rapakivi granite batholith, which hosts the Loviisa nuclear site and is notable for recurrent swarm-like seismicity that is not observed elsewhere in southern Finland [30, 43–45]. Another example is the narrow belt of low-magnitude earthquake clusters along Sweden's northeastern coastline that clearly distinguishes the area from the surrounding region [11].

However, the main concern with SSZs is whether future seismicity will follow the same spatial patterns inferred from past records. The historical record is inevitably incomplete, and regions with minimal prior activity may still experience damaging earthquakes. An infamous example of this comes from Italy, where in 2002 a school collapsed during an unexpected earthquake (5.7 M_W), which struck the region that was not included in the SSZ model used for building code requirements at the time [46, 47]. Similar surprises have occurred in Canada [48] and Russia [49], where notable earthquakes occurred in regions where available catalogues had suggested only very low levels of seismicity. Even within Fennoscandia, the 1976 Osmussaar earthquake in the Gulf of Finland illustrates this phenomenon: although non-damaging, it occurred outside the pattern suggested by the then-available catalogue and exceeded all previously observed magnitudes in that area [50].

Although intraplate seismicity evolves over long time scales, incidents such as these highlight how abruptly the observable spatial patterns may change. As new earthquakes are recorded and location accuracy is improved with denser seismic stations networks, the identification of seismicity patterns naturally becomes more reliable. Consequently, even in regions like Fennoscandia, it remains important for nuclear safety to continually reassess and validate SSZ models to ensure that they reflect the best available geoscientific knowledge.

2.3 Maximum Magnitude

Another key input in PSHA is the maximum magnitude, which defines the largest earthquake considered physically possible within a given seismic source. Because seismic hazard is evaluated up to $m_{\max}$, specifying this parameter is essential: it sets an upper bound on earthquake size in the calculations and prevents unrealistically large events from contributing to the hazard.

In Cornell's original (1968) formulation of PSHA [3], $m_{\max}$ was not explicitly included, as earthquake magnitudes were assumed to follow an unbounded exponential distribution. Even then, it was recognised that real earthquake sizes might be bounded, but the scarcity of large events made this difficult to demonstrate empirically. Nevertheless, physical reasoning related to fault dimensions and crustal strength has long supported the existence of an upper limit on earthquake size [51].

A defined upper bound was introduced to PSHA only a year later, when Cornell and Vanmarcke [52] proposed a modification to include a maximum magnitude parameter. However, early estimates of $m_{\max}$ were largely intuitive, as systematic and statistically robust estimation techniques had not yet been developed.

Since then, a multitude of different methods for $m_{\max}$ assessment has been proposed, each with its own pros and cons [53]. These approaches are commonly classified into deterministic and probabilistic categories [54]. Deterministic methods link $m_{\max}$ to empirical relationships between earthquake size and fault parameters such as rupture length and area (see, e.g., [55]). By contrast, probabilistic methods estimate $m_{\max}$ purely on the basis of the seismological history of the area, making them appealing in regions like Fennoscandia where information on fault parameters is limited. However, it is well understood that intraplate catalogues would need to span exceptionally long time periods to fully capture the largest potential events [56].

Among probabilistic approaches, two of the most commonly applied are the Kijko method, introduced by Professor Andrzej Kijko in 2004 [54], and the Bayesian method developed in the extensive 1994 study by Johnston et al. [57]. These methods are also used in the present thesis, and a more detailed description of their adaptation is given in Chapter 4. Fundamentally, the Kijko method estimates $m_{\max}$ based on only the observed distribution of earthquakes in a region. It builds on the Gutenberg–Richter (GR) frequency–magnitude relationship (Section 2.4.1) and applies statistical techniques to derive a probabilistic upper bound on earthquake size.

The Bayesian method, on the other hand, combines observed local seismicity with prior information from global or regional analogues. Johnston et al. [57] introduced this approach by developing separate priors for extended and non-extended stable continental crust using geological analogues from the stable continental region (SCR) catalogue, which compiles areas of long-term tectonic stability. This reliance on analogue domains reflects the ergodic principle, in which short local catalogues are supplemented with data from geologically similar regions to compensate for their limited duration.

Because the effectiveness of these methods depends strongly on the regional context, there is no universally preferred approach to maximum magnitude assessment [53]. Vanneste et al. [58] have even suggested that $m_{\max}$ may be similar across all SCRs, given current limitations in constraining regional differences. Nevertheless, this idea has received little attention in PSHA practice, and statistical methods—along with fault-based constraints where available—remain the most widely used approaches for estimating $m_{\max}$.

2.4 Hazard Calculations

The calculation of seismic hazard requires not only identifying the relevant seismic sources and their associated parameters, but also appropriately treating the uncertainties that enter the analysis. Although the physical basis for the distinction is sometimes debated, it has become standard practice in PSHA to divide relevant sources of uncertainty into epistemic uncertainty and aleatory variability [16].

Epistemic uncertainty arises from incomplete scientific knowledge about the true state of the earthquake-generating process, and it can generally be reduced with additional data and improved modelling. In PSHA, this type of uncertainty is typically represented through alternative models or parameter choices that reflect different plausible interpretations of the available information. These alternatives are combined using a logic tree framework, in which each branch corresponds to a specific modelling choice—such as alternative seismic source characterisations or maximum magnitudes. Each branch is also assigned a weight that represents the degree-of-belief in its plausibility, so that more credible alternatives have a proportionally greater influence on the final hazard estimate.

Aleatory variability, on the other hand, represents the natural randomness in earthquake occurrence that cannot be reduced by acquiring additional information. This includes the variability in earthquake recurrence, magnitude, and the resulting ground motion, which must be represented explicitly in the hazard calculations using probability distributions. In the hazard quantification process, these distributions are integrated to yield the annual frequency of exceeding specified ground motion levels at the site.

2.4.1 Earthquake Recurrence

The frequency of earthquakes in a given region is commonly described using the GR relationship, named after its formulation by Gutenberg and Richter in 1944 [59], although a similar expression had already been proposed by Ishimoto and Iida in 1939 [60]. The GR law states that the number of earthquakes with magnitude greater than or equal to m follows the empirical relation

$$\log_{10}(n(m)) = a - bm, \tag{1}$$

where $n(m)$ denotes the cumulative number of events with magnitude $\geq m$, and the parameters a and b are estimated for each seismic source zone. Setting $m = 0$ in

Equation (1) yields the total number of earthquakes 10^a, meaning that parameter a represents the overall seismic activity rate in the zone, while parameter b describes the relative proportion of small to large earthquakes. A high b value indicates a rapid decrease in earthquake frequency with increasing magnitude, whereas a low b value reflects a greater proportion of larger events.

Equation (1) can be expressed equivalently in exponential form

$$n(m) = \exp\{\alpha - \beta m\},$$

with $\alpha = \ln(10)a$ and $\beta = \ln(10)b$. As mentioned before, this formulation does not include any limits on the size of the magnitude range, and thus it ought to be modified to account for the assessed threshold of catalogue completeness and maximum magnitude ($m_{\max}$). These limits can be integrated in the truncated GR distribution

$$n(m) = n(m_c)\frac{\exp\{-\beta(m - m_c)\} - \exp\{-\beta(m_{\max} - m_c)\}}{1 - \exp\{-\beta(m_{\max} - m_c)\}}. \tag{2}$$

It is worth noting that although some approaches to estimating $m_{\max}$—such as the Kijko method discussed earlier—use this truncated distribution while simultaneously solving for the value of $m_{\max}$ that appears within it, this does not pose a practical difficulty. It has been shown that the estimation of the GR parameters a and b is not particularly sensitive to the exact value of $m_{\max}$ [6, 61]. Thus, the parameters may be estimated initially using the maximum observed magnitude ($m_{\max}^{\text{obs}}$) as a proxy, after which they can be used to derive a more accurate estimate of the maximum magnitude.

Estimating the recurrence parameters is an essential component of PSHA, as they determine the expected rates of earthquakes of different magnitudes. Numerous techniques for estimating the GR parameters have been proposed, with maximum likelihood estimation (MLE) and least squares (LS) regression being the most commonly used in PSHA applications [59, 62]. MLE identifies the parameters that maximise the likelihood of observing the catalogue under a Poissonian distribution, while LS regression provides an alternative estimate by minimising the error in the log-linear GR relation. MLE is generally preferred because it provides unbiased estimates when working with truncated or incomplete catalogues, but nevertheless the LS method is also occasionally used [63].

2.4.2 Ground Motion Prediction Equations

Ground motion prediction equations (GMPEs) provide a quantitative relationship between earthquake source parameters, local site conditions, and the resulting ground shaking at a site [64]. Within PSHA, GMPEs are used to estimate the probability distribution of a chosen ground motion intensity measure—typically PGA or SA—conditional on the occurrence of an earthquake with magnitude m at distance r from the site.

Rather than yielding a single deterministic value, GMPEs provide the likelihood that the ground motion parameter exceeds a specified level c, expressed as $P(C > c \mid m, r)$.

This probability increases with earthquake magnitude and decreases with source-to-site distance, reflecting the general physical behavior that larger and closer earthquakes tend to produce stronger shaking.

In regions with abundant data on strong ground motions, GMPEs are developed directly from local recordings. However, in stable intraplate regions such as Fennoscandia, the limited availability of seismic data poses significant challenges for locally calibrated GMPE development. As a result, Finnish PSHAs have relied on modifying existing models that have been developed for tectonically analogous regions with more extensive datasets [65, 66].

2.4.3 Hazard Quantification

After the seismic sources, their associated seismicity parameters, and GMPEs have been defined, the contribution of each source to the seismic hazard at a site can be quantified. For a single seismic source, the annual frequency of exceeding a ground motion level c is obtained by integrating over all relevant magnitudes and source-to-site distances. This is expressed as

$$\nu(C > c) = n_{\min} \int_{m_{\min}}^{m_{\max}} \int_{r_{\min}}^{r_{\max}} P(C > c \mid m, r)\, f_M(m)\, f_R(r)\, \mathrm{d}r\, \mathrm{d}m, \tag{3}$$

where $P(C > c \mid m, r)$ is given by the selected GMPE, $n_{\min}$ is the recurrence rate of earthquakes with magnitude greater than $m_{\min}$, and $f_M(m)$ and $f_R(r)$ are the probability density functions (PDFs) for magnitude and distance, respectively. In the case of SSZs, $n_{\min}$ is further normalised by the area of the zone, and the distance distribution $f_R(r)$ is determined directly from the geometry and relative position of the SSZ with respect to the site.

Additionally, the magnitude distribution is assumed to follow the truncated GR model in Equation (2), with PDF

$$f_M(m) = \frac{\beta \exp\{-\beta(m - m_{\min})\}}{1 - \exp\{-\beta(m_{\max} - m_{\min})\}},$$

where $m_{\min}$ and $m_{\max}$ correspond to the magnitude limits in Equation (3). It is important to note that $m_{\min}$ is not the same as the catalogue completeness threshold m_c used to estimate the GR parameters. Instead, $m_{\min}$ is a modeling choice in the hazard calculation: earthquakes smaller than $m_{\min}$ are excluded because they are assumed to be incapable of producing ground motions that could harm the NPP. Typical values of $m_{\min}$ range from 4.0 to 5.0 $\mathrm{M_W}$ [67].

In practice, Equation (3) is solved numerically by discretising the magnitude and distance integrals. When multiple seismic sources contribute to the hazard, the total AFE is computed by summing the exceedance rates from all sources. The quantity $\nu(C > c)$ is then evaluated for different intensity levels c to construct the seismic hazard curve, which expresses the annual frequency of exceeding a given ground motion level.

3 Data and Models

To enable the sensitivity assessment of different modelling choices, this chapter first introduces the datasets and representations of seismicity on which the analyses are based, and then outlines how each is used in the subsequent steps of the PSHA calculations. The Fennoscandian SSZ models adopted in this work are evaluated using the Fennoscandian catalogue, which forms the basis for the regional seismicity modelled in the hazard calculations. In parallel, Bayesian maximum magnitude estimates rely on a broader SCR catalogue to complement the limited high-magnitude information available within the regional dataset.

3.1 Fennoscandian Earthquake Catalogue

The Fennoscandian earthquake catalogue (FENCAT; updated after Ahjos and Uski, 1992 [68]) is an open-access database maintained by the Institute of Seismology at UH. It provides all available non-instrumental and instrumental earthquake records in Fennoscandia and adjacent offshore areas, using data from earthquake bulletins provided by several institutions. Each catalog entry includes information on event time, location, depth, magnitude, intensity, and data sources. To the extent possible, the dataset has been cleaned of non-seismic events such as explosions, induced events, and frost-related occurrences. [69]

Since its initial release, FENCAT has undergone several updates, resulting in multiple published versions. In this thesis, two declustered versions of the catalogue are used: a publicly available subcatalogue of FENCAT17 [70] and an unpublished version of the FENCAT(2021) catalogue [10]. The former is used exclusively for comparing alternative SSZ models, since it was compiled with particular attention to earthquake swarms, to which statistical comparisons are especially sensitive. The latter serves as the primary dataset for the hazard calculations, as it contains the most recent seismicity information available. Both catalogues provide homogenised magnitudes, in which the originally reported magnitude scales have been converted to moment magnitudes, which are used throughout this thesis.

FENCAT17

The FENCAT17 dataset, published in 2024, is an updated version of the Fennoscandian earthquake catalogue that covers earthquakes from 1467 to the end of 2017 within an area bounded by 46–86°N latitudes and 0–60°E longitudes. Compared to its predecessors, FENCAT17 incorporates several enhancements, including homogenised magnitude estimates and improved event characterisation. [70]

Additionally, the FENCAT17 dataset includes several subcatalogues that have been developed for specific applications. The dataset used in this thesis is the declustered subcatalogue FENCAT17_Seismic_Risk [70], hereafter referred to as FENCAT17. This version includes 16 624 events which have been filtered from the full dataset of 20 406 observations by removing dependent events, such as fore- and aftershocks.

Declustering was performed using a windowing algorithm based on the method of Gardner and Knopoff [29], which was also used to identify swarm events present in the region. Additionally, for the purposes of this thesis, 626 events with reported moment magnitudes less than or equal to zero were removed.

FENCAT21

As of early 2026, FENCAT(2021) is the most recent version of the Fennoscandian earthquake catalogue that extends the previous FENCAT17 by including events from 2018–2021. The current official release, FENCAT(2021)_update [69], incorporates formatting changes and minor error corrections compared to the first release.

However, for consistency with Vehmas' work [9], this thesis employs an unpublished version of the catalogue [10], referred to here as FENCAT21. The differences between the unpublished and official versions are relatively minor as the updating and processing steps, which have been described in detail by Uski et al. [31], are mostly identical.

One notable difference between the different versions of FENCAT(2021) is that the unpublished version includes events from 2017–2021 only for areas corresponding to the 2025 micro-level SSZs within a 300 km radius of the target NPPs (Section 3.2.1), whereas the official version covers the whole study area bounded by 54–75°N latitudes and 0–45°E longitudes. For observations prior to 2017, the unpublished version appears to use the slightly larger study region defined for FENCAT17. This explains the sudden drop in the number of earthquakes after 2017 in the FENCAT21 dataset, as shown in Figure 1.

Another key distinction is that the official FENCAT(2021) version has not been declustered, making it unsuitable for hazard calculations [13, 14]. As mentioned in Vehmas' thesis, the unpublished FENCAT21 was declustered using the same principles as the previously discussed FENCAT17 dataset, although less attention was given to filtering specific earthquake swarms. Consequently, FENCAT17 removed substantially more observations during declustering. After declustering, the FENCAT21 had 591 events removed, while the declustering process implemented for FENCAT17 eliminated 3 782 events. Additional filtering excluded 592 events without a homogenised magnitude and 149 events with homogenised magnitude equal or smaller than zero, resulting in a final dataset of 20 791 events for FENCAT21.

The differences between the FENCAT21 and FENCAT17 are illustrated in Figure 1. The catalogues differ most clearly in 2007, 2008, and 2015, primarily because of low-magnitude events ($M_W < 2.0$) in offshore Norway and the Norwegian Sea, which do not influence the seismic hazard of Finnish NPPs. Nonetheless, some additional clustering is visible in Kymenlaakso and along the western coast of Sweden; these may affect the statistical tests used when comparing modelling approaches (Section 4.2), although their impact on the final hazard estimates is expected to be minor.

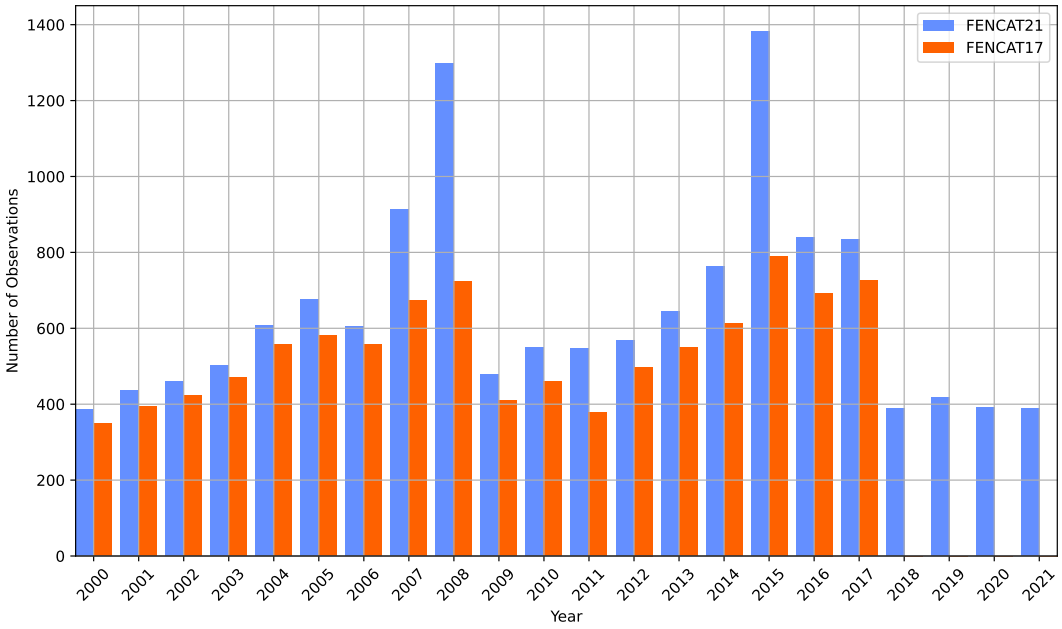

Figure 1: Number of earthquake observations by year in the different declustered FENCAT datasets in the 21st century.

3.2 Seismic Source Zone Models for Fennoscandia

Seismic source zones represent regions within which earthquakes are assumed to occur with equal likelihood, based on shared geological, tectonic, and seismological characteristics. In PSHA, these zones are used to define the spatial distribution of potential earthquake sources and to estimate regional recurrence parameters.

Two generations of SSZ models are considered in this thesis:

- The 2016 SSZ model, introduced and described by Korja et al. [42], which has served as the reference configuration in previous studies, including Vehmas [9].
- The 2025 SSZ models, presented by Mäntyniemi et al. [11], which incorporate updated seismicity data and refined geological interpretations to produce multiple zoning alternatives at different levels of detail.

The following subsections describe these models in more detail, summarise their key characteristics, and discuss their implications for site-specific hazard assessments at the Olkiluoto and Loviisa NPPs.

3.2.1 Summary of the Models

The SSZ model described in the 2016 seismological study [42] was designed in a cooperative project by the Institute of Seismology at UH, Geological Survey of Finland, Geological Survey of Estonia, Geological Survey of Sweden and University of Uppsala. The project produced two alternative SSZ models: in the first model, zone

6 is treated as a single unit, while in the second it is subdivided into three smaller zones (6a, 6b, 6c), as shown in Figure 2. In this thesis, both configurations are collectively referred to as the 2016 SSZ model, and only the zones that are located within a 300 km radius of the target nuclear sites are considered, following international nuclear safety guidelines [13, 71]. Following the approach adopted by Vehmas [9], both versions are given equal 50 % weight in hazard calculations.

The 2025 SSZ models were also developed through a collaborative effort, this time involving 29 geoscientists from Finland, Estonia, Norway, Russia, and Sweden [11]. The work resulted in four alternative SSZ delineations for the Fennoscandian region, each representing a different level of detail. The models are categorised as micro, meso, and macro, with the micro-level model having two versions. However, since the differences between the two micro-level versions occur outside the 300 km radii of the target nuclear sites, only one version is considered in this thesis. Additionally, the macro-level model is excluded because its broad zoning was considered unsuitable for detailed hazard analysis by engineers at Fortum and Teollisuuden Voima (TVO).

The formulation process of the different 2025 models is described in detail by Mäntyniemi et al. [11]. The models were based on the original FENCAT17 dataset [69] and supplemented with extensive geological and geophysical data. These inputs were used to refine pre-existing models, such as the 2016 SSZ model, to better reflect recent seismicity patterns. The differences between the 2016 SSZ model and the 2025 micro model are illustrated in Figure 2, while the meso model is shown in Figure 3. The zones in the 2025 models are named according to their geographical location (e.g., FI-C for Central Finland).

According to Mäntyniemi et al. [11], these seismic zoning models provide a robust basis for seismic hazard mapping at national and regional scales. However, they recommend further investigations if the model is to be applied to site-specific PSHAs targeting extremely low-probability earthquakes. For this reason, particular emphasis is placed on the source zones closest to the sites in this work.

Table 1 summarises the SSZ-specific earthquake statistics for the adopted FENCAT datasets for all the SSZ models. The micro-level zones show values reasonably close to their 2016 counterparts, while the larger areas of the meso-level zones result in a significantly higher number of included earthquakes. Nevertheless, these results slightly underestimate the actual number of recorded events for the meso-level model, as the used FENCAT21 version does not include the most recent data for the entire model area.

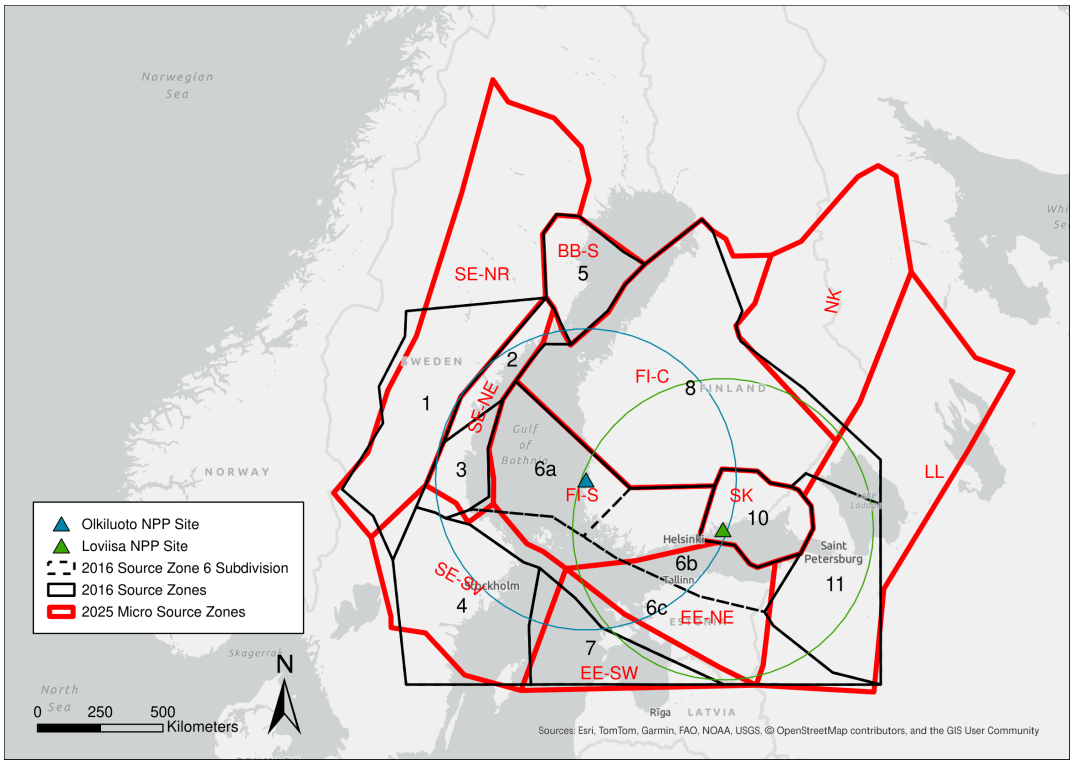

Figure 2: SSZ delineation according to the 2025 micro model compared to the 2016 SSZs. The circles indicate the 300 km radii around the NPP sites.

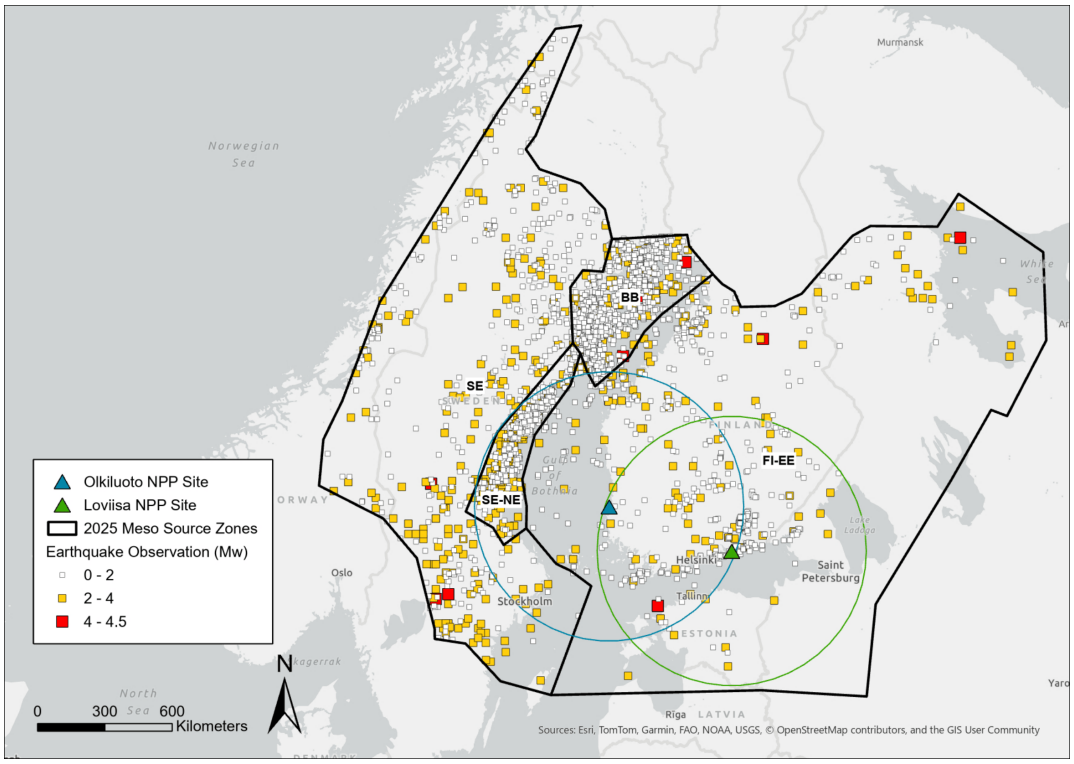

Figure 3: SSZ delineation of the 2025 meso model. Seismicity from 1467 to 2021 is shown, and the circles indicate the 300 km radii around the NPP sites.

Table 1: SSZ-specific number of events (N), mean observed magnitude ($\bar{m}$), and maximum observed magnitude ($m_{\max}^{\text{obs}}$) in each of the adopted FENCAT datasets. The SSZs correspond to the 2016 model and the 2025 micro and meso models.

	FENCAT17			FENCAT21		
SSZ	N	$\bar{m}$ (M_W)	$m_{\max}^{\text{obs}}$ (M_W)	N	$\bar{m}$ (M_W)	$m_{\max}^{\text{obs}}$ (M_W)
1	106	2.03	4.2	123	1.96	4.2
2	263	1.68	3.9	332	1.60	3.9
3	173	1.98	3.6	189	1.95	3.6
4	106	2.23	4.5	116	2.16	4.5
5	768	1.39	4.1	1111	1.25	4.4
6 (whole)	84	1.81	4.4	123	1.58	4.4
6a	23	1.58	2.9	37	1.44	2.9
6b	33	1.71	3.6	50	1.41	3.6
6c	28	2.11	4.4	36	1.97	4.4
7	2	1.85	2.6	2	1.85	2.6
8	207	1.49	4.0	283	1.31	4.0
10	86	1.13	2.9	314	0.86	2.9
11	1	2.2	2.2	2	2.15	2.2
All (2016)	**1796**	**1.59**	**4.5**	**2595**	**1.40**	**4.5**
SE-NR	222	1.82	4.2	267	1.72	4.2
SE-NE	424	1.80	3.9	508	1.73	3.9
SE-SV	111	2.19	4.5	124	2.12	4.5
BB-S	773	1.39	4.2	1118	1.25	4.2
FI-S	64	1.69	3.6	94	1.49	3.6
EE-NE	17	2.24	4.4	25	1.88	4.4
EE-SW	1	2.6	2.6	1	2.6	2.6
FI-C	222	1.55	4.1	297	1.36	4.1
SK	86	1.13	2.9	314	0.86	2.9
LL	2	2.2	2.2	4	2.05	2.2
NK	20	1.54	3.1	30	1.44	3.1
All (micro)	**1942**	**1.60**	**4.5**	**2782**	**1.41**	**4.5**
SE	465	1.90	4.5	535	1.82	4.5
SE-NE	424	1.80	3.9	508	1.73	3.9
BB	1159	1.38	4.2	1649	1.24	4.2
FI-EE	434	1.56	4.4	791	1.23	4.4
All (meso)	**2482**	**1.58**	**4.5**	**3483**	**1.40**	**4.5**

3.2.2 Characterisation Parameters

In addition to defining the source-to-site distance associated with seismic activity, SSZs also represent the expected depth range within the Earth's crust where earthquakes may originate. This requires specifying the seismogenic thickness and faulting characteristics for each zone. Because the exact source location is often uncertain, these parameters are typically expressed as distributions.

The characterisation parameters have been defined for the 2016 SSZ model in Loviisa's 2021 PSHA [65], and they were used without modification in Vehmas' 2024 thesis [9]. As no updated parameters have yet been developed for the 2025 SSZ models, the present work applies the same parameter distributions by mapping each new SSZ to the 2016 zones with which it most strongly overlaps. In cases where a new zone spans multiple 2016 SSZs—such as the SE-NE zone—the more conservative distribution (i.e., the one corresponding to shallower depths) was selected.

Although Vehmas demonstrated that the fault-plane dip and fault-type parameters have no influence on the resulting hazard estimate, they are retained here for the sake of completeness. The final characterisation parameters used for the 2025 meso and micro models are summarised in Tables 2 and 3, respectively.

Table 2: Seismogenic thicknesses, fault plane dips, fault types and depth distributions for the 2025 meso SSZ model.

2025 Meso SSZ	**Seismogenic Thickness (km) [weight]**	**Fault Plane Dip (° from horizontal) [weight]**	**Fault Type**	**Focal Depth Triangular (km) [parameter]**
SE-NE	22 [0.2] 26 [0.6] 30 [0.2]	80 [0.3] 85 [0.3] 90 [0.4]	Strike-slip	0 [lower] 18 [mode] 30 [upper]
SE	21 [0.2] 26 [0.6] 31 [0.2]	80 [0.3] 85 [0.3] 90 [0.4]	Strike-slip	0 [lower] 18 [mode] 31 [upper]
BB	25 [0.2] 28 [0.6] 31 [0.2]	80 [0.3] 85 [0.3] 90 [0.4]	Strike-slip	0 [lower] 20 [mode] 31 [upper]
FI-EE	18 [0.2] 23 [0.6] 28 [0.2]	80 [0.3] 85 [0.3] 90 [0.6]	Reverse	0 [lower] 15 [mode] 28 [upper]

Table 3: Seismogenic thicknesses, fault plane dips, fault types and depth distributions for the 2016 and 2025 micro SSZ models.

2016 SSZ	2025 Micro SSZ	Seismogenic Thickness (km) [weight]	Fault Plane Dip (° from horizontal) [weight]	Fault Type	Focal Depth Triangular (km) [parameter]
1	SE-NR	25 [0.2] 30 [0.6] 35 [0.2]	80 [0.3] 85 [0.3] 90 [0.4]	Strike-slip	0 [lower] 23 [mode] 35 [upper]
2	SE-NE	22 [0.2] 26 [0.6] 30 [0.2]	80 [0.3] 85 [0.3] 90 [0.4]	Strike-slip	0 [lower] 18 [mode] 30 [upper]
3	–	22 [0.2] 27 [0.6] 32 [0.2]	80 [0.3] 85 [0.3] 90 [0.4]	Strike-slip	0 [lower] 18 [mode] 32 [upper]
4	SE-SV	21 [0.2] 26 [0.6] 31 [0.2]	80 [0.3] 85 [0.3] 90 [0.4]	Strike-slip	0 [lower] 18 [mode] 31 [upper]
5	BB-S	25 [0.2] 28 [0.6] 31 [0.2]	80 [0.3] 85 [0.3] 90 [0.4]	Strike-slip	0 [lower] 20 [mode] 31 [upper]
6	FI-S, EE-NE	18 [0.2] 23 [0.6] 28 [0.2]	70 [0.2] 80 [0.2] 90 [0.6]	Reverse	0 [lower] 15 [mode] 28 [upper]
7	EE-SW	18 [0.2] 23 [0.6] 28 [0.2]	80 [0.3] 85 [0.3] 90 [0.4]	Strike-slip	0 [lower] 15 [mode] 28 [upper]
8	FI-C, NK	19 [0.2] 25 [0.6] 30 [0.2]	80 [0.3] 85 [0.3] 90 [0.4]	Strike-slip	0 [lower] 17 [mode] 30 [upper]
10	SK	18 [0.2] 23 [0.6] 28 [0.2]	80 [0.3] 85 [0.3] 90 [0.4]	Reverse	0 [lower] 15 [mode] 28 [upper]
11	LL	18 [0.2] 23 [0.6] 28 [0.2]	80 [0.3] 85 [0.3] 90 [0.4]	Strike-slip	0 [lower] 15 [mode] 28 [upper]

3.2.3 Characteristics of the Source Zone for Loviisa

The 2023 sensitivity study of seismic hazard prediction in Finland (SENSEI) [4], together with earlier studies [72, 73], highlighted that the seismicity within the host source zone of Loviisa (SSZ 10 in the 2016 model and SK in the 2025 micro model) is spatially non-uniform. Indeed, as shown in Figure 4, earthquake activity is heavily concentrated in the western part of the zone. This may suggest that earthquakes do not occur with equal likelihood throughout the zone, which would be a violation of the fundamental assumption of a seismic source zone.

The SENSEI project investigated this issue and introduced three alternative subdivisions that separate the more active western area from the less active eastern area, thereby localising the seismicity into a smaller area. A simplified PSHA demonstrated that introducing any of these subdivisions would substantially increase the hazard at Loviisa, even with relatively small branch weights in the logic tree. However, while the need to account for such subdivisions has been assessed, these evaluations have not previously led to their inclusion in Loviisa's full PSHA model [72, 73].

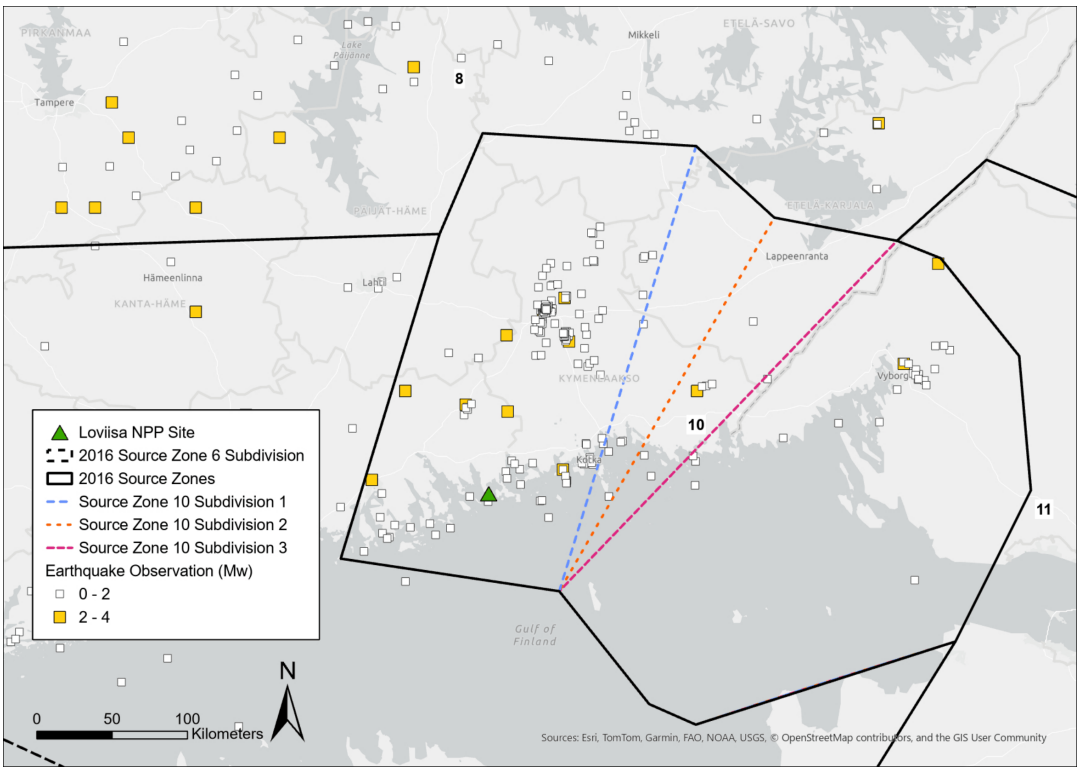

Figure 4: The three proposed subdivisions of the source zone 10. The earthquake observations are from FENCAT21 [10].

Despite the observed spatial clustering, previous studies [4, 72, 73] have ultimately concluded that there is currently no geophysical or geological evidence to support the belief that the SSZ should be treated as separate zones, and geologically the area is well-defined by the Vyborg rapakivi granite batholith [41]. Koskenranta [73] also noted that the limited amount of data, together with the influence of earthquake sequences, prevents demonstrating any statistically significant difference between the proposed subareas. Furthermore, Mäntyniemi et al. [72] highlighted that reporting differences across the Finland–Russia border may influence catalogue completeness, potentially contributing to the east–west contrast in observed seismicity. Nonetheless, it has been recognised that new data may justify re-evaluating the zone's boundaries, and recent observations provide an opportunity to revisit the question.

3.3 Updated Global SCR Earthquake Catalogue

The 2012 Electric Power Research Institute (EPRI) SCR database was updated during this work to support the present analysis as well as the broader study by Mäntyniemi et al. [12], from which the geologically comparable analogue domains used in this thesis were adopted. The original EPRI catalogue was expanded by integrating data for these selected domains retrieved from the Reviewed Bulletin of the ISC. This process involved magnitude harmonisation, removal of duplicate events, and recalculation of domain-level parameters to ensure consistency with the EPRI methodology. The resulting updated dataset is publicly available on GitHub [74].

3.3.1 2012 EPRI SCR Catalogue

The 2012 EPRI SCR Catalogue (Appendix K.1 of [75]), hereafter referred to as the EPRI catalogue, is a global earthquake dataset covering events from the year 495 CE until the end of 2008 that have been gathered from non-instrumental and instrumental records. Developed as part of the EPRI seismic hazard assessment project, the catalog organises earthquake observations into geological domains representing stable continental crust. Each domain corresponds to a tectonic block or region characterised by similar geological age and structural properties.

The catalogue is an updated version of the SCR catalog compiled by Schulte and Mooney [76], which itself was an extension of the original dataset developed by Johnston et al. [57]. The Johnston et al. catalog was based on regional and global earthquake catalogs and historical sources, covering events up to 1990. Schulte and Mooney extended this dataset to 2003 using instrumental data and incorporated additional pre-1990 events identified in later literature. In 2012, EPRI further updated the catalogue by adding a modest number of earthquakes occurring between 2004 and 2008 that were recorded in the Harvard Moment Tensor catalog. Additionally, EPRI assigned an expected moment magnitude $E[\mathrm{M}]$ to all events and updated magnitude uncertainties $\sigma[\mathrm{M}]$, as detailed their report [75].

The definition of domains was directly adopted from Johnston et al., along with domain-specific parameters such as area, geological age, and completeness intervals. In the Bayesian approach for maximum magnitude assessment, these domains also serve as the basis for identifying geological analogues that expand the available dataset for the target region. In this thesis, analogues for Fennoscandia were selected based on geological age, which has been strongly linked to $m_{\max}$ in previous research [75].

Based on the classification by Mäntyniemi et al. [12], the age groups most similar to Fennoscandia are Archean, Lower Proterozoic (LP), and Middle Proterozoic (MP). The Archean and LP domains broadly correspond to the age of the Fennoscandian Shield, whereas the MP domains are comparable to crustal areas in south–western Sweden and large parts of Norway. Accordingly, domains belonging to these groups were selected as analogues for constructing a prior for the entire Fennoscandian region. The initially selected domains are illustrated in Figure 5, while the 49 domains containing observed events in the final catalogue are listed in detail in Appendix A.2.

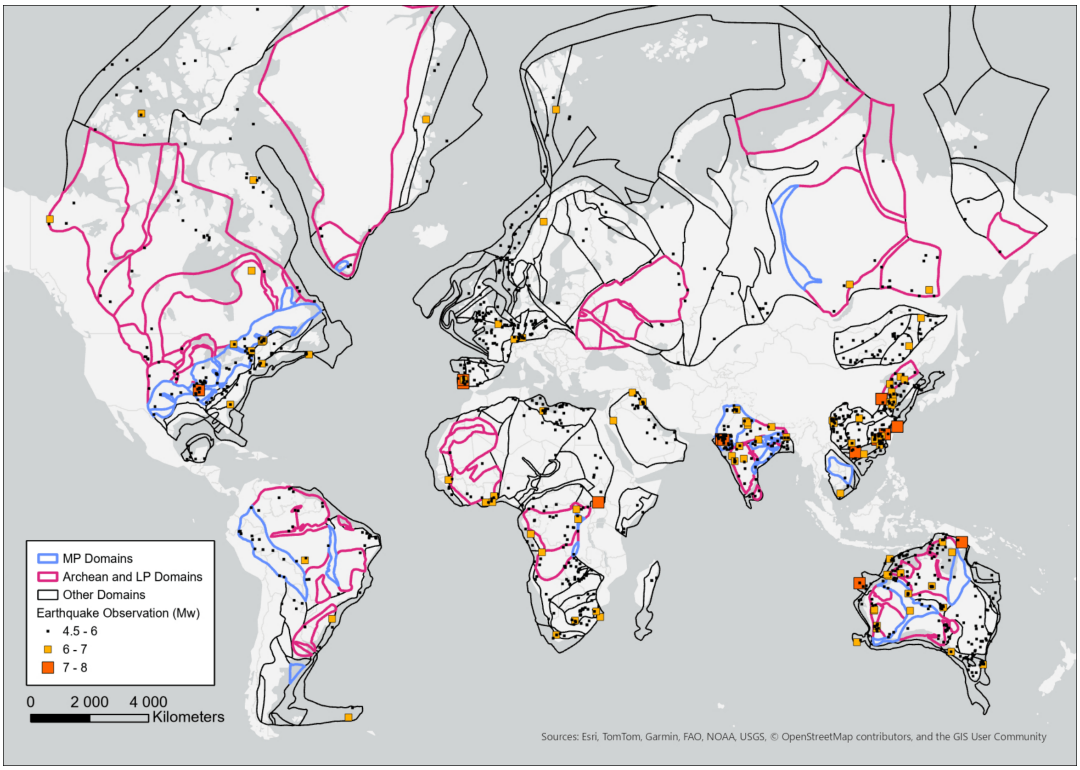

Figure 5: Analogue domains used for the Fennoscandian prior, grouped by geological age into MP domains and Archean–LP domains, shown together with all other domains and the earthquake observations from 495–2008 included in the 2012 EPRI SCR catalogue.

Domains belonging to these age groups were first used to update the EPRI catalogue and later as the basis for the maximum magnitude distribution. In cases where a domain was subdivided into multiple segments (e.g., 110a and 110b), these subdivision were treated as a single combined domain to ensure that the domain-level parameters reflect the target area as a whole and completeness estimates remain representable.

3.3.2 The Reviewed Bulletin of the ISC

The Reviewed Bulletin of the ISC [77], referred to as the ISC catalogue, contains extensive information on global seismicity from 1900 through the end of 2023. It has been compiled from the contributions of hundreds of seismological agencies which have been re-analysed by ISC seismologists. Where necessary, the analysts have manually refined hypocentre solutions and magnitude estimates, resulting in one of the most comprehensive global earthquake catalogues available.

For this work, earthquake data were retrieved from the ISC catalogue using the polygon-based event search interface [78]. The search was executed programmatically using a Python script generated with the assistance of M365 Copilot (GPT-5.2) and targeted the domains outlined in Section 3.3.1, defined by sets of coordinate vertices. Additional search constraints included a magnitude range of 4.5–9.0, a depth range

of 0–50 km, and the requirement that only magnitudes associated with the prime hypocentre be retained.

The initial query returned 826 events. Of these, 50 were removed as they were flagged by the ISC as known or suspected to be anthropogenic, predominantly associated with nuclear test activity in Russia and North Korea. Subsequent magnitude harmonisation excluded an additional 174 events, leaving 602 events in the dataset. Among these, 130 were identified as potential duplicates of observations already present in the EPRI catalogue and were merged with their corresponding counterparts. These processing steps are described in detail in Appendix A.1.

A key distinction between the ISC and EPRI catalogues is that the ISC Bulletin is not declustered. As a result, dependent but still unique events are included in the raw ISC data and will consequently persist in the updated global catalogue. In the context of Bayesian $m_{\max}$ assessment, however, this has only a minor impact on the results, since aftershocks are by definition smaller than their corresponding mainshocks. Moreover, the requirement of $M_W \geq 4.5$ naturally reduces the number of dependent events.

3.3.3 Parameters of the Updated SCR Catalogue

The final updated SCR catalogue contains a total of 1781 earthquake observations. To prepare the dataset for the subsequent maximum magnitude computations, several domain-level parameters were derived.

Following the methodology of the 2012 EPRI study [75], each domain was paired with a regional b-value taken from Johnston et al. [57], which are later used to adjust the mean of the maximum magnitude distribution. Similarly, the completeness of the catalogue was assessed using the regional completeness intervals estimated globally by Johnston et al.

These completeness intervals were used to compute the completeness-corrected number of earthquakes for each domain d given by

$$N_d^{\text{corr}} = \max \left[\sum_{i=0}^{I_{\max,d}} N_d(m_i) \frac{t_{c,d}(m_{\max,d}^{\text{obs}})}{t_{c,d}(m_i)}, N_d \right],$$

where $I_{\max,d}$ corresponds to the index of the domain's maximum observed magnitude $m_{\max,d}^{\text{obs}}$, $N_d(m_i)$ is the number of observed earthquakes with magnitude m_i that fall within their respective completeness intervals, $t_{c,d}(m_i)$ denotes the region-specific length of the interval associated with magnitude m_i, and N_d is the raw number of catalogue events in the domain prior to completeness correction. The smallest magnitude included was 4.5 M_W.

This correction accounts for the fact that catalogue completeness periods are typically shorter for small magnitudes and provides the maximum likelihood estimate for the true number of earthquakes that would have been recorded if all events could have been reliably recorded for the completeness period of the maximum observed magnitude

event. Consequently, the completeness-corrected number of earthquakes should be at least the number of events recorded in the catalogue. A summary of the resulting parameters is provided in Table 4 while the full set of domain-wise values is provided in Appendix A.2 for reference.

Table 4: Number of selected domains in each region that contain data in the final SCR catalogue (# DNs), together with the mean domain-level values of area, maximum observed magnitude ($m^{\text{obs}}_{\text{max},d}$), raw number of catalogue events (N_d), completeness-corrected event count (N^{corr}_d), and the regional b-value assigned following [57].

		Mean Value of				
Region	**# DNs**	**Area (km^2)**	$m^{\text{obs}}_{\text{max},d}$ (M$_W$)	N_d	N^{corr}_d	b
Africa	6	931 274	5.810	9.00	12.45	0.982
Australia	9	649 707	5.946	20.33	30.53	0.896
China	2	344 881	5.875	13.00	17.28	1.029
Europe	3	736 476	5.367	2.33	2.44	1.156
India	8	336 721	5.930	20.75	43.78	0.966
North America	12	1 062 113	5.685	13.42	20.99	0.728
Russia	4	881 556	5.888	11.50	14.91	1.160
South America	5	1 724 008	5.588	30.40	43.62	1.212

4 Methodology

The methodology of this thesis provides the basis for integrating the alternative SSZ models and $m_{\max}$ distributions into the hazard analysis. For the SSZs, this involves re-evaluating catalogue completeness that affects the estimation of recurrence parameters, followed by statistical testing to support the assignment of logic tree weights for the zoning alternatives. For $m_{\max}$, the Kijko and Bayesian methods are introduced, together with the framework used to combine their results and incorporate the resulting distributions into the logic tree.

4.1 Completeness Analysis

As catalogue completeness directly influences the estimation of recurrence parameters, it must be reassessed whenever the spatial definition of a source zone changes. Because the 2025 SSZ models introduce new zoning alternatives that cover different subsets of the earthquake catalogue, the completeness of the data must therefore be re-evaluated for each zone individually.

In his 2024 thesis [9], Vehmas performed a completeness analysis for both the individual and grouped SSZs of the 2016 model using the methodology proposed by Stepp [35] that is briefly discussed in Section 2.1.2. In that work, Vehmas also validated a completeness threshold of $m_c = 1.0$ M_W for all source zones of the 2016 model except SSZs 3 and 4, for which a higher threshold of $m_c = 1.5$ M_W was required. Accordingly, this thesis adopts the limit of $m_c = 1.0$ for all new 2025 source zones except the micro-level zone SE-SV, which closely corresponds to the 2016 zone 4 with the threshold of $m_c = 1.5$.

As illustrated in Section 3.2.1, the source zones of the 2025 micro largely coincide with those of the 2016 zoning. Thus, the completeness periods for the micro SSZs can be approximated with reasonable accuracy using the values obtained for the 2016 model. Following the same approach as for the source zone characterisation parameters (Section 3.2.2), each micro-model SSZ was paired with the 2016 zone with which it overlaps most strongly, and the corresponding completeness period identified by Vehmas was adopted.

The 2025 meso model, on the other hand, exhibits more substantial deviations from the 2016 zoning, and therefore the completeness analysis for these zones needed to be performed from scratch. Unlike Vehmas' thesis, which relied solely on the Stepp method, the present work utilises the CUVI method [32], which offers a slightly more intuitive graphical interpretation of completeness.

In the CUVI method, the catalogue is first filtered by SSZ and divided into magnitude bins, typically of width 0.5 M_W. For each bin, the cumulative number of events is plotted as a function of time. The point at which the cumulative curve begins to follow an approximately linear trend marks the start of the completeness interval, under the assumption of stationary earthquake occurrence rates. Previous studies [33, 79] have found good convergence between the Stepp and CUVI methods, and this claim is

verified in this thesis using the SE-NE meso- and micro-level zone, which is effectively equivalent to the grouping of SSZs 2 and 3 in the 2016 model.

4.2 Statistical Testing for SSZ Models

As discussed in Section 2.2, a key assumption in SSZ modelling is that seismicity within each source zone is spatially uniform. To evaluate whether this assumption holds in the alternative 2025 SSZ configurations, this thesis applies statistical methods designed to detect deviations from uniformity. Testing this assumption is important because violations such as spatial clustering may indicate that a zone is not homogeneous and could justify considering alternative zoning structures.

In the 2023 SENSEI study [4], the clustering test originally proposed by Musson [80] was adopted to assess this assumption specifically for the source zone of Loviisa. Musson, as cited in [4], argued that if seismic activity within an SSZ is genuinely uniform, the epicentral locations of earthquakes should follow a spatially random pattern—that is, they should be consistent with a stationary Poisson process.

To test this assumption, Musson proposed comparing the observed mean nearest neighbour distance of earthquake epicentres in each zone, denoted $d_{\text{obs},i}$, with the expected mean nearest neighbour distance under complete spatial randomness, $d_{\text{exp},i}$. For a Poisson process, the expected value is given by

$$d_{\text{exp},i} = 0.5\sqrt{\frac{A_i}{N_i}},$$

where A_i is the area of zone i and N_i is the number of earthquake observations within it. It should be noted that only earthquakes within the appropriate completeness intervals are considered in this analysis, to ensure that variations in catalogue completeness do not bias the results.

The nearest neighbour statistic is defined by the ratio

$$R_i = \frac{d_{\text{obs},i}}{d_{\text{exp},i}}.$$

A value of $R_i = 0$ reflects complete clustering at a single point, whereas values $R_i \geq 1$ are indicative of spatial randomness consistent with uniform seismicity. The variability of the test statistic can be quantified by the sampling variance,

$$\sigma_i^2 = (4 - \pi)\,\frac{A_i}{4\pi N_i^2},$$

from which the standard error of the mean nearest neighbour distance follows as

$$\sigma_i = 0.26136\sqrt{\frac{A_i}{N_i^2}}.$$

This standard error is then used to compute a Z-score with $Z_i = (d_{\text{obs},i} - d_{\text{exp},i})/\sigma_i$. The corresponding two-tailed p-value is obtained from $p_i = 2(1 - \Phi(|Z_i|))$, where Φ is the cumulative distribution function of the standard normal distribution $\mathcal{N}(0, 1)$.

To evaluate the performance of an entire SSZ model, the individual zone-level Z-scores are combined using the weighted Z-method [81]. The combined statistic is computed as

$$Z_{\text{model}} = \frac{\sum_i w_i Z_i}{\sqrt{\sum_i w_i^2}}, \tag{4}$$

where the weight $w_i = N_i$ corresponds to the number of earthquakes in zone i. The overall p-value for the SSZ model is then derived in a similar fashion to the zone-level statistics with

$$p_{\text{model}} = 2\left[1 - \Phi(|Z_{\text{model}}|)\right]. \tag{5}$$

A p-value below 0.05 indicates statistically significant clustering, implying that the SSZ model does not adequately represent uniform seismicity. Conversely, higher p-values suggest better agreement with the model assumption and thus a more appropriate SSZ zoning from the standpoint of spatial uniformity.

4.2.1 Testing for SSZ 10 Subdivisions

In addition to the clustering test, the suitability of the different subdivisions proposed in the SENSEI study [4] for source zone 10 is further assessed by comparing the observed magnitude-frequency distributions on the eastern and western sides of each proposed boundary. The underlying idea is that if two regions exhibit different magnitude distributions, this could support treating them as separate source zones and help derive appropriate weighting for the zoning alternatives in the logic tree.

According to the GR relationship, the number of earthquake occurrences should follow a linear relation with magnitude on a logarithmic scale. While this relation is expected to hold for any sufficiently large dataset, the parameters of the relation—the intercept a and slope b—may vary spatially. Variation in a can be observed in the total number of earthquake observations, whereas differences in the b value are reflected in the distribution of magnitudes.

To investigate whether such distributional differences are present in the proposed SSZ 10 subdivisions, the two-sample Kolmogorov–Smirnov (K–S) test [82] is employed. This nonparametric test compares the empirical cumulative distribution functions (CDFs) of two samples in order to determine whether they originate from populations with the same underlying distribution. The K–S test is particularly suitable in this context because it does not assume any specific parametric form for the magnitude distribution and remains effective even when sample sizes are modest, making it well-suited to the low seismicity of the region.

The null hypothesis of the test is

$$H_0 : F(m) = G(m), \qquad -\infty < m < \infty,$$

where m is magnitude and F and G denote the underlying population-level distributions associated with the two samples. The alternative hypothesis H_1 is simply that H_0 does not hold.

The corresponding test statistic is defined as

$$D_{n_1 n_2} = \sup_{-\infty<m<\infty} \left| F_{n_1}(m) - G_{n_2}(m) \right|,$$

where F_{n_1} and G_{n_2} are the empirical CDFs computed from samples of size n_1 and n_2, respectively. It can be shown that if the two samples originate from the same distribution, then $D_{n_1 n_2} \to 0$ as $n_1, n_2 \to \infty$. Thus, large observed values of $D_{n_1 n_2}$ with sufficiently large samples indicate that the null hypothesis may be rejected.

If H_0 is true, the statistic satisfies

$$\lim_{n_1,n_2\to\infty} \Pr\left[\left(\frac{n_1 n_2}{n_1 + n_2} \right)^{1/2} D_{n_1 n_2} \le x \right] = 1 - 2 \sum_{i=1}^{\infty} (-1)^{i-1} \exp\{-2i^2 x^2\} = H(x), \ \forall x > 0.$$

Values for the function $H(x)$ have been given in the literature (see, e.g., [82]). Under a significance level of 0.01, for example, the null hypothesis is rejected when

$$\left(\frac{n_1 n_2}{n_1 + n_2} \right)^{1/2} D_{n_1 n_2} \ge H^{-1}(1 - 0.01) = H^{-1}(0.99) = 1.63. \tag{6}$$

For each proposed SSZ 10 subdivision, the dataset is partitioned into western and eastern subsets, from which the empirical CDFs $F_{n_1}(m)$ and $G_{n_2}(m)$ are constructed as step functions increasing by $1/n_1$ and $1/n_2$ at each event magnitude. As in the clustering test, only earthquakes within their corresponding completeness intervals are considered in this analysis.

4.3 Maximum Magnitude Assessment

Because detailed, spatially comprehensive information on active faults is lacking in Fennoscandia, deterministic approaches for estimating the maximum magnitude are not feasible [83]. As a result, recent PSHAs for the region have relied almost exclusively on probabilistic methods [65, 84–86], typically using the Kijko method or hybrid approaches that combine the Kijko and Bayesian formulations. These methods yield continuous, unbounded probability distributions for $m_{\max}$, which must therefore be truncated at physically reasonable lower and upper limits.

A trivial lower bound for $m_{\max}$ is given by the maximum observed magnitude $m_{\max}^{\text{obs}}$ of the regional earthquake catalogue, since by definition the true maximum possible magnitude cannot be smaller than an event that has already occurred. However, in

regions of low seismicity, $m_{\max}^{\text{obs}}$ may be small simply because large earthquakes are rare. For this reason, previous Fennoscandian PSHAs have imposed an additional lower bound of 5.5 M_W, motivated by the occurrence of the 21 September 2004 Kaliningrad earthquake (5.2 M_W), which demonstrated that events larger than 5.0 M_W are possible even in areas with modest historical seismicity [42].

In this thesis, the lower-bound estimate is revisited using the widely-adopted methodology proposed by EPRI [75]. They recommend that the bound should be set below the smallest $m_{\max}^{\text{obs}}$ among suitably defined groupings of domains within the SCR database. The analogue domains for Fennoscandia, defined in Section 3.3.1, were grouped by geographical region. Within these groups the smallest $m_{\max}^{\text{obs}}$ were found in the SCRs of Indochina (5.09 M_W) and South America (5.25 M_W). Thereby, based on this approach, a lower bound of 5.0 M_W appears more reasonable for Fennoscandia.

EPRI additionally recommend that the upper bound of $m_{\max}$ should exceed the largest earthquake recorded in the SCR database, which led them to adopt an upper bound of 8.25 M_W. Prior Fennoscandian studies have instead used a more restrictive upper bound of 7.0 M_W, based primarily on historically inferred rupture lengths in the region [83]. However, even with this method it has been concluded that depending on the technique adopted to analyse the rupture lengths the upper bound of $m_{\max}$ could be close to 8.0 M_W.

Because Fennoscandian $m_{\max}$ distributions are typically heavily weighted toward the lower end of the magnitude range, the choice of the upper bound is expected to have minimal influence on the overall results. For this reason, and to maintain consistency with global methodology, the more conservative upper bound of 8.25 M_W is adopted in this thesis. The implications of both the lower and upper bound choices are explored in detail in Chapter 5.

4.3.1 Kijko Method for Maximum Magnitude Estimation

The Kijko method for estimating $m_{\max}$ relies solely on the observed earthquake magnitude distribution within the study region. The method assumes that magnitudes follow the truncated GR distribution in Equation (2), with the lower truncation point set equal to the completeness magnitude. The CDF of the magnitude is therefore

$$F_M(m) = \begin{cases} 0 & \text{for } m < m_c \\ \frac{1-\exp\{-\beta(m-m_c)\}}{1-\exp\{-\beta(m_{\max}-m_c)\}} & \text{for } m_c \leq m \leq m_c \\ 1 & \text{for } m > m_c, \end{cases} \tag{7}$$

where the slope of the GR law, $\beta = b\ln(10)$, and the magnitude of completeness m_c are derived from the local earthquake catalogue.

Kijko [54] showed that Equation (7) can be used to construct a fiducial distribution for the maximum magnitude in the form of

$$\Pr[m_{\max} < z] = 1 - [F_M(m_{\max}^{\text{obs}}; z)]^{\lambda T}, \tag{8}$$

where it is assumed that the earthquake observations in the catalogue over its whole timespan T obey the Poisson distribution with parameter λ. This distribution is then truncated according to the specified lower and upper bounds on $m_{\max}$ and renormalised to produce the final distribution used in the hazard calculations.

Although the parameters β, m_c, λ, and T may vary between different versions of the Fennoscandian earthquake catalogue, prior implementations of the method [84, 87] have shown that the resulting $m_{\max}$ distribution is highly insensitive to reasonable variations in these inputs in this region. Consequently, the present work does not recompute these parameters using the most recent FENCAT21 catalogue. Instead, the parameter values presented by Korja et al. [42], and subsequently used in Fortum's 2018 PSHA [85], are retained. These parameters are repeated in Table 5.

Table 5: Kijko $m_{\max}$ distribution parameters presented by Korja et al. [42].

Parameter	Value
m_c	1.4
$m_{\max}^{\text{obs}}$	4.5
β	2.487
λ	2.987
T	245

4.3.2 Bayesian Approach to Maximum Magnitude Estimation

The Bayesian approach to estimating $m_{\max}$ is grounded in Bayes' theorem [88]

$$p(\theta|y) = \frac{p(\theta)p(y|\theta)}{p(y)},$$

where $p(\theta|y)$ denotes the posterior distribution of the unknown parameter θ given the observed data y, $p(\theta)$ is the prior distribution of θ, $p(y|\theta)$ is the likelihood function, and $p(y) = \int p(\theta)p(y|\theta)d\theta$ is the marginal distribution of the data. In essence, Bayes' theorem provides a formal framework for updating prior knowledge about θ using new information contained in the observations.

In this thesis, the prior distribution for Fennoscandia is based on the target domains derived from the updated SCR catalogue, as described in Section 3.3. Otherwise, the methodology follows exactly that of EPRI [75], which in turn is heavily influenced by the work of Johnston et al. [57]. According to their formulation, the prior distribution is assumed to be normal, $\mathcal{N}(\mu, \sigma)$, where the mean μ is derived from the sample mean $\hat{\mu}$ of $m_{\max}^{\text{obs}}$ across the selected analogue domains, and the standard deviation σ is set equal to the corresponding sample standard deviation $\hat{\sigma}$.

However, because the observed maximum magnitude is necessarily less than or equal to the true $m_{\max}$, the authors emphasise that using $\hat{\mu}$ directly would lead to a systematic underestimation of the true maximum magnitude. To account for this bias, Johnston et

al. [57] proposed a correction based on the CDF of $m_{\max}^{\text{obs}}$, derived from the truncated GR distribution. The CDF is given by

$$F(m_{\max}^{\text{obs}}) = \left[\frac{1-\exp\{-\beta(m_{\max}^{\text{obs}} - m_{\min})\}}{1-\exp\{-\beta(m^u - m_{\min})\}}\right]^{N^{\text{corr}}}, \text{ for } m_{\min} \leq m_{\max}^{\text{obs}} \leq m^u, \quad (9)$$

where $\beta = b\ln(10)$ is the area-weighted GR slope for the target domains, $m_{\min} = 4.5\ \text{M}_\text{W}$ is the minimum magnitude considered in the PSHA calculations, m^u is a candidate value for $m_{\max}$, and N^{corr} denotes the completeness-corrected number of earthquakes across the analogue domains.

Solving Equation (9) for m^u yields

$$m^u = m_{\min} - \frac{1}{\beta}\ln\left(1 - \frac{1-\exp\{-\beta(m_{\max}^{\text{obs}} - m_{\min})\}}{F[m_{\max}^{\text{obs}}]^{1/N^{\text{corr}}}}\right), \text{ for } m_{\min} \leq m_{\max}^{\text{obs}} \leq m^u. \quad (10)$$

Since $m_{\max}^{\text{obs}}$ across the analogue domains is modeled as normally distributed, the median of this distribution ($F[m_{\max}^{\text{obs}}] = 0.5$) corresponds to the sample mean $\hat{\mu}$. Applying the correction of Equation (10) to this median yields a bias-corrected estimate of the mean of m^u, which becomes the mean of the prior for $m_{\max}$. The standard deviation of the prior is retained as the original sample standard deviation $\hat{\sigma}$.

As illustrated in Figure 6, the effect of the bias correction increases with increasing $m_{\max}^{\text{obs}}$ and decreasing sample size. Thus, the correction is only meaningful when applied to sufficiently large groupings of analogue domains.

Once a bias-corrected prior distribution has been obtained, it can be updated using the earthquake catalogue of the specific target region. According to EPRI [75], the likelihood function derived from the local data is

$$L[m^u] = \begin{cases} 0, & \text{for } m^u < m_{\max}^{\text{obs}}, \\ [1-\exp\{-\beta(m^u - m_c)\}]^{-N_c}, & \text{for } m^u \geq m_{\max}^{\text{obs}}, \end{cases}$$

where β and $m_{\max}^{\text{obs}}$ are determined from the local catalogue, and N_c is the number of earthquakes with magnitudes greater than or equal to the catalogue completeness magnitude m_c.

The posterior distribution is then obtained by multiplying the prior by this likelihood and truncating to integrate to one between the defined bounds of $m_{\max}$. For catalogues with only a few considerable earthquakes, such as the Fennoscandian catalogue, the likelihood is relatively flat for large magnitudes. Its primary effect is therefore to truncate the distribution below $m_{\max}^{\text{obs}}$, leaving the shape of the upper tail largely controlled by the prior.

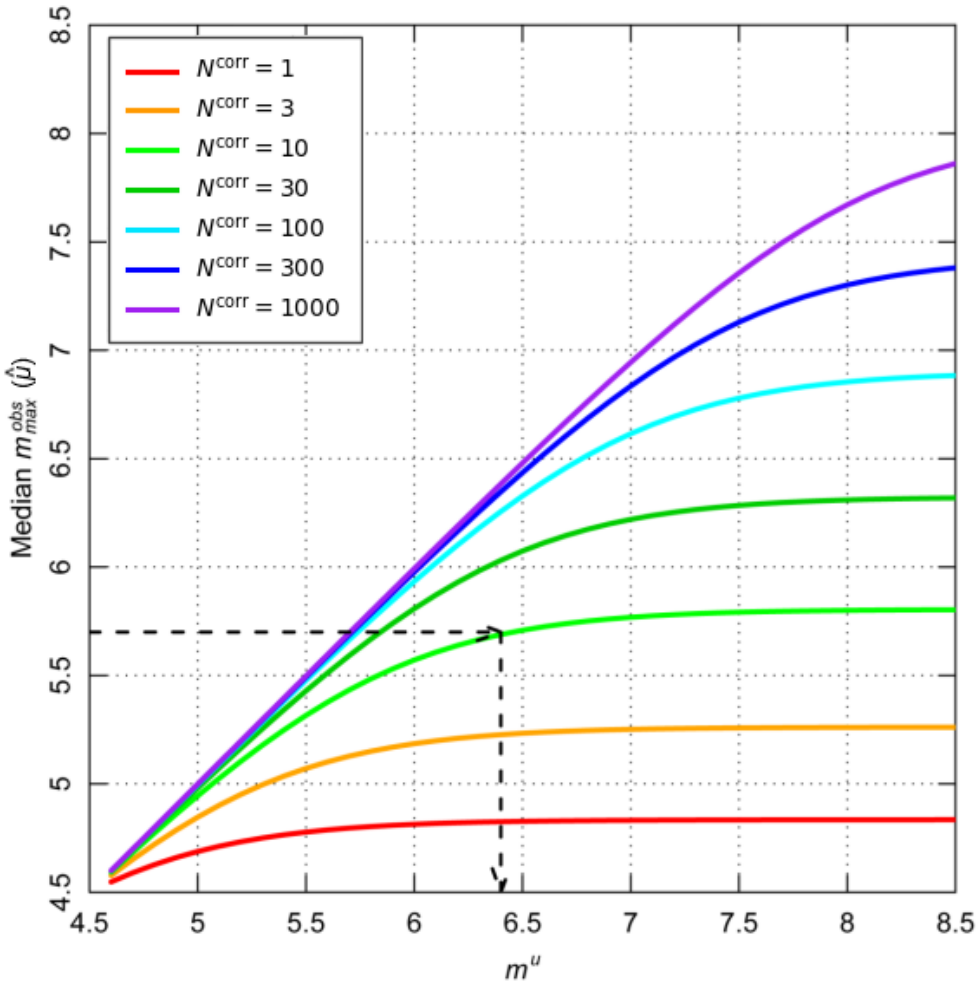

Figure 6: Median values of $m_{\max}^{\text{obs}}$ (equivalent to the sample mean $\hat{\mu}$ under a normal distribution) as a function of the candidate value m^u for the maximum magnitude and the bias corrected sample size N^{corr}. Dashed lines show bias correction for a $m_{\max}$ of 5.7 with a sample size of 10. Figure modified from [75].

4.3.3 Combining the Methods

The alternative approaches for estimating $m_{\max}$ can be incorporated in the hazard calculations in two ways. The first option, used in previous Finnish PSHAs [65, 86], is to assign each method its own branch in the logic tree, effectively repeating the hazard computation separately for each model. The second option, adopted for example by EPRI [75], is to combine the continuous $m_{\max}$ distributions produced by the different methods into a single weighted distribution and represent only this combined distribution in the tree. In this thesis, the latter approach is adopted, as it provides a substantial gain in computational efficiency while producing hazard results that are effectively identical to those obtained with separate method-specific branches.

To form the combined distribution, the continuous $m_{\max}$ distributions from the Kijko and Bayesian methods are first scaled according to the weights assigned to the two approaches. EPRI [75] proposed using the Kijko's fiducial distribution in Equation (8) as an index for determining these weights: when $\Pr[m_{\max} > 8.25]$ reaches 0.5 or higher, the Kijko method is assigned zero weight, whereas at $\Pr[m_{\max} > 8.25] = 0$—where Kijko's approach is at its strongest with large numbers of larger earthquakes—the Kijko and Bayesian methods are considered equally credible.

In Fennoscandia, where large earthquakes are rare, this weighting scheme would effectively eliminate the contribution of the Kijko method. However, unlike in the context of the Central and Eastern United States considered by EPRI, the Fennoscandian catalogue provides little information with which to significantly update the Bayesian prior. Thus, there is no compelling justification for giving the Bayesian approach strictly greater weight. Following recent Finnish PSHAs [65, 86], equal weighting of the two methods is therefore adopted in the present work.

Since the PSHA logic tree requires discrete rather than continuous representations, the resulting combined continuous $m_{\max}$ distribution must be discretised. For this purpose, the procedure of Miller and Rice [89] is used. Their two-step Gaussian quadrature scheme constructs a discrete approximation that preserves the primary statistical moments (i.e., the mean, standard deviation, skewness, and kurtosis) of the underlying continuous distribution.

The method provides a set of cumulative probability values together with associated probability weights. These cumulative probabilities are then evaluated using the combined $m_{\max}$ distribution to obtain the corresponding quantile values, which serve as the discrete maximum magnitudes in the logic tree. The five-point approximation that is commonly used with maximum magnitudes (see e.g. Table 5.3.3-1 in [75]) is presented in Table 6.

Table 6: Miller and Rice five-point discrete approximation to a continuous probability distribution [89] and the rounded weights used in PSHA calculations.

Cumulative Probability of a Continuous Distribution	Miller and Rice Probability Weight	Modified Weight for PSHA
0.034893	0.10108	0.101
0.211702	0.24429	0.244
0.500000	0.30926	0.310
0.788298	0.24429	0.244
0.965107	0.10108	0.101

4.4 Configuration for Hazard Calculations

The seismic hazard estimate for the Loviisa and Olkiluoto NPPs is computed using a modified version of the HAZ45 program originally developed by Norman Abrahamson [90]. The version used in this work incorporates updates made by Slate Geotechnical

Consultants, including the implementation of new GMPEs and a magnitude-recurrence model with a varying b-value. This same modified code base was also employed in Vehmas' thesis [9].

To assess the sensitivity of the hazard results to the updated source zone models and maximum magnitude, the results of this thesis are compared directly to those of Vehmas. Apart from the model components that are explicitly modified, the computational setup is kept as close as possible to that of [9]. The logic tree used by Vehmas is presented in Figure 7 for reference.

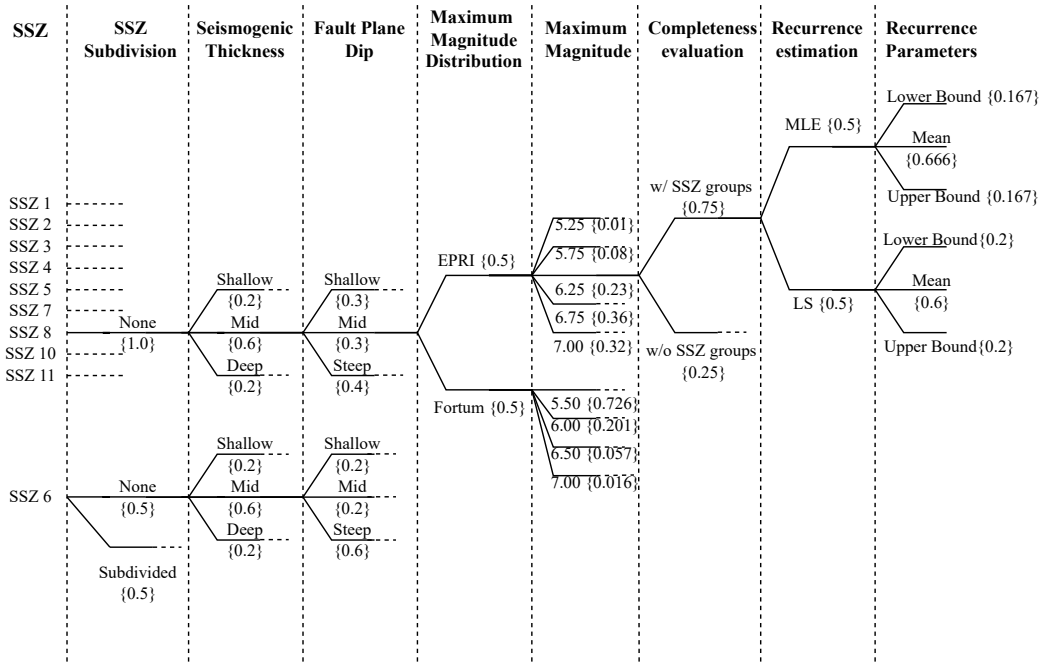

Figure 7: Logic tree presented by Vehmas [9] that is used as reference in the present thesis. The weights for the branches are given in braces.

Following Vehmas' configuration, the minimum magnitude is set to $m_{\text{min}} = 4.5\,\text{M}_\text{W}$, which reflects a standard engineering choice in PSHA to exclude small earthquakes that do not contribute to seismic hazard [7]. The modified NGA-East GMPE model, originally developed for Central and Eastern North America [91], is also adopted without further modification.

The ground-motion calculations use SA as the intensity measure. Hazard curves are evaluated at 18 SA levels ranging from 10^{-5} g to 5 g. Because SA is frequency dependent, exceedance rates are computed for 21 oscillator frequencies between 0.1 and 100 Hz, consistent with the frequency range of the modified NGA-East GMPE set.

Activity parameters are also estimated exactly as in Vehmas' work: recurrence parameters are computed using both the MLE and LS methods, with equal weights assigned to the two approaches. For the 2016 SSZ model, the parameters are taken directly from [9], whereas they are recomputed for the 2025 models and the SSZ 10

subdivisions. The full procedure and results of these computations are provided in Appendix B.

To incorporate the new SSZ models, the logic tree in Figure 7 is retained in structure but updated so that its zone branches reflect the alternative models. Additionally, the meso-level completeness evaluation is applied only without SSZ groups, since the underlying zones are already aggregated from the micro model. For the purpose of sensitivity analysis, the two 2025 models are treated independently rather than as branches of a shared logic tree.

As in [9], only SSZs within a 300 km radius of each NPP site are included. For Loviisa, these consist of FI-S, FI-C, EE-SW, EE-NE, SK, NK, and LL in the micro model, and FI-EE in the macro model. For Olkiluoto, the relevant micro zones are SE-NR, SE-NE, SE-SV, BB-S, FI-S, FI-C, EE-SW, EE-NE, and SK, together with the macro zones SE, SE-NE, BB, and FI-EE.

To investigate the impact of the proposed SSZ 10 subdivisions, each subdivision is implemented separately with full weight in the logic tree. This differs fundamentally from the SSZ 6 subdivision in the 2016 model, for example, which carried only 50 % weight. It also contrasts with the treatment in the SENSEI study [4], where the eastern part of the zone was merged with SSZ 6, but this difference was verified to have no impact on the resulting hazard estimate.

Finally, sensitivity to maximum magnitude is evaluated by modifying the $m_{\max}$ branches of the reference logic tree. Vehmas employed the Kijko-based "Fortum" distribution and the Bayesian "EPRI" distribution as two alternative $m_{\max}$ models, as shown in Figure 7. In the present work, the Bayesian approach is updated and combined with the Kijko distribution following the procedure described in the previous section. The resulting logic tree structure for $m_{\max}$ is presented in Figure 8, with the five magnitude points corresponding to the Miller and Rice approximation listed in Table 6.

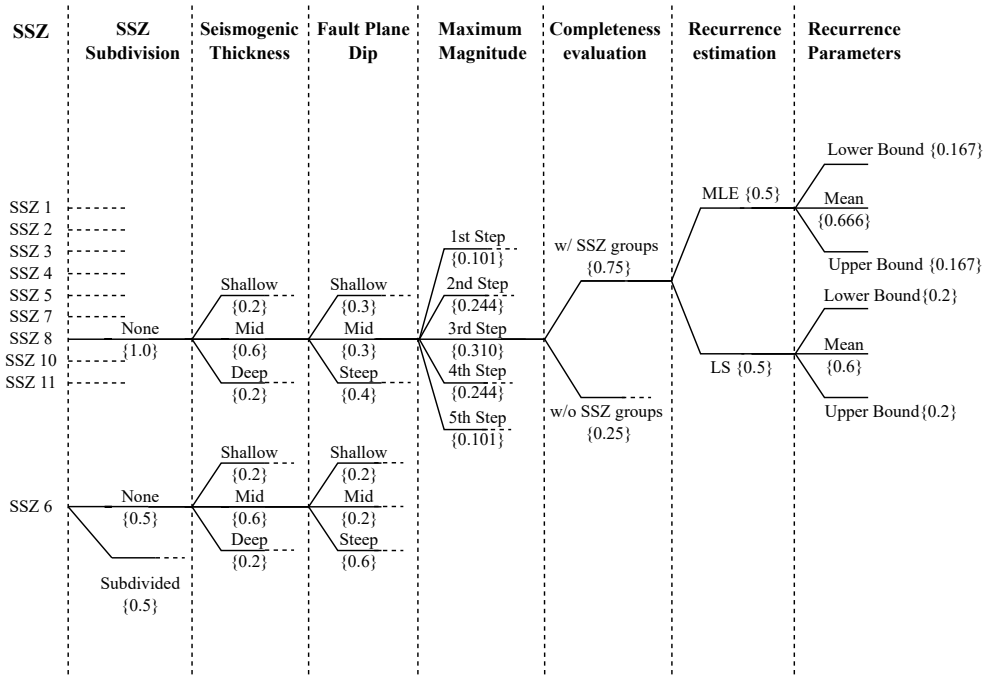

Figure 8: Logic tree to account for the $m_{\max}$ modification with the branch weights in braces. The five magnitude steps refer to the five points of the Miller and Rice approximation in Table 6.

5 Results

5.1 Catalogue Completeness

Completeness of the FENCAT21 dataset was assessed for the micro-level SSZs by matching each micro zone to the corresponding 2016 SSZs, for which completeness had been estimated using the Stepp method [35] by Vehmas [9]. The division between completeness with and without SSZ groups was retained. As concluded by Vehmas, the 2016 SSZs 7 and 11 have so few observations in FENCAT21 that reliable completeness intervals cannot be derived. Since the micro-level zones EE-SW and LL coincide closely with these 2016 zones, no completeness intervals were assigned to them. Similarly, no completeness interval was assigned to the NK zone, which lies outside the 2016 model domain. The resulting completeness intervals for micro SSZs are presented in Table 7.

Table 7: Start years of completeness intervals by magnitude bin, derived by linking the micro SSZ zones to the corresponding 2016 SSZ completeness intervals presented by Vehmas [9]. Each completeness interval begins on the first day of the listed year and ends on 31 December 2021. Cell colors indicate the source groupings adopted by Vehmas.

		Magnitude Bin					
SSZ (2016)	**SSZ (micro)**	**1.0–1.5**	**1.5–2.0**	**2.0–2.5**	**2.5–3.0**	**3.0–3.5**	**3.5–**
1	SE-NR	2007	1992	1962	1782	1742	1742
2	SE-NE	2002	1992	1962	1882	1882	1742
3	–	–	2002	1962	1882	1882	1742
4	SE-SV	–	2002	1962	1782	1742	1742
5	BB-S	1997	1997	1962	1942	1882	1742
6	FI-S, EE-NE	2012	2012	1882	1742	1742	1742
8	FI-C	2012	2002	1882	1742	1742	1742
10	SK	2007	2007	1882	1742	1742	1742

For the meso SSZs, the completeness was re-evaluated using the CUVI method. Figure 9 presents the plot used to analyse the completeness for the SE-NE zone. In it, a clear point of transition to a linear cumulative trend can be distinguished for magnitudes below 3 M_W. At larger magnitudes, however, the observation count becomes very small, and the cumulative curve resembles a step function, complicating the identification of completeness intervals. For this reason, the largest magnitude bin $[3.5, 4.0)$ M_W was assessed collectively for all source zones. Throughout the analysis the intuitive requirement was enforced that the completeness interval for larger magnitudes must be at least as long as that determined for smaller magnitudes, which notably affects the results for the highest magnitude bins.

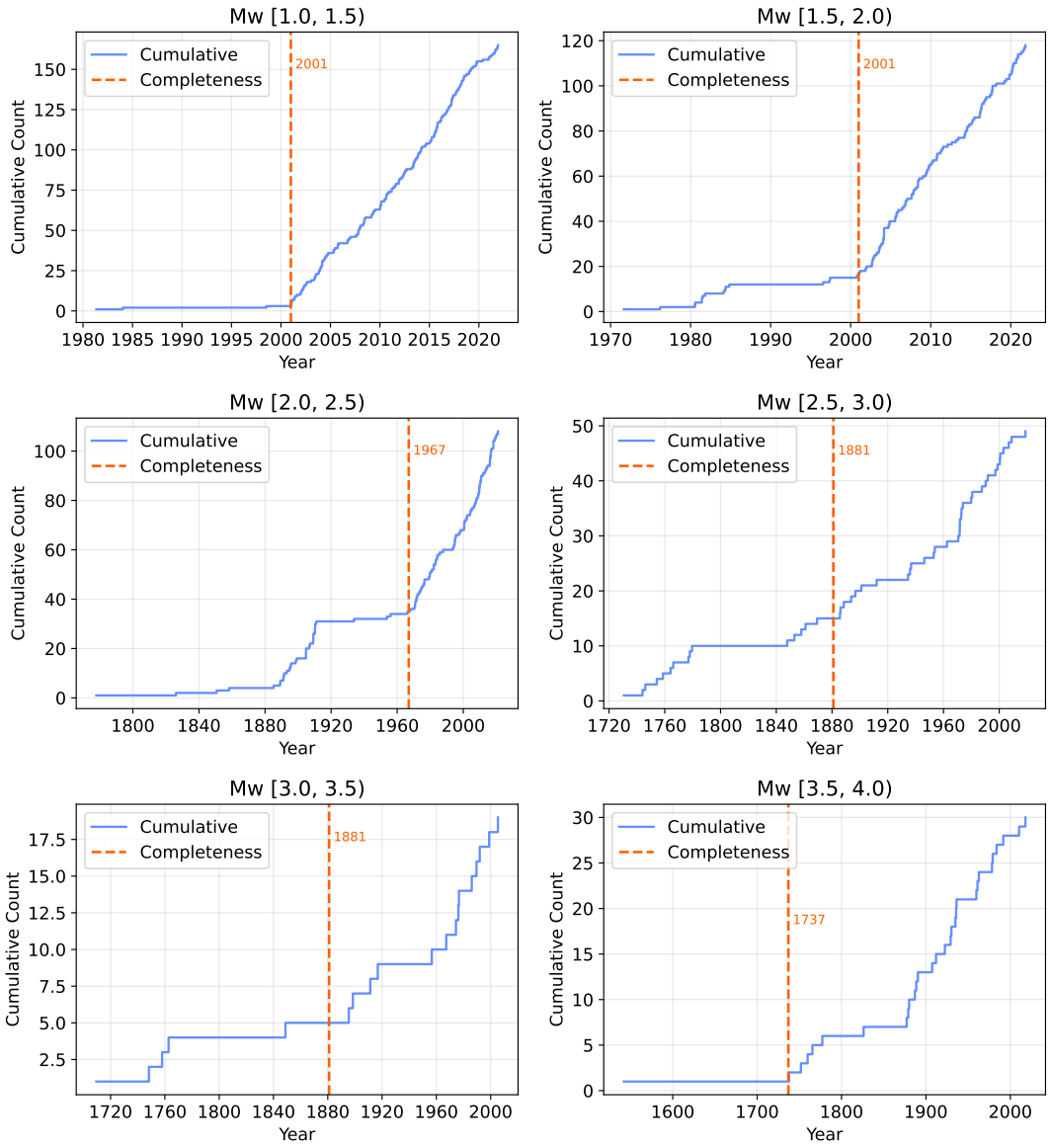

Figure 9: Start years of the completeness intervals by magnitude bin, estimated with the CUVI method for the meso-level SE-NE zone. The largest magnitude bin $[3.5, 4.0)$ M_W was assessed collectively for all source zones.

As noted in Section 4.1, the meso-level SE-NE zone is identical to the micro-level SE-NE zone, which in turn corresponds closely to the combined 2016 SSZs 2 and 3. This makes the zone a useful reference case for comparing the completeness estimates obtained with the CUVI and Stepp methods. Based on the results, the two approaches agree very well, with differences of less than ten years across all magnitude bins. For example, for the largest magnitude bin, the CUVI method yields a completeness start year of 1737, whereas Vehmas' analysis indicates 1742. The completeness analyses for the remaining meso-level zones are provided in Appendix C, and the resulting start years of the completeness intervals are summarised in Table 8.

Table 8: Start years of completeness intervals by magnitude bin, estimated with the CUVI method for all meso-level zones. Each completeness interval begins on the first day of the listed year and ends on 31 December 2021.

	Magnitude Bin					
SSZ (meso)	**1.0–1.5**	**1.5–2.0**	**2.0–2.5**	**2.5–3.0**	**3.0–3.5**	**3.5–**
SE	2002	2000	1966	1783	1752	1737
SE-NE	2001	2001	1967	1881	1881	1737
BB	2001	2001	1969	1957	1889	1737
FI-EE	2010	2005	1899	1751	1751	1737

5.2 Comparison of SSZ Models

The clustering test, discussed in Section 4.2, was conducted for all SSZs for which catalogue completeness could be assessed. Consequently, SSZs 7 and 11 were excluded from the 2016 model, and the micro-level zones EE-SW, LL, and NK were excluded from the 2025 model. The analysis was conducted primarily using the FENCAT17 catalogue, while the corresponding results based on FENCAT21 are included for comparison. Before performing the tests, both catalogues were filtered according to the completeness intervals defined in Tables 7 and 8, thereby removing variations in completeness that might otherwise bias the results. Although the completeness estimates were derived solely from FENCAT21, they were deemed sufficiently representative for FENCAT17 as well, given the substantial overlap between the two catalogues.

The areas of the SSZs used in the analysis were computed using the commercial geographic information system software ArcGIS Pro [92]. The clustering test results are shown in Table 9, which lists the nearest neighbour statistics for each zone. For each complete SSZ model (2016, micro, meso), the overall R-value was calculated as an N-weighted average of the zone-specific values, while the total model Z and p statistics were computed using Equations (4) and (5), respectively.

Table 9: Clustering test results for the 2016, micro, and meso SSZ models based on the FENCAT17 and FENCAT21 catalogues. Listed for each zone are the event count N, the nearest neighbour statistic R, and the corresponding Z-score and p-value, with model-level results obtained using the weighted procedures of Section 4.2.

	FENCAT17				FENCAT21			
SSZ	***N***	***R***	***Z***	***p*-value**	***N***	***R***	***Z***	***p*-value**
1	88	1.034	0.611	0.541	105	0.964	-0.703	0.482
2	191	0.875	-3.311	0.001	244	0.841	-4.754	1.99E-6
3	103	0.920	-1.550	0.121	114	0.889	-2.274	0.023
4	67	0.830	-2.660	0.008	72	0.792	-3.371	0.001
5	487	0.806	-8.198	2.22E-16	625	0.758	-11.595	4.36E-31
6a	12	1.167	1.108	0.268	21	1.027	0.237	0.813
6b	17	1.132	1.044	0.297	25	0.957	-0.414	0.679
6c	21	0.564	-3.825	1.31E-4	28	0.527	-4.787	1.69E-6
8	102	0.816	-3.563	3.67E-4	126	0.798	-4.339	1.43E-5
10	42	0.714	-3.550	3.87E-4	104	0.450	-10.734	7.08E-27
Total (2016)	**1130**	**0.849**	**-9.722**	**2.43E-22**	**1466**	**0.783**	**-15.909**	**5.49E-57**
SE-NR	183	0.964	-0.924	0.355	214	0.919	-2.266	0.023
SE-NE	319	0.823	-6.045	1.50E-9	388	0.793	-7.813	5.55E-15
SE-SV	67	0.835	-2.589	0.010	72	0.806	-3.145	0.002
BB-S	490	0.804	-8.285	2.22E-16	629	0.763	-11.358	6.73E-30
FI-S	36	0.947	-0.604	0.546	55	0.872	-1.813	0.070
EE-NE	12	0.973	-0.181	0.856	16	0.976	-0.187	0.852
FI-C	110	0.809	-3.826	1.30E-4	133	0.788	-4.667	3.06E-15
SK	42	0.714	-3.550	3.87E-4	104	0.450	-10.734	7.29E-27
Total (micro)	**1259**	**0.837**	**-11.059**	**1.97E-28**	**1611**	**0.781**	**-16.843**	**1.18E-63**
SE	363	0.858	-5.175	2.28E-7	418	0.839	-6.279	3.41E-10
SE-NE	322	0.829	-5.870	4.37E-9	391	0.798	-7.644	2.11E-14
BB	677	0.806	-9.660	4.45E-22	859	0.755	-13.734	6.32E-43
FI-EE	235	0.655	-10.105	5.25E-24	354	0.623	-13.562	6.751E-42
Total (meso)	**1597**	**0.800**	**-15.269**	**1.23E-52**	**2022**	**0.758**	**-20.843**	**1.78E-96**

Across all models and both catalogues, the results indicate that none of the SSZ configurations yields a spatially uniform epicentre distribution. In every case, the probability of observing nearest neighbour distances as short as those found in the data under a uniform spatial hypothesis is well below standard significance thresholds. To put the results into context, a source zone consistent with complete spatial randomness would typically exhibit an R-value close to 1, corresponding to Z-scores near 0 and p-values comfortably above common significance levels such as 0.05. In contrast, the observed R-values are well below 1, and the associated Z-scores are strongly negative, resulting in extremely small p-values. These results indicate that statistically significant clustering is present throughout all models.

This outcome is reasonable given the limited seismicity data available for model development: each SSZ model relies on a combination of different information types that does not necessarily align perfectly with the recorded earthquake locations of limited time horizons. The effect is further amplified in the FENCAT21 results, where partially untreated swarm activity produces even shorter nearest neighbour distances and lead to even lower p-values.

Within the 2016 model, the strongest clustering is observed in SSZs 5, 6c, 8, and 10. These zones correspond closely with the micro-level zones SE-NE, BB-S, FI-C, and SK, which exhibit similarly strong clustering behaviour in the micro model. In the meso model, the most pronounced clustering is found in FI-EE, which encompasses most of these higher-clustering areas.

Overall, the 2016 and 2025 micro models display very similar clustering characteristics, reflecting the fact that both are based on relatively fine spatial delineations that can capture local variations in seismicity. The meso model, by contrast, exhibits markedly stronger clustering. This outcome is expected, since the meso model merges several micro-scale structures into larger zones, which smooths over local variability and causes multiple clusters to appear within the same region. As a result, the meso-scale representation inevitably produces stronger clustering signals than the more detailed 2016 and micro models.

5.2.1 Comparison of SSZ 10 Subdivisions

The results of the clustering test for the alternative subdivisions of SSZ 10 are presented in Table 10. For each subdivision, the catalogues were filtered using the completeness interval defined for the undivided source zone in Table 7, as the available data do not permit a reliable subdivision-specific completeness assessment.

Table 10: Nearest neighbour clustering results for the alternative subdivisions of SSZ 10 using the FENCAT17 and FENCAT21 catalogues: event count N, nearest neighbour statistic R, and the corresponding Z-score and p-value for each subdivision, with the undivided zone included for comparison.

	FENCAT17				FENCAT21			
Subdivision	***N***	***R***	***Z***	***p*-value**	***N***	***R***	***Z***	***p*-value**
1 East	10	0.79	-1.25	0.211	22	0.59	-3.70	2.16E-4
West	32	0.78	-2.42	0.016	82	0.47	-9.11	8.01E-20
2 East	10	0.85	-0.93	0.351	21	0.59	-3.61	3.01E-4
West	32	0.70	-3.22	0.001	83	0.43	-9.98	1.92E-23
3 East	9	1.07	0.39	0.697	18	0.68	-2.62	8.85E-3
West	33	0.73	-2.99	0.003	86	0.42	-10.25	1.14E-24
No Subdivision	42	0.71	-3.55	3.87E-4	104	0.45	-10.73	7.18E-27

When evaluated using the FENCAT17 catalogue, the western part of the zone consistently exhibits stronger evidence of clustering than the eastern part regardless

of the subdivision implemented. With the common reference level of 0.05, none of the subdivision alternatives remove the indication of clustering in the western half, whereas in the eastern half the observed p-values are comparatively large and therefore do not contradict the hypothesis of spatial randomness. When the analysis is repeated with FENCAT21, whose inclusion of more swarm activity increases the sensitivity of the nearest neighbour test, low p-values appear across all subdivisions and in both halves of the zone. Importantly, regardless of whether statistical significance is attained, all subdivisions lead to higher values of the nearest neighbour statistic R compared to the undivided zone, indicating a consistent reduction in clustering.

The K–S test yields a less definitive picture. As shown in Table 11, none of the subdivision alternatives display statistically significant differences in their magnitude distributions for either catalogue. In contrast to the clustering test—where a low p-value argues against the subdivision—a low p-value in the K–S test supports it, as it indicates that the two parts of the zone display distinct magnitude characteristics. Conversely, a high p-value suggests that any differences between the proposed subdivisions arise primarily from variations in earthquake frequency rather than from differences in magnitude behaviour. This lack of significance may also be influenced by the limited number of events in the eastern part of the zone, which reduces the sensitivity of the K–S test to detect subtle distributional differences.

Table 11: K–S test results for the SSZ 10 subdivisions with FENCAT17 and FENCAT21 filtered according to the completeness interval of SSZ 10 presented in Table 7. The scaled K–S statistic refers to the metric presented in Equation (6).

	FENCAT17		FENCAT21	
Subdivision	**Scaled K–S Statistic**	***p*-value**	**Scaled K–S Statistic**	***p*-value**
1	0.880	0.335	0.965	0.262
2	0.880	0.335	0.815	0.448
3	1.048	0.174	0.927	0.302

Taken together, the clustering and K–S results suggest that any decision to subdivide SSZ 10 should be guided primarily by the spatial distribution of seismicity rather than by differences in magnitude behaviour. However, the available evidence does not clearly favour any of the proposed subdivisions, and none can be identified as definitively superior based on the present analyses.

5.3 Maximum Magnitude Distribution

The mean observed maximum magnitude $m_{\max}^{\text{obs}}$ obtained from the analogue domains of Fennoscandia in the updated SCR catalogue is 5.78 M_W, with a standard deviation of 0.60. After applying bias correction in Equation (10), the mean increases to 6.04 M_W, and this corrected value was used to construct the Bayesian prior distribution shown in Figure 10.

If the prior had instead been formed by excluding domains of Middle Proterozoic age—which are analogues primarily to Norway—the bias-corrected mean would have been 6.09 M_W. Because this increase is marginal and has no practical implications for the seismic hazard assessment, the full original set of analogue domains was preserved.

The resulting prior has a notably lower mean than the SCR priors presented in literature, reflecting the observation that the maximum magnitude in regions of similar geologic age to Fennoscandia tend to be lower than the average values inferred for SCRs globally. For comparison, the prior for non-extended crust proposed by Johnston et al. [57] was used in Loviisa's most recent PSHAs [65, 86], and EPRI's [75] prior for non-Mesozoic and younger extension (NMESE) was adopted in the SENSEI study [4].

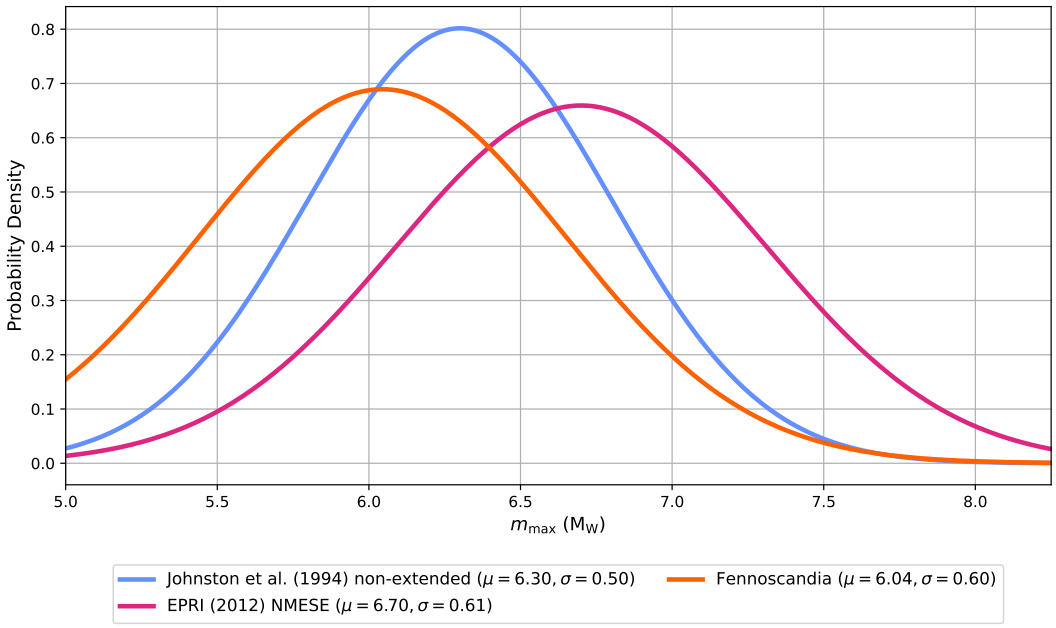

Figure 10: The Fennoscandian m_{max} prior distribution derived from the updated SCR catalogue compared with the more global priors suggested in the literature [57, 75]. All distributions are truncated and normalised to the interval $[5.00, 8.25]$.

To derive the posterior distribution used to define the weights of the discrete m_{max} values in the hazard calculations, the Fennoscandian prior was updated using a likelihood function based on the FENCAT21 catalogue within a 300 km radius of the Finnish NPPs. As illustrated in Figure 11, this likelihood function is essentially flat within the truncated interval $[5.00, 8.25]$. Consequently, the posterior distribution differs only marginally from the truncated prior, and the two are effectively identical for the purposes of the hazard calculations.

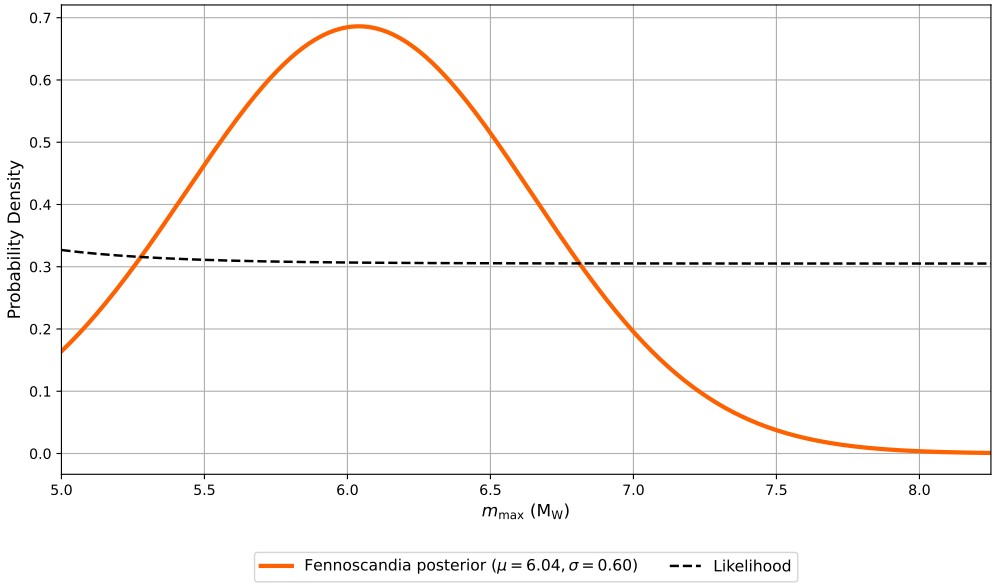

Figure 11: The likelihood function used to update the Fennoscandian $m_{\max}$ prior, and the resulting posterior distribution. Both are truncated and normalised to the interval $[5.00, 8.25]$.

The resulting Bayesian posterior was then combined with the Kijko $m_{\max}$ distribution from Fortum's 2018 PSHA [85], with equal weighting assigned to both alternatives. The combined distribution, shown in Figure 12, places proportionally more weight on smaller maximum magnitudes through the Kijko contribution, while the probability mass associated with larger magnitudes originates mainly from the Bayesian posterior.

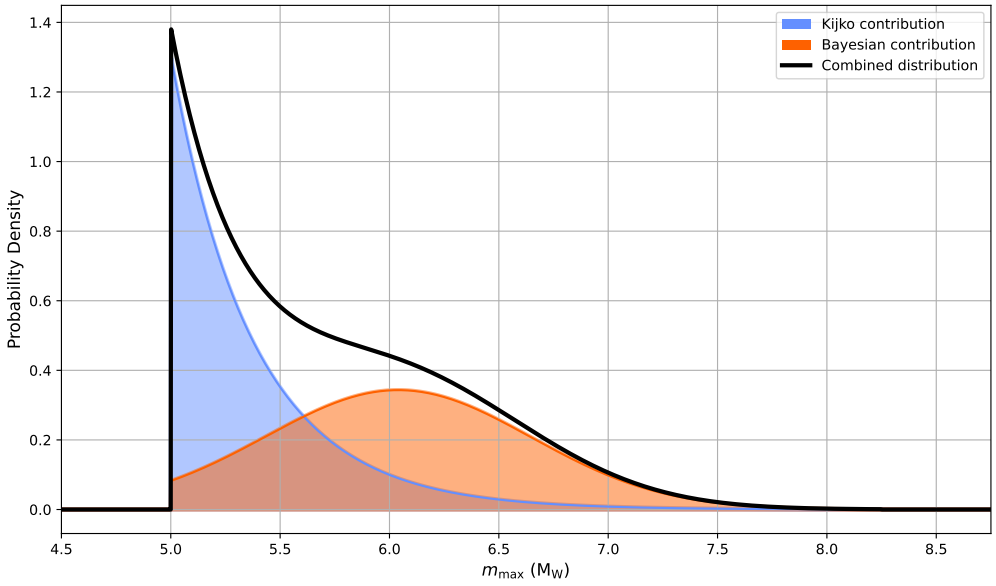

Figure 12: The combined $m_{\max}$ distribution obtained by weighting the Bayesian posterior and the Kijko distribution equally. The distribution is truncated and normalised to the interval $[5.00, 8.25]$.

Applying the Miller and Rice five-point approximation to this combined distribution yields the discrete $m_{\max}$ values and their associated weights used in the PSHA calculations, as presented in Table 12. The procedure was repeated with alternative truncation bounds to evaluate the sensitivity of the resulting values to these limits. As expected, the lower bound has a noticeably stronger influence on the discrete $m_{\max}$ values than the upper bound, even when the latter is varied more substantially. Nevertheless, the changes induced by adjustments to either bound remain small and have no impact on the seismic hazard estimates for the Finnish nuclear sites.

The weighted average of the discrete $m_{\max}$ values obtained with the bounds [5.00, 8.25] is 5.74 M_W, which is lower than the corresponding weighted average of 6.15 M_W used by Vehmas [9]. This reflects the lower mean of the Fennoscandian prior when compared with the previously employed global priors.

Table 12: Discrete $m_{\max}$ values and their corresponding weights used in the hazard calculations for three sets of truncation bounds. Weighted averages are provided for comparison.

	$m_{\max}$ with limits		
Weight	**[5.50, 7.00]**	**[5.00, 7.00]**	**[5.00, 8.25]**
0.101	5.52	5.03	5.03
0.244	5.65	5.19	5.19
0.310	5.93	5.60	5.61
0.244	6.35	6.19	6.25
0.101	6.82	6.77	6.98
Weighted Average	6.01	5.70	5.74

5.4 Loviisa Seismic Hazard Estimate Sensitivity

Loviisa's seismic hazard estimate was recalculated for each modelling decision considered in this thesis and compared with the results of Vehmas [9]. This section summarises the key findings, primarily by examining the mean UHRS at selected AFEs. Alternative presentations of the hazard estimate results are provided in Appendix D.

5.4.1 Loviisa Hazard Estimate with 2025 Models

Figure 13 compares the mean UHRS obtained with the 2025 micro and meso models against the 2016 model results. The results indicate that incorporating the micro model leads to a minor increase in the hazard estimate at AFEs above 10^{-6}, and otherwise has practically no observable effect. In contrast, the meso model produces a consistent reduction in the estimated hazard across all AFEs and frequencies, with the most pronounced decreases occurring at AFEs of 10^{-5} and 10^{-6} and below.

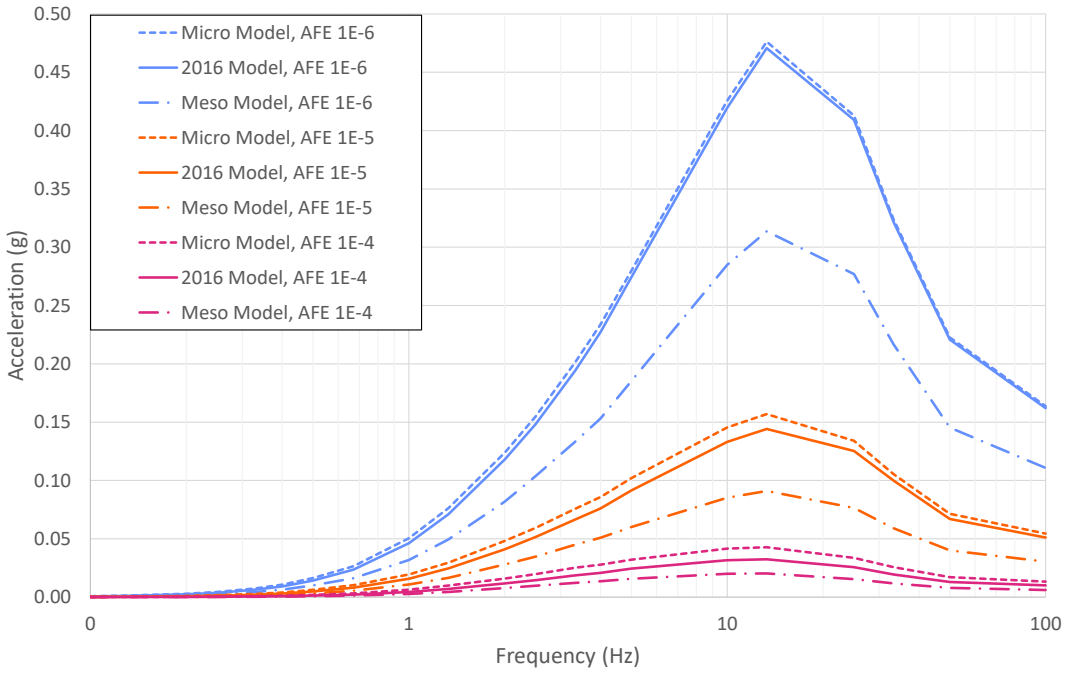

Figure 13: Loviisa mean UHRS at different AFEs using the 2025 micro and meso models. The 2016 model corresponds to the results of Vehmas [9] and is included for comparison.

Both outcomes are expected. Since the micro model does not alter SSZ 10, which overwhelmingly dominates the estimated hazard at Loviisa, the resulting hazard estimate remains effectively unchanged. The meso model, by contrast, spreads the concentrated seismicity of the nearest source zones across a much larger area. This dilutes the seismicity rates per unit area, leading to a systematic reduction in the hazard estimate.

The hazard contributions of individual source zones further demonstrate these effects. As shown in Figure 14, at higher levels of acceleration the total estimated hazard is almost entirely controlled by the host zone SK in the micro model. In the meso model, however, FI-EE is the only zone within 300 km of the site; hence the hazard contribution trivially originates exclusively from that single source zone. The resulting differences between frequencies mirror the behaviour observed in the UHRS: at low AFEs, the predicted acceleration is notably higher around the 10–25 Hz range than at lower or higher frequencies.

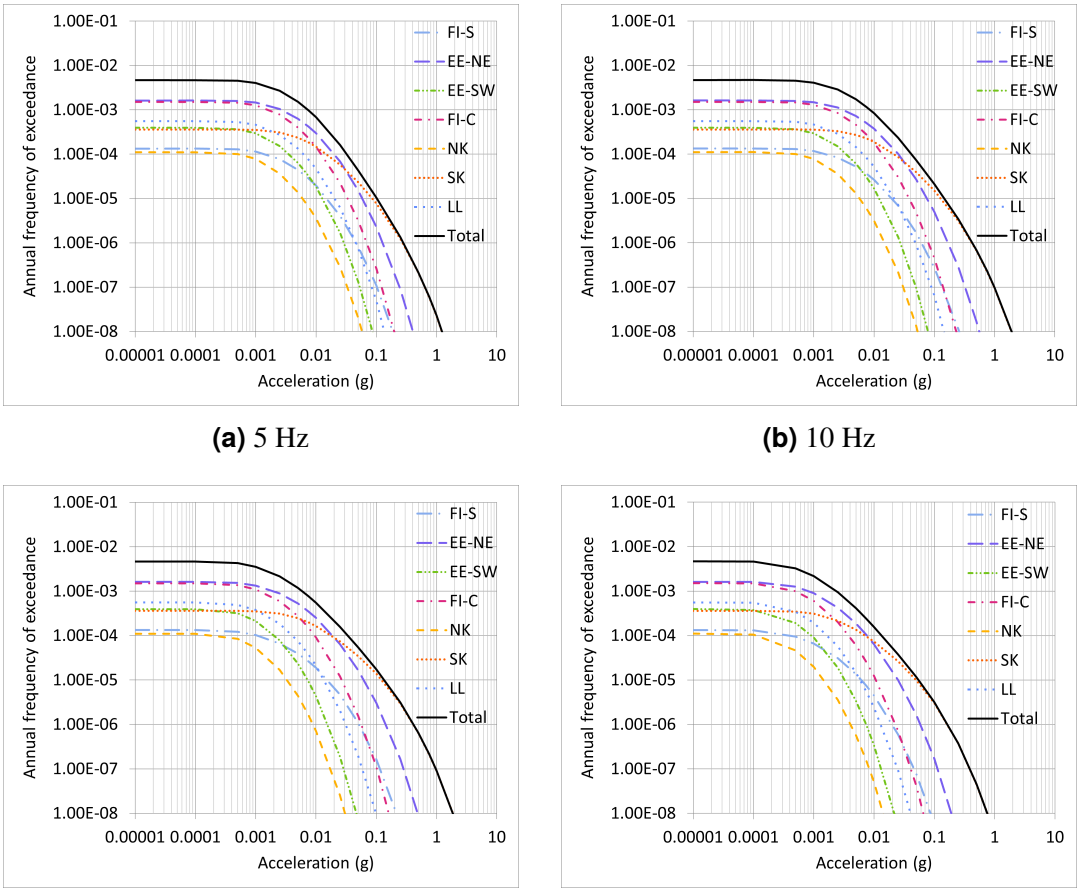

(a) 5 Hz

(b) 10 Hz

(c) 25 Hz

(d) 100 Hz

Figure 14: Loviisa mean hazard curves by micro SSZ and the total mean at different frequencies.

5.4.2 Loviisa Hazard Estimate with SSZ 10 Subdivision

The impact of subdividing SSZ 10 in the 2016 model is in Figure 15. In contrast to the negligible effect of the 2025 micro model, dividing the host zone results in a clear and systematic increase in the hazard estimate. This arises because the relatively elevated seismicity of the western portion of the zone becomes concentrated into a smaller area instead of being averaged together with the less active eastern part. Consequently, the activity rate per unit area increases, leading to higher estimated hazard levels.

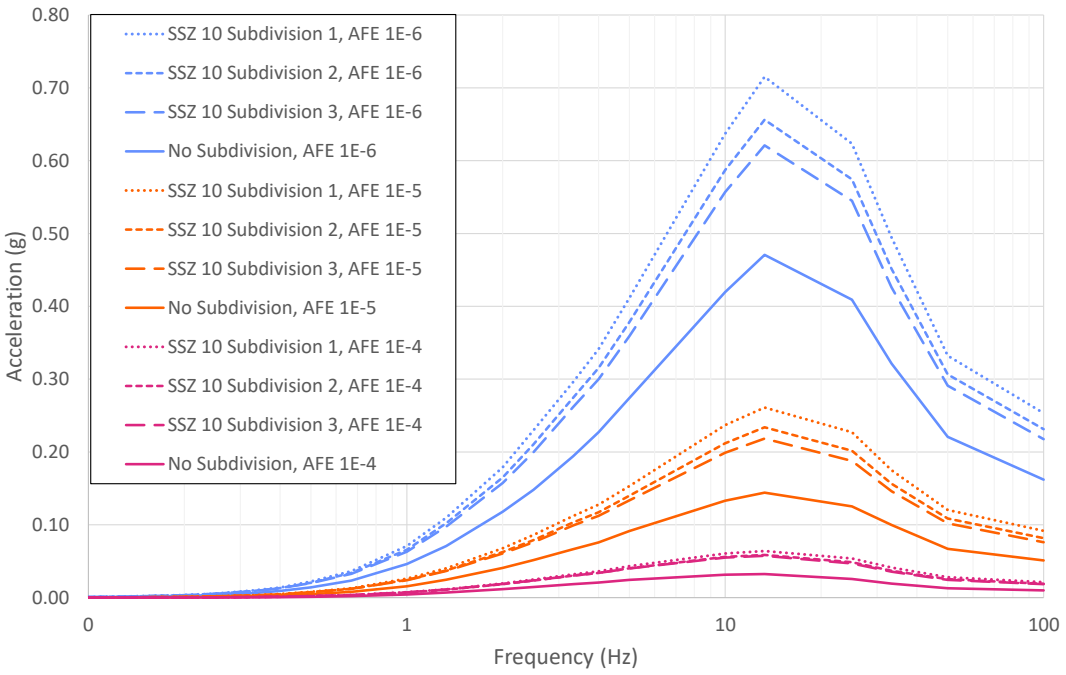

Figure 15: Loviisa mean UHRS at different AFEs using the proposed subdivisions of the source zone 10, compared with the UHRS of the undivided 2016 model [9].

Subdivision 1 produces the smallest western subzone, whereas Subdivision 3 yields the largest. The resulting hazard curves follow this configuration closely: the smaller the western subzone, the higher the estimated hazard, reflecting the increasing spatial concentration of seismicity. When this effect is compared with the impact of the meso model, the two influences are similar in magnitude but opposite in direction.

5.4.3 Loviisa Hazard Estimate with Updated Maximum Magnitude

Figure 16 presents the mean UHRS obtained using the updated $m_{\max}$ distribution, compared to the values reported by Vehmas [9]. Only the distribution truncated to the interval $[5.00, 8.25]$ is shown, as variations in the truncation bounds were confirmed to have no practical effect on the hazard estimate results.

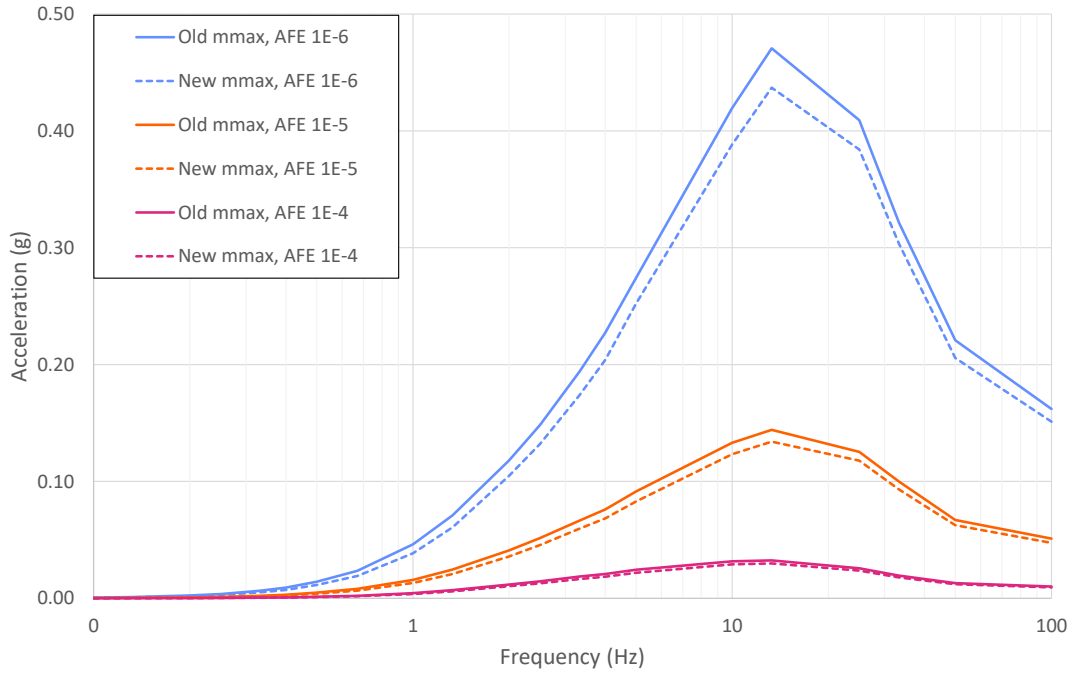

Figure 16: Loviisa mean UHRS at different AFEs using the updated $m_{\max}$ distribution. The UHRS curves labelled "old $m_{\max}$" are from Vehmas [9].

The updated maximum magnitude distribution consistently reduces the hazard estimate across all frequencies and AFEs. The magnitude of this reduction increases with acceleration level but remains largely independent of frequency, meaning that the overall shape of the UHRS curves remains nearly unchanged. The estimated hazard decreases simply because the updated $m_{\max}$ distribution assigns less probability mass to the largest magnitudes compared with the distributions used in earlier PSHAs.

5.5 Olkiluoto Seismic Hazard Estimate Sensitivity

The seismic hazard calculations for Olkiluoto were carried out using the same modelling alternatives as for Loviisa, with the exception of the SSZ 10 subdivisions, which are only relevant to Loviisa's host zone. As before, additional hazard plots and complementary visualisations can be found in Appendix D.

5.5.1 Olkiluoto Hazard Estimate with 2025 SSZ Models

Figure 17 shows the mean UHRS for the 2025 micro and meso models compared with the 2016 model results. Neither of the updated models produces substantial changes to the Olkiluoto hazard estimate. The largest differences appear at AFEs below 10^{-6} and at frequencies above 10 Hz. In contrast to the situation at Loviisa, the micro model leads to a modest reduction in the estimated hazard, while the meso model results in a slight increase.

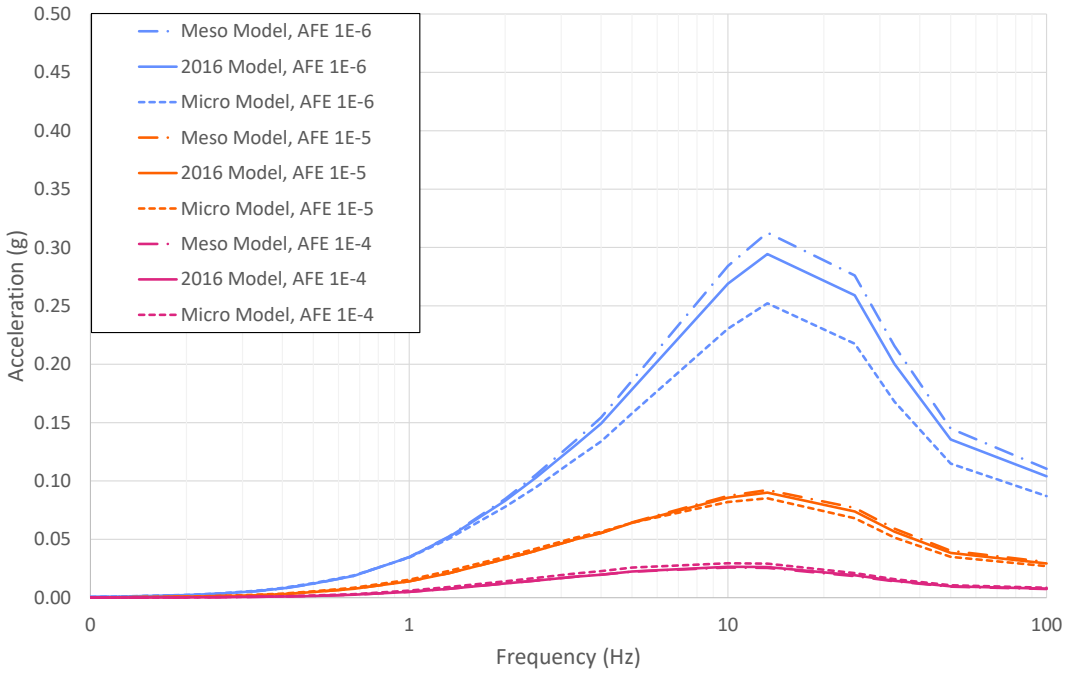

Figure 17: Olkiluoto mean UHRS at different AFEs using the 2025 micro and meso models. The 2016 model corresponds to the results of Vehmas [9] and is included for comparison.

This behaviour can be understood by examining the source zone contributions in Figure 18. At low acceleration levels, the SE-NE zone contributes most significantly to the estimated hazard because of its relatively high seismicity rates. As the acceleration level increases, however, the hazard estimate becomes dominated by the FI-S zone that hosts the Olkiluoto site. This transition reflects the general behaviour of ground-motion attenuation: earthquakes occurring farther from the site must be considerably larger to produce the same levels of ground motion as smaller, nearby events.

A similar pattern is visible in the meso-model results in Figure 19. At low accelerations, the SE-NE zone again accounts for most of the estimated hazard, while at higher accelerations the FI-EE zone dominates. Because FI-EE combines micro-level zones such as FI-C and SK—both more active than FI-S—the meso model produces correspondingly higher hazard estimate levels for Olkiluoto than the micro model. It should also be noted that, as discussed in Section 3.1, the last four years of the utilised FENCAT21 version [10] are only fully covered for the area corresponding to the micro SSZ model. As a result, the seismicity of the more distant SE and BB zones in the meso model is slightly underestimated. However, these effects are considered negligible with respect to the final hazard estimates.

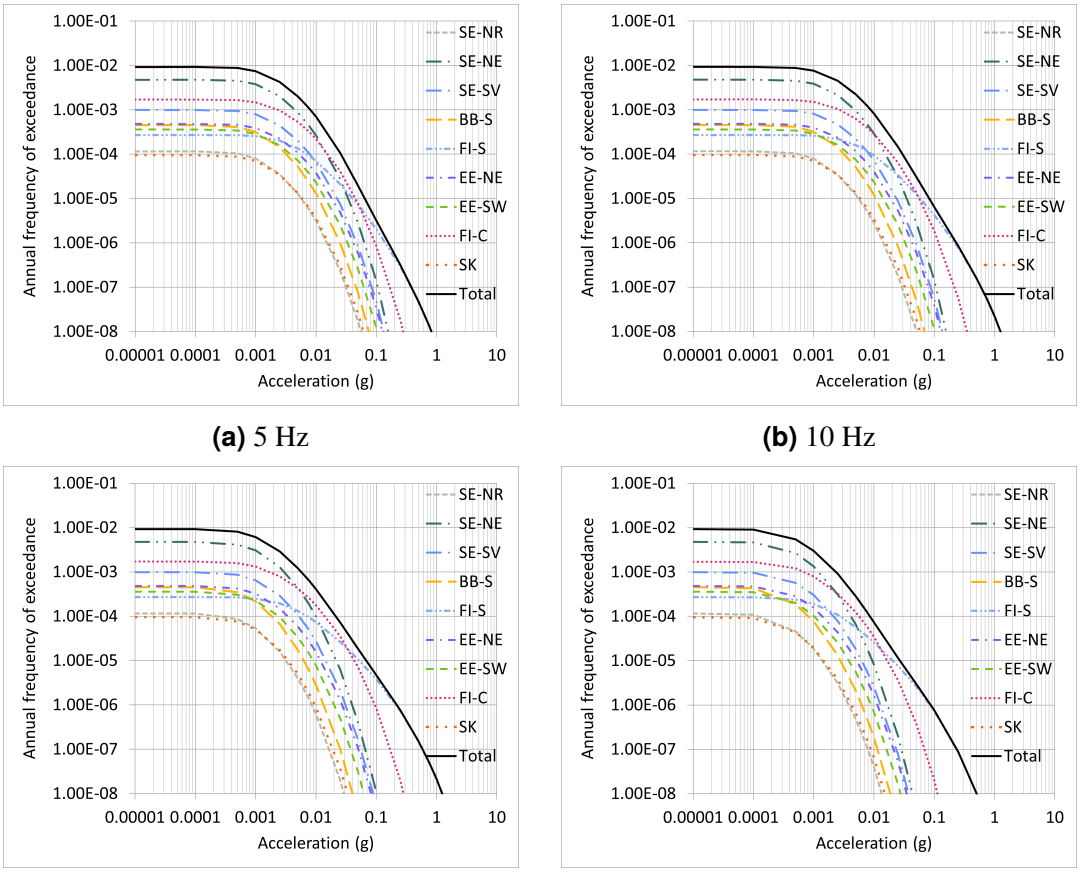

(a) 5 Hz

(b) 10 Hz

(c) 25 Hz

(d) 100 Hz

Figure 18: Olkiluoto mean hazard curves by micro SSZ and the total mean at different frequencies.

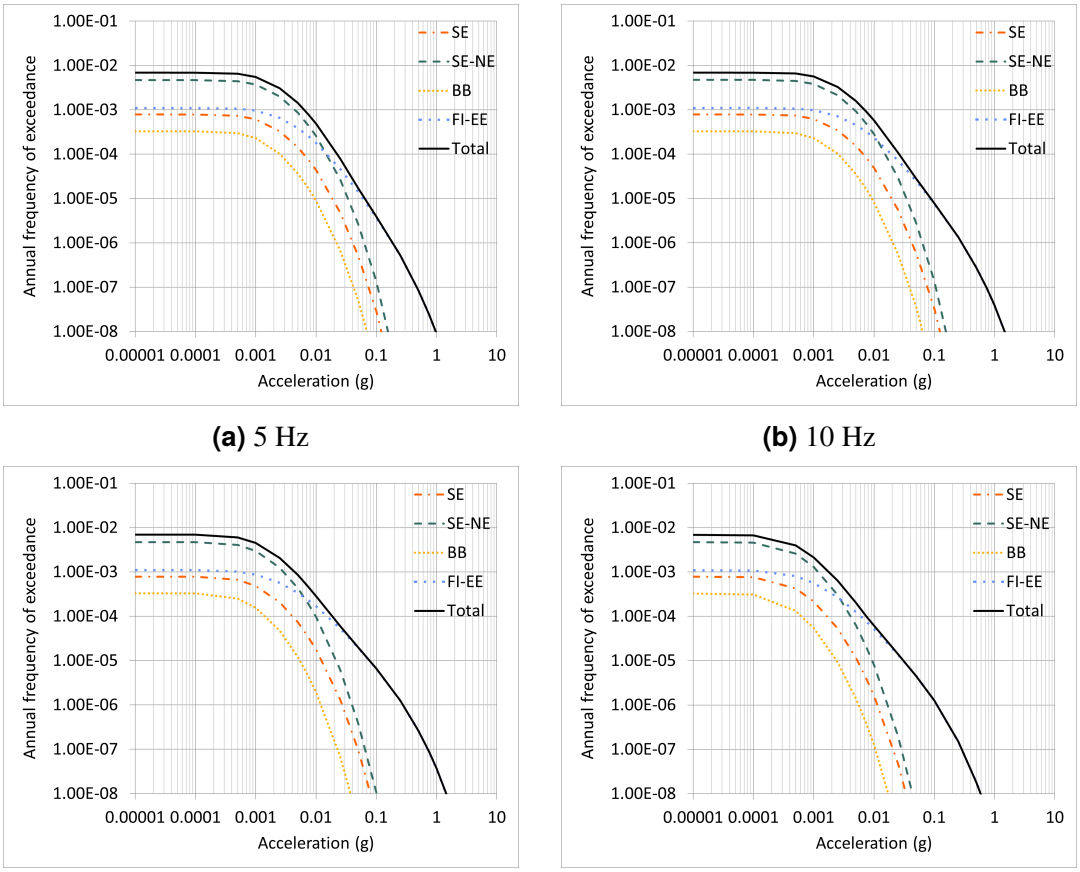

(a) 5 Hz

(b) 10 Hz

(c) 25 Hz

(d) 100 Hz

Figure 19: Olkiluoto mean hazard curves by meso SSZ and the total mean at different frequencies.

5.5.2 Olkiluoto Hazard Estimate with Updated Maximum Magnitude

The effect of the updated $m_{\max}$ distribution on the Olkiluoto UHRS is shown in Figure 20. The pattern mirrors that observed for Loviisa: the updated distribution produces a uniform decrease in the estimated hazard across all AFEs and frequencies. However, because the absolute acceleration levels at Olkiluoto are lower, the corresponding absolute decreases are proportionally smaller. The relative reduction nevertheless scales consistently with ground-motion amplitude.

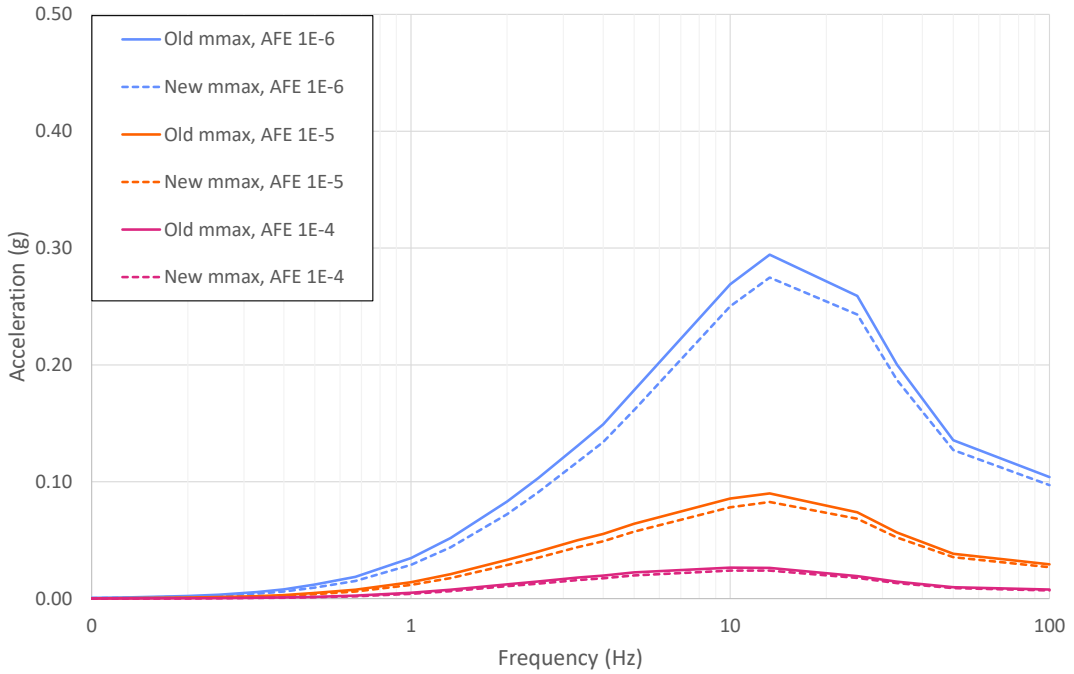

Figure 20: Olkiluoto mean UHRS at different AFEs with the updated $m_{\max}$ distribution. The curves labelled "old $m_{\max}$" are from Vehmas [9].

Overall, the relatively modest impact of the updated maximum magnitude distribution at both Finnish nuclear sites aligns with the general understanding that the seismic hazard at practical AFEs in Finland is driven primarily by the rates of small-to-moderate earthquakes rather than by the extreme tail of the magnitude distribution. Consequently, the hazard estimates remain fairly robust to reasonable adjustments of $m_{\max}$. Nevertheless, adopting a maximum magnitude distribution that better reflects the low-seismicity context of Fennoscandia can still eliminate some conservatism from the model.

6 Discussion and Conclusions

This thesis examined the seismic hazard estimate sensitivity of nuclear sites in Finland to two key components of PSHA: (i) the delineation of SSZs and (ii) the modelling of the maximum magnitude. The SSZ-related analyses were conducted using pre-existing Fennoscandian earthquake catalogues, while a broader SCR catalogue was updated to support the development of an updated $m_{\max}$ model. Throughout, the hazard estimate results of Vehmas [9] were used as a reference, and the computational configuration closely followed his implementation, which itself is largely based on the 2021 Loviisa PSHA formulation [65].

Seismic Source Zone Models

A key premise behind SSZ-based PSHA is that earthquake occurrence is spatially uniform within each zone. To examine how well the considered zoning models support this assumption, nearest neighbour clustering tests were applied to the 2016 SSZ model and to the 2025 micro and meso models.

The results show statistically significant clustering in essentially all tested configurations, which in the strictest interpretation speaks against uniformity. However, such clustering behaviour is likely difficult to avoid in practice: seismicity patterns evolve over long time horizons, whereas the completeness periods of the Fennoscandian catalogues are relatively short and may not fully capture the long-term spatial characteristics of seismicity. Consequently, clustering-test outcomes should be interpreted primarily as diagnostic indicators that inform model selection and uncertainty representation rather than as definitive grounds for rejecting SSZ-based models altogether.

From a site-hazard-estimation perspective, the 2025 micro model closely reproduces the behaviour of the 2016 model: clustering patterns are similar, and the resulting hazard curves differ only modestly from the reference calculations. In this context, replacing the 2016 model with the 2025 micro model is reasonable, as the latter incorporates the additional data that have accumulated since the previous zoning and reflects the most recent expert consensus on SSZ delineation.

The meso model, in contrast, produces more pronounced changes in the estimated hazard, particularly at Loviisa, where the broader zoning dilutes the concentrated seismicity near the site and therefore reduces the hazard estimate at low AFEs. This behaviour is consistent with its stronger clustering signal and reflects its modelling philosophy: instead of following fine-grained seismic patterns, the model emphasises broader tectonic structures, thereby acknowledging the epistemic uncertainty in using small events to infer the occurrence of large earthquakes, whose governing processes remain largely unknown [15].

At the same time, the assumption of seismic similarity across such extensive areas is challenged by the clustering test results, which show that the meso-level zones are markedly less uniform than the micro zones and therefore caution against using the meso model as the primary representation of the seismicity. Consequently, the meso

model may be included in the logic tree to capture the epistemic uncertainty associated with the appropriate spatial scale of zoning, but it should be assigned a noticeably smaller weight than the micro-scale zoning.

Finally, the potential subdivisions of SSZ 10 at Loviisa represent the opposite modelling direction: refining the zoning to reflect the observed spatial concentration of earthquakes in the western portion of the host zone. All subdivision alternatives significantly increase the estimated hazard because of increased seismicity rates per unit area in the western subzone. However, in the absence of supporting geological evidence, and given that seismic patterns typically evolve over timescales far longer than the span of the available catalogue, it is still uncertain whether this concentration reflects long-term behaviour [4, 72]. It is also plausible that the shallow, low-magnitude swarms within the rapakivi do not reflect the deeper seismogenic processes that generate damaging earthquakes beneath the rapakivi, and are therefore of limited relevance for seismic hazard evaluation.

Moreover, none of the tested subdivisions improve the clustering result with particularly high confidence, suggesting that the clusters are either so localised that capturing them perfectly would require an unrealistically small source zone, or that they cannot be meaningfully resolved with such simple geometric divisions at all. Further work is therefore needed to determine whether a more defensible boundary can be identified. If no robust alternative emerges, a pragmatic option could be to partition the zone into equally sized segments using a straight north–south division. Nonetheless, regardless of the eventual implementation, the subdivision is best represented as a low-weight epistemic branch: it acknowledges a plausible, high-impact uncertainty without unjustifiably redefining the base zoning.

Maximum Magnitude

The second major component of this thesis was the development of an updated $m_{\max}$ model for Fennoscandia. Because the regional catalogue is too sparse to constrain the upper tail of the magnitude distribution, a geological-age-based selection of analogue SCR domains was used to construct a new Bayesian prior. This Fennoscandia-specific prior has a lower mean than the SCR priors used in earlier Finnish PSHAs and, when combined with the pre-existing Kijko distribution, leads to systematically lower discretised $m_{\max}$ values.

A purely Bayesian treatment was not adopted because the local data have too little updating power and the posterior would be almost entirely determined by the prior, contrary to the intent of the method. Instead, following the approach adopted in the most recent Finnish PSHAs [65, 86], the Kijko and Bayesian distributions were combined with equal weights. This choice reflects the remaining uncertainty regarding the applicability of the Kijko method under the sparse-seismicity conditions of Fennoscandia while still allowing its information to contribute meaningfully to the final estimate.

Incorporating the resulting $m_{\max}$ distribution into the hazard calculations produces a stable but modest estimated hazard reduction at both nuclear sites. Sensitivity tests show that the lower truncation bound of the distribution influences the discrete $m_{\max}$ values more strongly than the upper bound, yet neither bound materially affects site hazard estimates. These results support adopting the updated truncation interval $[5.0, 8.25]$ and the new Fennoscandian prior in future PSHAs for Loviisa and Olkiluoto.

Suggested Adaptation

Following the conclusions outlined above, a practical way to incorporate the various modelling alternatives into a coherent PSHA framework is illustrated in Figure 21. In this adaptation, the 2016 SSZ model is replaced entirely by the 2025 models. The branch weights—set at 75 % for the micro model and 25 % for the meso model—were established through a panel discussion with representatives from Fortum, TVO, and the Institute of Seismology at UH. Within the micro model, subdivision of Loviisa's host zone (SK, corresponding to SSZ 10) is included with one quarter of the weight of the overall model. All branches of the logic tree share the same maximum magnitude model, implemented as a discrete approximation of the combined Kijko and Bayesian distributions.

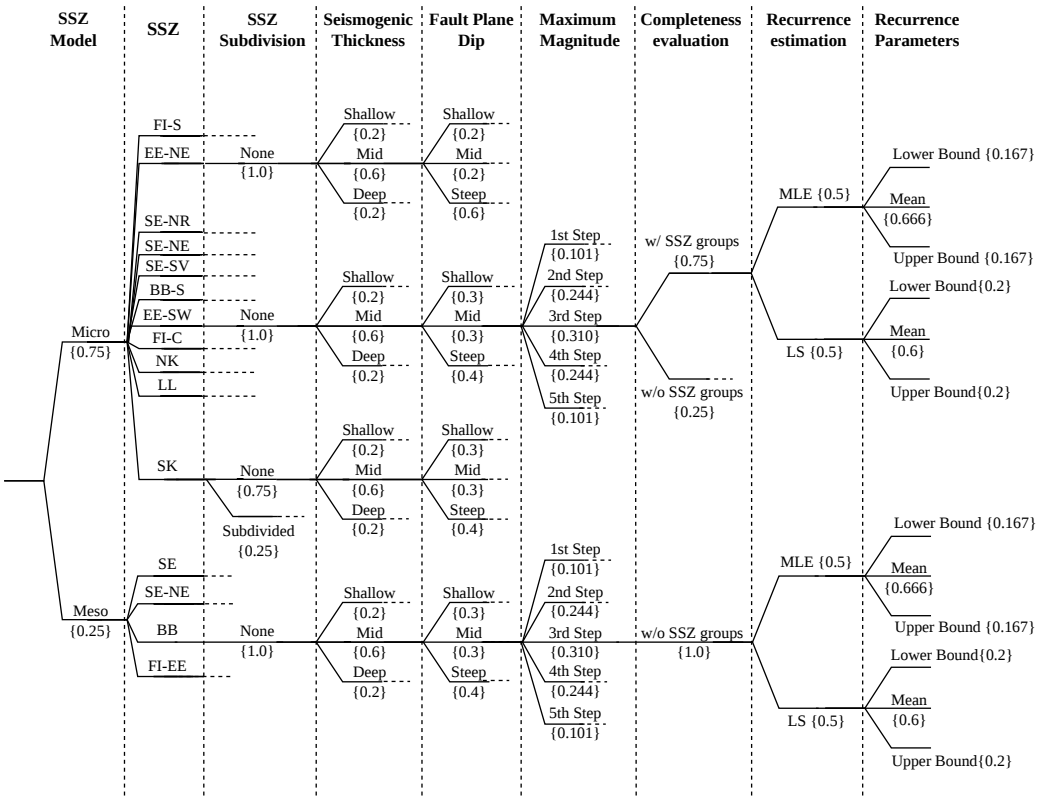

Figure 21: Logic tree to simultaneously incorporate the alternative modelling decisions discussed in this thesis. Suggested branch weights are shown in braces.

In current PSHA practice, branch weights represent the degree-of-belief of the analyst or expert panel in the plausibility of each alternative and are, by design, subjective probabilities [16]. Nonetheless, the weighting choices presented here follow the qualitative guidance derived from the analyses of this thesis: the unmodified micro model represents the most credible baseline depiction of regional seismicity; the meso model serves as a broader, lower-resolution alternative that captures uncertainty related to the zoning process; and the Loviisa host-zone subdivision captures a plausible, though unverified, spatial feature with potentially large hazard implications.

In its current form, the suggested framework is applicable mainly to the Olkiluoto site, as its hazard estimate is insensitive to the method of subdividing the Loviisa source zone, which has not yet been established. Without implementing the subdivision at all, the resulting hazard estimate for Loviisa decreases modestly relative to the results of Vehmas [9], primarily because of the reductive influences of the meso model and the updated maximum magnitude. Once the proposed subdivision and its suggested weight are incorporated, the final estimate is expected to align closely with the results of Vehmas. At Olkiluoto, the overall hazard decreases slightly, driven mainly by the micro model and the updated maximum magnitude distribution. Detailed hazard curves and numerical comparisons for this configuration are provided in Appendix D.

Before adopting any of these adjustments in official hazard assessments, several additional refinements would be advisable. In this work, the completeness analysis for the micro model was inferred indirectly from the corresponding 2016 zones and should be reassessed directly in future studies. Although this is not expected to alter the hazard significantly, it would strengthen the internal consistency of the modelling. Furthermore, efforts should be directed toward constructing a fully declustered version of the FENCAT21 catalogue that also includes the most recent observations for the entire meso-model region. For the Loviisa source zone in particular, the earthquake swarms present in the catalogue should be treated as far as possible so that their hazard implications can be evaluated more reliably in future analyses.

References

[1] Radiation and Nuclear Safety Authority (STUK). Guide YVL B.7, Provisions for internal and external hazards at a nuclear facility, 2019. [Online]. https://www.stuklex.fi/en/ohje/YVLB-7 (Accessed: 29 September 2025).

[2] G. Shin and O. Song. A time-domain method to generate artificial time history from a given reference response spectrum. *Nuclear Engineering and Technology*, 48(3):831–839, 2016.

[3] C. A. Cornell. Engineering seismic risk analysis. *Bulletin of the Seismological Society of America*, 58(5):1583–1606, 1968. Errata 59:1733.

[4] S. Burck, J. Holmberg, M. Lahtinen, O. Okko, J. Sandberg, and P. Välikangas. Sensitivity study of seismic hazard prediction in Finland (SENSEI). Technical report, Radiation and Nuclear Safety Authority (STUK), Vantaa, Finland, 2023.

[5] L. Fülöp. Review of Loviisa seismic hazard reports. Technical report, Technical Research Centre of Finland (VTT), Espoo, Finland, 23 March 2022. VTT-CR-00303-22.

[6] V. Visakorpi. Sensitivity analysis of a seismic hazard assessment for a Finnish nuclear power plant. Master's thesis, Aalto University, School of Science, Espoo, Finland, 2022.

[7] Slate Geotechnical Consultants, Inc. Comments on re-evaluation of seismic hazard at Loviisa and Olkiluoto NPP sites. Technical report, 17 June 2020. LO1-T84252-00014Liite1.

[8] P. Mäntyniemi. A review of probabilistic seismic hazard analysis of Loviisa and Olkiluoto based on a master's thesis. Technical report, Institute of Seismology, University of Helsinki, 18 July 2025.

[9] J. Vehmas. Probabilistic seismic hazard analysis for nuclear power plant sites in Finland. Master's thesis, Aalto University, School of Science, Espoo, Finland, 2024.

[10] University of Helsinki, Institute of Seismology. Homogenized and declustered earthquake catalogue for Northern Europe (1467–2021). LO1-T84252-00024.

[11] P. Mäntyniemi, L. Fülöp, K. Oinonen, N. Junno, E. Kosonen, and A. Korja. A zoning model for seismic hazard analysis of Finland and adjacent areas: A fusion of seismological and geological data. *Tectonophysics*, 907:230757, 2025.

[12] P. Mäntyniemi, L. Fülöp, E. Asikainen, G. Toro, and O. Okko. Bayesian prior distribution of the maximum credible magnitude, Mmax, for Fennoscandia: Sensitivity of the methodology to data characteristics. Research manuscript, 2026.

[13] International Atomic Energy Agency (IAEA). *Seismic Hazards in Site Evaluation for Nuclear Installations*. Vienna, Austria, 2022. No. SSG-9 (Rev. 1).

[14] J. Baker, B. Bradley, and P. Stafford. *Seismic Hazard and Risk Analysis*. Cambridge University Press, 2021.

[15] L. Fülöp, P. Mäntyniemi, M. Malm, G. Toro, M. J. Crespo, et al. Probabilistic seismic hazard analysis in low-seismicity regions: An investigation of sensitivity with a focus on Finland. *Natural Hazards*, 116:111–132, 2023.

[16] J. J. Bommer and F. Scherbaum. The use and misuse of logic trees in probabilistic seismic hazard analysis. *Earthquake Spectra*, 24(4):997–1009, 2008.

[17] F. Mulargia, P. B. Stark, and R. J. Geller. Why is probabilistic seismic hazard analysis (PSHA) still used? *Physics of the Earth and Planetary Interiors*, 264:63–75, 2017.

[18] R. J. Geller. Shake-up time for Japanese seismology. *Nature*, 472:407–409, 2011.

[19] S. Stein, R. J. Geller, and M. Liu. Why earthquake hazard maps often fail and what to do about it. *Tectonophysics*, 562-563:1–25, 2012.

[20] C. F. Richter. An instrumental earthquake magnitude scale. *Bulletin of the Seismological Society of America*, 25(1):1–32, 1935.

[21] B. Gutenberg and C. F. Richter. Earthquake magnitude, intensity, energy, and acceleration (second paper). *Bulletin of the Seismological Society of America*, 46(2):105–145, 1956.

[22] E. M. Scordilis. Empirical global relations converting MS and mb to moment magnitude. *Journal of Seismology*, 10(2):225–236, 2006.

[23] B. Gutenberg. Amplitude of P, PP, and S and magnitudes of shallow earthquakes. *Bulletin of the Seismological Society of America*, 35:57–69, 1945.

[24] B. Gutenberg. Amplitudes of surface waves and magnitudes of shallow earthquakes. *Bulletin of the Seismological Society of America*, 35:3–12, 1945.

[25] T. C. Hanks and H. Kanamori. A moment magnitude scale. *Journal of Geophysical Research: Solid Earth*, 84(B5):2348–2350, 1979.

[26] D. Di Giacomo, I. Bondár, D. A. Storchak, E. R. Engdahl, P. Bormann, and J. Harris. ISC-GEM: Global instrumental earthquake catalogue (1900–2009), III. Re-computed M_S and m_b, proxy M_W, final magnitude composition and completeness assessment. *Physics of the Earth and Planetary Interiors*, 239:33–47, 2015.

[27] C. A. Cornell and S. R. Winterstein. Temporal and magnitude dependence in earthquake recurrence models. *Bulletin of the Seismological Society of America*, 78(4):1522–1537, 1988.

[28] Min-Hao Wu, J. P. Wang, and Kai-Wen Ku. Earthquake, Poisson and Weibull distributions. *Physica A: Statistical Mechanics and its Applications*, 526:121001, 2019.

[29] J.K. Gardner and L. Knopoff. Is the sequence of earthquakes in Southern California, with aftershocks removed, Poissonian? *Bulletin of the Seismological Society of America*, 64(5):1363–1367, 1974.

[30] B. A. Assinovskaya, I. P. Gabsatarova, N. M. Panas, and M. Uski. Seismic events in 2014–2016 around the Karelian Isthmus and their nature. *Seismic Instruments*, 55(1):24–40, 2019.

[31] M. Uski, K. Oinonen, B. Lund, H. Soosalu, L. Ottemöller, et al. FENCAT – an update of the Fennoscandian earthquake catalogue. *Geophysical Journal International*, 242(3):1–18, 2025.

[32] S. Tinti and F. Mulargia. Completeness analysis of a seismic catalog. *Annales Geophysicae*, 3:407–414, 1985.

[33] A. Ansari, F. Zahoor, K. S. Rao, and A. K. Jain. Seismic hazard assessment studies based on deterministic and probabilistic approaches for the Jammu region, NW Himalayas. *Arabian Journal of Geosciences*, 15(11):1–26, 2022.

[34] C. Gouache, P. Tinard, and F. Bonneau. Stochastic generator of earthquakes for mainland France. *Applied Sciences*, 12:571, 2022.

[35] J. C. Stepp. Analysis of completeness of the earthquake sample in the Puget Sound area and its effect on statistical estimates of earthquake hazard. In *Proceedings of the International Conference on Microzonation*, volume 2, pages 897–910, Seattle, 1972.

[36] M. Wyss, D. Schorlemmer, and S. Wiemer. Mapping asperities by minima of local recurrence time: San Jacinto–Elsinore fault zones. *Journal of Geophysical Research: Solid Earth*, 105(B4):7829–7844, 2000.

[37] S. Wiemer and M. Wyss. Minimum magnitude of completeness in earthquake catalogs: Examples from Alaska, the western United States, and Japan. *Bulletin of the Seismological Society of America*, 90(4):859–869, 2000.

[38] P. Mäntyniemi, R. Wahlström, C. Lindholm, and A. Kijko. Seismic hazard in Fennoscandia: A regionalized study. *Tectonophysics*, 227:205–213, 1993.

[39] G. Grünthal and the GSHAP Region 3 Working Group. Seismic hazard assessment for Central, North and Northwest Europe: GSHAP Region 3. *Annali di Geofisica*, 42:999–1011, 1999.

[40] R. Wahlström and G. Grünthal. Probabilistic seismic hazard assessment (horizontal PGA) for Fennoscandia using the logic tree approach for regionalization and nonregionalization models. *Seismological Research Letters*, 72(1):33–45, 2001.

[41] A. Korja and E. Kosonen (editors). Seismotectonic framework and seismic source area models in Fennoscandia, northern Europe. Technical report, Institute of Seismology, University of Helsinki, Finland, 2015. Report S-63.

[42] A. Korja, S. Kihlman, and K. Oinonen (editors). Seismic source areas in central Fennoscandia. Technical report, Institute of Seismology, University of Helsinki, Finland, 2016. Report S-64, LO1-T84252-00003.

[43] M. Uski, T. Tiira, A. Korja, and S. Elo. The 2003 earthquake swarm in Anjalankoski, south-eastern Finland. *Tectonophysics*, 422(1):55–69, 2006.

[44] P. Mäntyniemi. Revisiting Svenskby, southeastern Finland: Communications regarding low-magnitude earthquakes in 1751–1752. *Geosciences*, 12(9):338, 2022.

[45] P. Mäntyniemi. Geologi Hugo Berghell ja Viipurin rapakiven tärinät 1899–1900. *Geologi*, 75:77–81, 2023.

[46] J. Maffei and P. Bazzurro. The 2002 Molise, Italy, earthquake. *Earthquake Spectra*, 20(S1):1–358, 2004.

[47] C. Meletti, F. Galadini, G. Valensise, M. Stucchi, R. Basili, et al. A seismic source zone model for the seismic hazard assessment of the Italian territory. *Tectonophysics*, 450(1):85–108, 2008.

[48] S. Ma, D. Motazedian, and M. Lamontagne. Further studies on the 1988 Mw 5.9 Saguenay, Quebec, earthquake sequence. *Canadian Journal of Earth Sciences*, 55(10):1115–1128, 2018.

[49] S. Gregersen, P. Wiejacz, W. Debski, B. Domanski, B. A. Assinovskaya, et al. The exceptional earthquakes in Kaliningrad district, Russia on September 21, 2004. *Physics of the Earth and Planetary Interiors*, 164(1–2):63–74, 2007.

[50] A. A. Nikonov and H. Sildvee. Historical earthquakes in Estonia and their seismotectonic position. *Geophysica*, 27(1–2):79–93, 1991.

[51] M. A. Chinnery. Investigations of the seismological input to the safety design of nuclear power reactors in New England. Technical Report NUREG/CR-0563, U.S. Nuclear Regulatory Commission, Washington, D.C., 1979.

[52] C. A. Cornell and E. H. Vanmarcke. The major influences on seismic risk. In *Proceedings of the Fourth World Conference on Earthquake Engineering*, volume 1, pages 69–83, Santiago, Chile, 1969. Session A–1.

[53] R. L. Wheeler. Methods of Mmax estimation east of the Rocky Mountains. Technical report, U.S. Geological Survey, Reston, Virginia, 2009. Open-File Report 2009–1018.

[54] A. Kijko. Estimation of the maximum earthquake magnitude, mmax. *Pure and Applied Geophysics*, 161, 2004.

[55] D. L. Wells and K. J. Coppersmith. New empirical relationships among magnitude, rupture length, rupture width, rupture area, and surface displacement. *Bulletin of the Seismological Society of America*, 84(4):974–1002, 1994.

[56] L. Swafford and S. Stein. Limitations of the short earthquake record for seismicity and seismic hazard studies. In S. Stein and S. Mazzotti, editors, *Continental Intraplate Earthquakes: Science, Hazard, and Policy Issues*, volume 425 of *Geological Society of America Special Paper*. Geological Society of America, 2007.

[57] A. C. Johnston, K. J. Coppersmith, L. R. Kanter, and C. A. Cornell. The earthquakes of stable continental regions: Assessment of large earthquake potential. Technical report, Electric Power Research Institute (EPRI), Palo Alto, California, 1994.

[58] K. Vanneste, B. Vleminckx, S. Stein, and T. Camelbeeck. Could Mmax be the same for all stable continental regions? *Seismological Research Letters*, 87(5):1214–1223, 2016.

[59] B. Gutenberg and C. F. Richter. Frequency of earthquakes in California. *Bulletin of the Seismological Society of America*, 34(4):185–188, 1944.

[60] M. Ishimoto and K. Iida. Observations sur les séismes enregistrés par le microsismographe construit dernièrement (1). *Bulletin of the Earthquake Research Institute*, 17:443–478, 1939.

[61] L. Heikkilä. Verification and sensitivity analysis of maximum likelihood estimation for Loviisa NPP seismic hazard. Special assignment. Aalto University, School of Science. Espoo, Finland, 2023.

[62] D. Stromeyer and G. Grünthal. Capturing the uncertainty of seismic activity rates in probabilistic seismic hazard assessments. *Bulletin of the Seismological Society of America*, 105(2A):580–589, 2015.

[63] D. H. Weichert. Estimation of the earthquake recurrence parameters for unequal observation periods for different magnitudes. *Bulletin of the Seismological Society of America*, 70(4):1337–1346, 1980.

[64] J. P. Stewart, J. Douglas, M. Javanbarg, N. Abrahamson, Y. Bozorgnia, et al. Selection of ground motion prediction equations for the Global Earthquake Model. *Earthquake Spectra*, 31(1):19–45, 2015.

[65] Slate Geotechnical Consultants, Inc. Finland probabilistic seismic hazard analysis. Technical report, 21 August 2021. LO1-T84252-00016Liite1.

[66] L. Fülöp, V. Jussila, R. Aapasuo, T. Vuorinen, and P. Mäntyniemi. A ground-motion prediction equation for Fennoscandian nuclear installations. *Bulletin of the Seismological Society of America*, 110(2):1211–1230, 2020.

[67] J. J. Bommer and H. Crowley. The purpose and definition of the minimum magnitude limit in PSHA calculations. *Seismological Research Letters*, 88(4):1097–1106, 2017.

[68] T. Ahjos and M. Uski. Earthquakes in northern Europe in 1375–1989. *Tectonophysics*, 207:1–23, 1992.

[69] K. Oinonen, M. Uski, H. Soosalu, and B. Lund. A joint Fennoscandian earthquake catalogue FENCAT, version FENCAT(2021). Institute of Seismology, University of Helsinki, Finland, January 2025 [Updated on 12 June 2025]. [Online]. https://doi.org/10.23729/fd-50c9011e-1ec8-3779-8a23-173e53931a07 (Accessed: 8 January 2026).

[70] K. Oinonen, M. Uski, H. Soosalu, and B. Lund. A joint Fennoscandian earthquake catalogue FENCAT, subcatalogue FENCAT17_Seismic_risk. Institute of Seismology, University of Helsinki, Finland, May 2024 [Updated on 30 January 2025]. [Online]. https://doi.org/10.23729/201d4846-a5da-4338-944c-2ae53aca9e0c (Accessed: 8 January 2026).

[71] International Atomic Energy Agency (IAEA). *Seismic Hazards in Site Evaluation for Nuclear Installations*. Vienna, Austria, 2010. No. SSG-9.

[72] P. Mäntyniemi, M. Uski, and K. Oinonen. On the boundaries of seismic source area no. 10. Technical report, Institute of Seismology, University of Helsinki, Finland, 23 September 2020. LO1-T84252-00011.

[73] J. Koskenranta and T. Leppänen. Selvitys Loviisan seismisestä lähdealueesta. Technical report, Fortum Power and Heat Oy, Espoo, Finland, 21 January 2021. LO1-T84252-00013.

[74] E. Asikainen. Updated SCR earthquake catalogue, March 2026. [Online]. https://github.com/asikaeel/psha2026-scr-catalogue (Accessed: 4 March 2026).

[75] Electric Power Research Institute (EPRI). Central and Eastern United States seismic source characterization for nuclear facilities. Technical report, Palo Alto, California, 2012. 1021097.

[76] S. M. Schulte and W. D. Mooney. An updated global earthquake catalogue for stable continental regions: Reassessing the correlation with ancient rifts. *Geophysical Journal International*, 161:707–721, 2005.

[77] The International Seismological Centre (ISC). Bulletin of the International Seismological Centre, 2026. [Online]. https://www.isc.ac.uk/iscbulletin/ (Accessed: 2 January 2026).

[78] The International Seismological Centre (ISC). ISC Bulletin: event catalogue search, 2026. [Online]. https://www.isc.ac.uk/iscbulletin/search/catalogue/ (Accessed: 2 January 2026).

[79] J. Vehmas and J. Koskenranta. Loviisa probabilistic seismic hazard analysis - Additional studies related to Gutenberg–Richter parameters. Technical report, Fortum Power and Heat Oy, Espoo, Finland, 8 January 2024. LO1-T84252-00021.

[80] R. M. W. Musson. Evaluation of seismic hazard source models. In J. K. Lapajne and R. Vidrih, editors, *Seismicity Modelling in Seismic Hazard Mapping*, pages 53–66. Slovenian Geophysical Survey, Ljubljana, 2000.

[81] T. Lipták. On the combination of independent tests. *Magyar Tudományos Akadémia Matematikai Kutató Intézetének Közleményei*, 3:171–197, 1958.

[82] M. H. DeGroot and M. J. Schervish. *Probability and Statistics*, chapter 10.6 Kolmogorov-Smirnov Tests, pages 657–665. Addison-Wesley, Boston, MA, 4th edition, 2012.

[83] P. Koskinen. Orientation of faults and their potential for reactivation in the present stress field in Finland. Master's thesis, Department of Physics, University of Helsinki, 2013.

[84] J. Saari and M. Malm. Re-evaluation of seismic hazard in Olkiluoto and Loviisa. Technical report, ÅF-Consult Ltd, 2016. LO1-T84252-00004.

[85] T. Leppänen. Re-evaluation of seismic hazard in Loviisa NPP site. Technical report, Fortum Power and Heat Oy, Espoo, Finland, 19 December 2018. LO1-T84252-00007.

[86] J. Vehmas. Loviisa probabilistic seismic hazard analysis - 2024 update. Technical report, Fortum Power and Heat Oy, Espoo, Finland, 28 November 2024. LO1-T84252-00023.

[87] T. Tran, A. Dao, E. Asikainen, E. Stenberg, and W. Sorjonen. Probabilistic seismic hazard analysis for a nuclear power plant. Final report on the course *MS–E2177 – Seminar on Case Studies in Operations Research*, Aalto University, School of Science, 2025. [Online]. https://sal.aalto.fi/files/teaching/ms-e2177/2025/index.html (Accessed: 12 January 2026).

[88] A. Gelman, J.B. Carlin, H.S. Stern, D.B. Dunson, A. Vehtari, and D.B. Rubin. *Bayesian Data Analysis*. Chapman & Hall/CRC, 3rd edition, 2013.

[89] A. C. Miller and T. R. Rice. Discrete approximations of probability distributions. *Management Science*, 29(3):352–362, 1983.

[90] N. Abrahamson. HAZ45.3, 2023. [Online]. https://github.com/abrahamson/HAZ (Accessed: 10 October 2025).

[91] C. Goulet, Y. Bozorgnia, N. Abrahamson, N. Kuehn, L. A. Atik, et al. Central and Eastern North America ground-motion characterization: NGA-East final report. Technical report, Pacific Earthquake Engineering Research Center, University of California, 2018.

[92] Esri Inc. ArcGIS Pro 3.5.3, 2025. [Online.] https://www.esri.com/en-us/arcgis/products/arcgis-pro/overview (Accessed: 9 December 2025).

[93] N. Abrahamson. Fractiles 45.3, 2023. [Online]. https://github.com/abrahamson/Fractiles (Accessed: 30 January 2026).

A Updated SCR Database

This appendix describes the process of updating the SCR catalogue and lists the domain-wise parameters used in the Bayesian maximum magnitude assessment. The full dataset is available on GitHub [74].

A.1 Catalogue Processing

The process of updating the SCR earthquake catalogue consisted of three main steps:

1. retrieving the data from the Reviewed ISC Bulletin (discussed in Section 3.3.2),
2. harmonising magnitude types listed in the bulletin, and
3. removing duplicate events arising from overlapping coverage.

Magnitude Conversions

In an effort to produce a uniform earthquake catalogue from the ISC catalogue, its various magnitude types were harmonised to the same M_W scale used in the EPRI catalogue. To achieve this, all events in the catalogue with multiple listed magnitudes associated with the prime hypocentre were filtered so that only one magnitude type was included. The magnitude type was selected in the order of preference

$$M_W \succ M_S \succ m_b \succ \text{any other available magnitude},$$

where M_S denotes the surface-wave magnitude scale and m_b is the short-period body-wave magnitude scale.

The magnitudes listed in M_W were accepted as such (two observations in the dataset). For events reported with M_S or m_b, the magnitudes were converted to M_W using the empirical exponential models of the form $My = \exp\{a + b \cdot Mx\} + c$ presented by Di Giacomo et al. [26]. The conversion from M_S to M_W is given by

$$M_W = \exp\{-0.222 + 0.233\, M_S\} + 2.863, \tag{A1}$$

with standard errors for the coefficients a, b, and c of 0.043, 0.004, and 0.056, respectively. Similarly, the conversion from m_b to M_W is

$$M_W = \exp\{-4.664 + 0.859\, m_b\} + 4.555, \tag{A2}$$

with corresponding coefficient standard errors 0.085, 0.012, and 0.017.

These relations were originally developed for the magnitude ranges $M_S \geq 5.0$ and $m_b \in [4.5, 6.5]$. In the ISC catalogue, all reported m_b values fell within the valid range. However, a total of 53 observations with $M_S \in [4.5, 5.0)$ had to be discarded. A subsequent sensitivity check showed that this decision had only a negligible influence on the results: the bias-corrected mean of the m_{max} distribution remained at 6.04, while the standard error decreased from 0.60 to 0.59.

The uncertainty introduced by the magnitude transformations was accounted for by propagating the errors associated with the coefficients of Equations (A1) and (A2). The standard deviation of the converted moment magnitude is expressed as

$$\begin{aligned}\sigma_{\mathrm{M_W}} &= \sqrt{\left(\frac{\partial \mathrm{M_W}}{\partial a}\sigma_a\right)^2 + \left(\frac{\partial \mathrm{M_W}}{\partial b}\sigma_b\right)^2 + \left(\frac{\partial \mathrm{M_W}}{\partial c}\sigma_c\right)^2} \\ &= \sqrt{(\exp\{a + bMx\} \cdot \sigma_a)^2 + (Mx \cdot \exp\{a + bMx\} \cdot \sigma_b)^2 + (\sigma_c)^2}, \end{aligned} \tag{A3}$$

where the appropriate set of coefficients and magnitude $Mx \in \{\mathrm{M_S}, \mathrm{m_b}\}$ is used depending on the magnitude type that is being converted.

Following magnitude conversion and uncertainty estimation, the ISC catalogue for the selected analogue domains was merged with the EPRI catalogue. In the combined dataset, the expected magnitude $E[\mathrm{M}]$ is taken as the converted moment magnitude, and the associated uncertainty $\sigma[\mathrm{M}]$ corresponds to the Equation (A3). For events originating from the EPRI catalogue, these values were retained without modification.

Because the ISC event catalogue search does not provide uncertainties for the original magnitude estimates, the error introduced by the conversion process represents the sole source of magnitude uncertainty for ISC events. For the two events originally reported in $\mathrm{M_W}$, the resulting $\sigma[\mathrm{M}]$ was set to zero. As these uncertainty estimates are not used to compute the maximum magnitude distribution, these assumptions do not affect the results of this thesis. Nevertheless, if the updated catalogue were to be applied to other analyses, the treatment of magnitude uncertainty should be revisited.

Removal of Duplicate Events

Since the timeframes of the ISC and EPRI catalogues are partially overlapping, some earthquakes appear in both datasets. To prevent double counting, potential duplicate events were identified using a simplified three-criterion matching scheme. Two recordings were considered duplicates of the same earthquake observation if they met the following conditions:

1. they were listed in different catalogues,
2. they had the same calendar day, and
3. they were located within the same domain.

Earlier tests also evaluated distance thresholds and magnitude-difference criteria, but these were ultimately discarded as both conditions had negligible influence on the resulting maximum magnitude distribution.

When overlapping observations were identified, they were merged on an event-by-event basis under the assumption that each catalogue reports only unique earthquakes. For a given domain and day, the catalogue containing the larger number of events determined the number of merged entries to be produced. Each merged entry was created by pairing one event from the larger catalogue with all suitable matching events from the

smaller catalogue such that the magnitude and epicentral coordinates were computed as simple arithmetic means of the contributing observations.

This approach follows directly from the underlying data interpretation: because the events within each catalogue are considered internally unique, the number of distinct earthquakes on that day must be at least as large as the number reported by the larger catalogue. However, because of uncertainties in magnitude estimates and epicentral locations, it is not possible to determine with sufficient confidence which specific events from the two catalogues correspond to the same physical earthquake. Pairing each event from the larger catalogue with all plausible counterparts from the smaller catalogue therefore provides a consistent and conservative merging strategy.

A.2 Domain Parameters of the Updated SCR Catalogue

Table A1 presents the domain-wise parameters for the chosen domains in this thesis that have been derived from the updated SCR earthquake catalogue. Each domain (DN) is characterised by its geographical area, observed maximum magnitude ($m_{\max}^{\text{obs}}$), the number of recorded events (N), and the estimated number of events corrected for catalogue completeness (N^{corr}). The completeness regions and corresponding b-values are based on the work of Johnston et al. [57], while the domain areas were assessed by EPRI [75].

Table A1: Parameters of the selected domains in the updated SCR catalogue.

DN	Area (km^2)	$m_{\max}^{\text{obs}}$ (M_W)	N	N^{corr}	Completeness Region	b-value
3	369 232	5.050	4	4.00	Australia (a)	0.896
7	237 858	6.580	29	40.89	Australia (a)	0.896
8	501 577	5.380	28	28.00	Australia (a)	0.896
9	853 794	6.680	34	47.82	Australia (a)	0.896
10	192 642	5.190	6	6.00	Australia (a)	0.896
13	2 010 402	6.800	66	132.09	Australia (a)	0.896
14	197 610	6.135	5	5.00	Australia (a)	0.896
18	645 753	5.600	1	1.00	Australia (a)	0.896
19	838 499	6.100	10	10.00	Australia (a)	0.896
42	509 261	4.870	1	1.00	South America (a)	1.212
47	941 052	5.140	5	5.00	South America (a)	1.212
48	324 268	5.250	2	2.00	South America (a)	1.212
51	2 130 122	6.420	98	148.15	South America (c)	1.212
52	4 715 337	6.260	46	61.96	South America (c)	1.212
72	1 004 603	6.125	14	25.21	Africa (c)	0.982
73	1 985 264	6.300	27	36.46	Africa (b)	0.982
77	49 528	5.050	2	2.00	Africa (c)	0.982
78	45 208	6.300	2	2.00	Africa (b)	0.982
98	1 128 104	4.825	1	1.00	Africa (a)	0.982
100	1 374 935	6.260	8	8.00	Africa (a)	0.982
106	781 860	6.430	48	73.00	India (a)	0.966
107	79 382	5.810	2	2.00	India (a)	0.966
108	155 035	5.120	1	1.00	India (a)	0.966
109	41 141	5.100	4	4.00	India (a)	0.966
110	142 062	5.805	3	4.97	India (a)	0.966
111	178 946	5.815	11	11.00	India (a)	0.966
112	504 375	6.410	17	22.97	India (a)	0.966
113	810 970	6.950	80	231.33	India (a)	0.966
123	377 393	5.090	3	3.00	China (e)	1.029
133	312 369	6.660	23	31.56	China (b)	1.029
140	229 180	5.190	4	4.00	Russia (a)	1.16
146	296 773	5.370	4	4.00	Russia (a)	1.16
147	750 750	6.590	32	45.65	Russia (b)	1.16
149	2 249 521	6.400	6	6.00	Russia (b)	1.16
163	561 495	5.140	2	2.33	Europe (e)	1.156
164	371 000	5.820	1	1.00	Europe (e)	1.156
166	1 276 933	5.140	4	4.00	Europe (e)	1.156
226	1 297 437	6.550	23	71.69	North America (d)	0.728
230	498 443	6.000	13	20.52	North America (g)	0.728
231	540 467	5.890	28	41.67	North America (h)	0.728
236	2 195 241	6.105	5	5.00	North America (e)	0.728
237	1 344 617	5.720	1	1.00	North America (e)	0.728
238	373 331	5.300	8	10.29	North America (h)	0.728
239	3 882 973	5.430	21	21.00	North America (b)	0.728
241	1 067 319	6.235	18	25.87	North America (e)	0.728
242	550 542	5.270	8	10.26	North America (e)	0.728
244	96 381	5.150	11	11.00	North America (d)	0.728
246	296 714	5.140	4	4.85	North America (d)	0.728
255	601 885	5.430	21	28.71	North America (g)	0.728

B Earthquake Recurrence in Fennoscandia

The earthquake recurrence parameters used as input in the HAZ45 program are obtained using both the MLE and LS methods, following the procedures of Vehmas [9]. The program requires as input the b–value and the recurrence rate at the minimum magnitude $m_{\min}$, defined as

$$n_{\min} = 10^{a - b m_{\min}}.$$

Owing to the original implementation, these are calculated separately using catalogue completeness estimates with and without SSZ groups for the micro SSZs and SSZ 10 subdivisions. For the broader meso-level SSZs, only one set of completeness estimates is used. The completeness intervals corresponding to the 2025 SSZ models are presented in Section 5.1 and Appendix C. A full description of the methods can be found in Vehmas' thesis [9]; the essential formulas are repeated below. In both the LS and MLE estimations, a magnitude bin width of 0.5 M_W is applied.

Least Squares Regression

The LS method is applied to fit the log-linear GR relation to the cumulative annual earthquake rates. The mean LS estimates for the recurrence parameters a and b are given by

$$b = -\frac{\sum_{i=1}^{I} (m_i - \bar{m}) \left[\log_{10}(n(m_i)) - \overline{\log_{10}(n(m_i))} \right]}{\sum_{i=1}^{I} (m_i - \bar{m})^2}, \tag{B1}$$

$$a = \overline{\log_{10}(n(m_i))} + b\bar{m}, \tag{B2}$$

where m_i is the center value of the magnitude bin $i \in [1, I]$, and the overline denotes the mean value. Because the magnitude bins have different completeness periods, the event count in each bin is divided by the corresponding interval length t_i before forming the cumulative annual rates $n(m_i)$.

The confidence intervals for the LS estimates are computed as

$$\left[a_{\mathrm{L}} = a - 1.65\sqrt{\mathrm{var}(a)}, a_{\mathrm{U}} = a + 1.65\sqrt{\mathrm{var}(a)} \right],$$

$$\left[b_{\mathrm{L}} = b - 1.65\frac{\mathrm{cov}(a,b)}{\sqrt{\mathrm{var}(a)}}, b_{\mathrm{U}} = b + 1.65\frac{\mathrm{cov}(a,b)}{\sqrt{\mathrm{var}(a)}} \right],$$

where a and b are the mean LS estimates given by Equations (B2) and (B1), respectively. The corresponding bounds for $n_{\min}$ are

$$\left[n_{\min,\mathrm{L}} = 10^{a_{\mathrm{L}} - b_{\mathrm{L}} m_{\min}}, n_{\min,\mathrm{U}} = 10^{a_{\mathrm{U}} - b_{\mathrm{U}} m_{\min}} \right].$$

In HAZ, a weight of 0.6 is assigned to the mean estimate and a weight of 0.2 to each of the two confidence-bound estimates.

Maximum Likelihood Estimation

Vehmas [9] applied the MLE method to the non-truncated GR model. Because the difference between $m_{\max}$ and the completeness magnitude m_c is several magnitude units for the Fennoscandian catalogue, truncation has negligible influence on the parameter estimates [6, 61]. The catalogue is divided into magnitude bins, and the observed count in each bin n_i is used to solve the MLE equations.

The estimate of β is obtained from

$$\sum_{i=1}^{I} n_i m_i = \frac{N \sum_{i=1}^{I} \exp\{-\beta m_i\} t_i m_i}{\sum_{i=1}^{I} \exp\{-\beta m_i\} t_i}, \tag{B3}$$

where t_i is the completeness period length for magnitude bin i and $N = \sum_{i=1}^{I} n_i$ is the total number of earthquakes in the range $[m_c, m_{\max}]$. Here, $m_{\max} = 6.5$ M_W as in [9]. Equation (B3) can be solved numerically, and its solution is used to solve α from

$$\exp\{\alpha\} = \frac{N}{2 \sinh(\beta \frac{\delta m}{2}) \sum_{i=1}^{I} \exp\{-\beta m_i\} t_i},$$

where $\delta m = 0.5$ is the width of the magnitude bin. The confidence intervals are then computed for $b = \frac{\beta}{\ln(10)}$ and $n_{\min}$ as

$$\left[b_{\mathrm{L}} = b - 1.73\sqrt{\mathrm{var}(b)}, b_{\mathrm{U}} = b + 1.73\sqrt{\mathrm{var}(b)} \right],$$

$$\left[n_{\min,\mathrm{L}} = 10^{a - b m_{\min} - 1.73\sqrt{\mathrm{var}(a - bm)}}, n_{\min,\mathrm{U}} = 10^{a - b m_{\min} + 1.73\sqrt{\mathrm{var}(a - bm)}} \right].$$

B.1 Recurrence Parameters for 2025 SSZ Models

Following the procedures outlined above, Tables B1–B4 present the LS and MLE recurrence parameters for the 2025 micro SSZ model, computed with and without SSZ grouping in the completeness analysis. The recurrence parameters EE-SW, LL, and NK zones, which have a very limited number of earthquakes, were taken from the neighbouring zones. For EE-SW and LL, the parameters are the same as for EE-NE, while the parameters for NK are derived from FI-C. The corresponding meso SSZ parameters, based on completeness estimates from the CUVI method, appear in Tables B5 and B6.

Table B1: Recurrence parameters for the 2025 micro source zones estimated with LS and catalogue completeness with SSZ groups.

SSZ	b	b_L	b_U	$n_{\min}$	$n_{\min,L}$	$n_{\min,U}$
SE-NR	1.0604	0.8247	1.2962	0.0029050	0.0061654	0.0013687
SE-NE	1.1089	0.8192	1.3987	0.0041237	0.0128904	0.0013192
SE-SV	0.9808	0.7200	1.2416	0.0027725	0.0058971	0.0013035
BB-S	1.1703	0.9104	1.4301	0.0041080	0.0094173	0.0017920
FI-S	1.2485	0.9191	1.5778	0.0002775	0.0010137	0.0000760
EE-NE	0.7702	0.5285	1.0119	0.0020169	0.0046349	0.0008776
FI-C	0.9164	0.7129	1.1198	0.0043766	0.0083790	0.0022860
SK	1.5531	0.9345	2.1718	0.0000544	0.0015332	0.0000019

Table B2: Recurrence parameters for the 2025 micro source zones estimated with MLE and catalogue completeness with SSZ groups.

SSZ	b	b_L	b_U	$n_{\min}$	$n_{\min,L}$	$n_{\min,U}$
SE-NR	1.0699	0.9972	1.1426	0.0014431	0.0024371	0.0008545
SE-NE	0.9884	0.9342	1.0426	0.0045827	0.0068693	0.0030573
SE-SV	0.9011	0.7643	1.0379	0.0024350	0.0054055	0.0010969
BB-S	1.0800	1.0304	1.1296	0.0035889	0.0052776	0.0024405
FI-S	1.3476	1.1857	1.5095	0.0000615	0.0001959	0.0000193
EE-NE	0.8498	0.5938	1.1058	0.0004741	0.0024345	0.0000923
FI-C	0.9871	0.8925	1.0816	0.0015455	0.0029005	0.0008235
SK	1.5116	1.3731	1.6501	0.0000272	0.0000775	0.0000095

Table B3: Recurrence parameters for the 2025 micro source zones estimated with LS and catalogue completeness without SSZ groups.

SSZ	b	b_L	b_U	$n_{\min}$	$n_{\min,L}$	$n_{\min,U}$
SE-NR	1.0652	0.8287	1.3018	0.0030535	0.0064972	0.0014351
SE-NE	1.1089	0.8192	1.3987	0.0041237	0.0128904	0.0013192
SE-SV	0.9773	0.7175	1.2372	0.0027709	0.0058780	0.0013062
BB-S	1.0696	0.8325	1.3067	0.0075074	0.0160041	0.0035217
FI-S	1.2581	0.9291	1.5871	0.0003559	0.0012984	0.0000976
EE-NE	0.7870	0.5467	1.0272	0.0026042	0.0059551	0.0011388
FI-C	0.9190	0.7148	1.1231	0.0043001	0.0082514	0.0022410
SK	1.3162	0.7886	1.8438	0.0003548	0.0061174	0.0000206

Table B4: Recurrence parameters for the 2025 micro source zones estimated with MLE and catalogue completeness without SSZ groups.

SSZ	b	b_L	b_U	$n_{\min}$	$n_{\min,L}$	$n_{\min,U}$
SE-NR	1.0163	0.9444	1.0882	0.0022703	0.0038417	0.0013417
SE-NE	0.9884	0.9342	1.0426	0.0045827	0.0068693	0.0030573
SE-SV	0.9061	0.7672	1.0450	0.0023038	0.0051704	0.0010265
BB-S	1.0544	1.0025	1.1063	0.0044061	0.0066024	0.0029404
FI-S	1.2009	1.0606	1.3412	0.0002390	0.0006692	0.0000853
EE-NE	0.8401	0.6151	1.0650	0.0007100	0.0030423	0.0001657
FI-C	0.9884	0.8952	1.0816	0.0015225	0.0028226	0.0008213
SK	1.2468	1.0869	1.4068	0.0002453	0.0008678	0.0000693

Table B5: Recurrence parameters for the 2025 meso source zones estimated with the LS method.

SSZ	b	b_L	b_U	$n_{\min}$	$n_{\min,L}$	$n_{\min,U}$
SE	1.0320	0.8028	1.2613	0.0073241	0.0152242	0.0035235
SE-NE	1.1446	0.8454	1.4438	0.0037217	0.0120759	0.0011470
BB	1.1911	0.9265	1.4556	0.0058613	0.0136380	0.0025190
FI-EE	1.0426	0.8111	1.2742	0.0054746	0.0114652	0.0026141

Table B6: Recurrence parameters for the 2025 meso source zones estimated with the MLE method.

SSZ	b	b_L	b_U	$n_{\min}$	$n_{\min,L}$	$n_{\min,U}$
SE	0.9635	0.9166	1.0104	0.0056595	0.0079353	0.0040364
SE-NE	0.9885	0.9364	1.0405	0.0048794	0.0072131	0.0033007
BB	1.0813	1.0403	1.1224	0.0057082	0.0078470	0.0041523
FI-EE	1.1536	1.0939	1.2132	0.0013796	0.0020978	0.0009073

B.2 Recurrence Parameters for SSZ 10 Subdivisions

Tables B7–B10 summarise the recurrence parameters for the three proposed subdivisions of SSZ 10. Both LS and MLE estimates are shown, and the completeness intervals follow the grouped and non-grouped results provided by Vehmas [9].

Table B7: Recurrence parameters for the three subdivisions of SSZ 10 estimated with LS and catalogue completeness with SSZ groups.

Subdivision		b	b_L	b_U	$n_{\min}$	$n_{\min,L}$	$n_{\min,U}$
1	East	1.6815	1.0134	2.3496	0.0000040	0.0001485	0.0000001
	West	1.5255	0.9169	2.1341	0.0000535	0.0014279	0.0000020
2	East	1.6669	1.0046	2.3292	0.0000043	0.0001543	0.0000001
	West	1.5296	0.9195	2.1398	0.0000524	0.0014116	0.0000019
3	East	1.6782	0.7686	2.5878	0.0000030	0.0007848	0.0000000
	West	1.5059	0.9047	2.1071	0.0000641	0.0016430	0.0000025

Table B8: Recurrence parameters for the three subdivisions of SSZ 10 estimated with MLE and catalogue completeness with SSZ groups.

Subdivision		b	b_L	b_U	$n_{\min}$	$n_{\min,L}$	$n_{\min,U}$
1	East	1.7101	1.3550	2.0651	0.0000013	0.0000199	0.0000001
	West	1.4676	1.3167	1.6185	0.0000297	0.0000926	0.0000095
2	East	1.6852	1.3296	2.0408	0.0000015	0.0000230	0.0000001
	West	1.4744	1.3237	1.6251	0.0000286	0.0000891	0.0000092
3	East	1.8434	1.4002	2.2866	0.0000004	0.0000120	0.0000000
	West	1.4603	1.3138	1.6068	0.0000329	0.0000991	0.0000109

Table B9: Recurrence parameters for the three subdivisions of SSZ 10 estimated with LS and catalogue completeness without SSZ groups.

Subdivision		b	b_L	b_U	$n_{\min}$	$n_{\min,L}$	$n_{\min,U}$
1	East	0.9542	0.4282	1.4802	0.0009164	0.0228283	0.0000368
	West	1.2637	0.7602	1.7672	0.0003866	0.0058526	0.0000255
2	East	0.9322	0.4193	1.4452	0.0010357	0.0238238	0.0000450
	West	1.2677	0.7627	1.7726	0.0003794	0.0057888	0.0000249
3	East	0.8846	0.3796	1.3896	0.0012346	0.0270544	0.0000563
	West	1.2797	0.7698	1.7896	0.0003611	0.0056570	0.0000230

Table B10: Recurrence parameters for the three subdivisions of SSZ 10 estimated with MLE and catalogue completeness without SSZ groups.

Subdivision		b	b_L	b_U	$n_{\min}$	$n_{\min,L}$	$n_{\min,U}$
1	East	1.3993	0.9967	1.8018	0.0000169	0.0004164	0.0000007
	West	1.2107	1.0364	1.3850	0.0002509	0.0009905	0.0000635
2	East	1.3751	0.9744	1.7757	0.0000195	0.0004714	0.0000008
	West	1.2173	1.0428	1.3917	0.0002418	0.0009564	0.0000611
3	East	1.3890	0.9595	1.8185	0.0000157	0.0004789	0.0000005
	West	1.2185	1.0462	1.3909	0.0002460	0.0009573	0.0000632

C Additional Catalogue Completeness Results

This appendix provides supplementary completeness results that support and expand on the findings presented in Section 5.1. Table C1 lists the completeness intervals for the micro-level SSZs, obtained by linking each micro SSZ to the corresponding 2016 SSZ completeness intervals without SSZ groups as reported by Vehmas [9]. The numbers of earthquakes retained in FENCAT21 in each SSZ and magnitude bin after applying the completeness intervals for the different SSZ models are provided in Tables C2–C4. Figures C1–C3 illustrate the CUVI-based completeness evaluations for the meso-level zones SE, BB, and FI–EE, which are listed in Table 8.

Table C1: Start years of completeness intervals by magnitude bin, derived by linking the micro SSZ zones to the corresponding 2016 SSZ completeness intervals presented by Vehmas [9]. Each completeness interval begins on the first day of the listed year and ends on 31 December 2021. In this table, the completeness intervals are shown without applying any SSZ grouping.

		Magnitude Bin					
SSZ (2016)	**SSZ (micro)**	**1.0–1.5**	**1.5–2.0**	**2.0–2.5**	**2.5–3.0**	**3.0–3.5**	**3.5–**
1	SE-NR	2007	1992	1962	1922	1742	1742
2	SE-NE	2002	1992	1992	1952	1882	1882
3	-	–	2002	1962	1882	1882	1882
4	SE-SV	–	2002	1962	1762	1742	1742
5	BB-S	1997	1997	1962	1942	1882	1882
6	FI-S, EE-NE	2012	2012	2012	1782	1782	1782
8	FI-C	2012	2012	1882	1722	1722	1722
10	SK	2007	2007	2002	1932	1932	1932

Table C2: Number of earthquakes per magnitude bin and SSZ in the 2016 and 2025 micro models, after applying the completeness intervals defined in Table C1 to FENCAT21.

	Magnitude Bin						
SSZ	**1.0–1.5**	**1.5–2.0**	**2.0–2.5**	**2.5–3.0**	**3.0–3.5**	**3.5–4.0**	**4.0–4.5**
1	29	25	20	13	9	2	1
2	122	64	23	11	8	3	0
3	0	41	44	21	6	2	0
4	0	20	14	25	10	3	0
5	365	141	61	33	19	4	1
6 (whole)	30	14	4	13	6	1	1
6a	14	1	2	4	0	0	0
6b	10	5	0	4	1	1	0
6c	6	8	2	5	5	0	1
8	33	23	36	19	11	5	1
10	62	17	8	5	0	0	0
All (2016)	**641**	**345**	**210**	**140**	**69**	**20**	**4**
SE-NR	73	63	39	16	13	2	2
SE-NE	154	106	48	23	14	5	0
SE-SV	0	17	14	24	12	4	1
BB-S	367	141	61	34	19	4	2
FI-S	26	10	2	12	1	1	0
EE-NE	3	4	1	0	5	0	1
FI-C	32	22	40	21	12	6	2
SK	62	17	8	5	0	0	0
All (micro)	**717**	**380**	**213**	**135**	**76**	**22**	**8**

Table C3: Number of earthquakes per magnitude bin and SSZ in the 2016 and 2025 micro models, after applying the completeness intervals defined in Table 7 to FENCAT21.

	Magnitude Bin						
SSZ	**1.0–1.5**	**1.5–2.0**	**2.0–2.5**	**2.5–3.0**	**3.0–3.5**	**3.5–4.0**	**4.0–4.5**
1	29	25	20	19	9	2	1
2	122	64	30	16	8	4	0
3	0	41	44	21	6	2	0
4	0	20	14	25	10	3	0
5	365	141	61	33	19	5	1
6 (whole)	30	14	9	13	6	1	1
6a	14	1	2	4	0	0	0
6b	10	5	4	4	1	1	0
6c	6	8	3	5	5	0	1
8	33	23	36	18	11	4	1
10	62	17	17	8	0	0	0
All (2016)	**641**	**345**	**231**	**153**	**69**	**21**	**4**
SE-NR	73	63	39	22	13	2	2
SE-NE	154	106	74	34	14	6	0
SE-SV	0	17	14	24	12	4	1
BB-S	367	141	61	34	19	5	2
FI-S	26	10	5	12	1	1	0
EE-NE	3	4	3	0	5	0	1
FI-C	32	22	40	20	12	5	2
SK	62	17	17	8	0	0	0
All (micro)	**717**	**380**	**253**	**154**	**76**	**23**	**8**

Table C4: Number of earthquakes per magnitude bin and SSZ in the 2025 meso model, after applying the completeness intervals defined in Table 8 to FENCAT21.

	Magnitude Bin						
SSZ	**1.0–1.5**	**1.5–2.0**	**2.0–2.5**	**2.5–3.0**	**3.0–3.5**	**3.5–4.0**	**4.0–4.5**
SE	140	104	82	53	27	8	4
SE-NE	162	102	73	34	14	6	0
BB	490	190	99	42	28	7	3
FI-EE	136	62	78	47	20	8	3
All (meso)	**928**	**458**	**332**	**176**	**89**	**29**	**10**

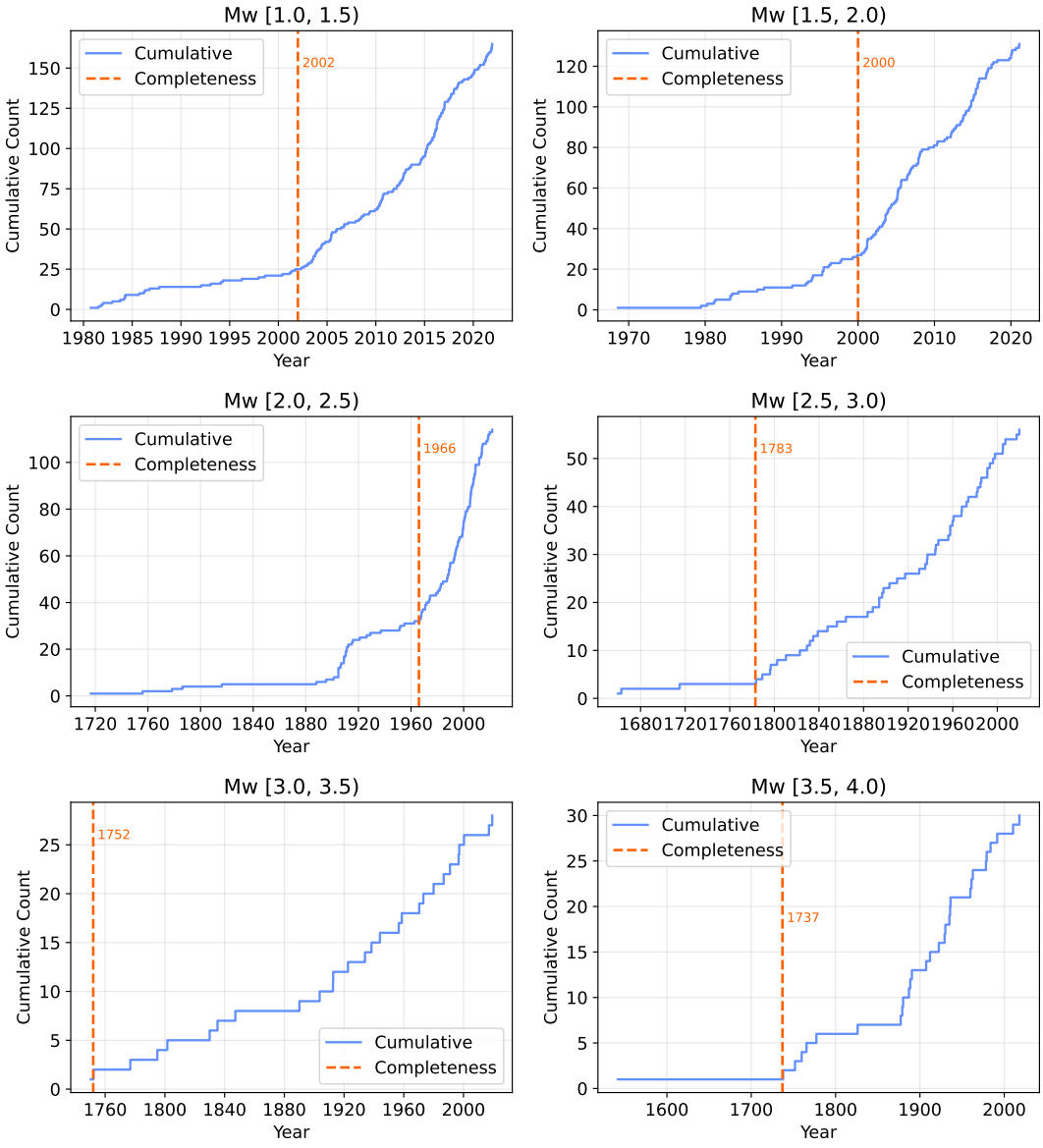

Figure C1: Start years of the completeness intervals by magnitude bin, estimated with the CUVI method for the meso-level SE zone.

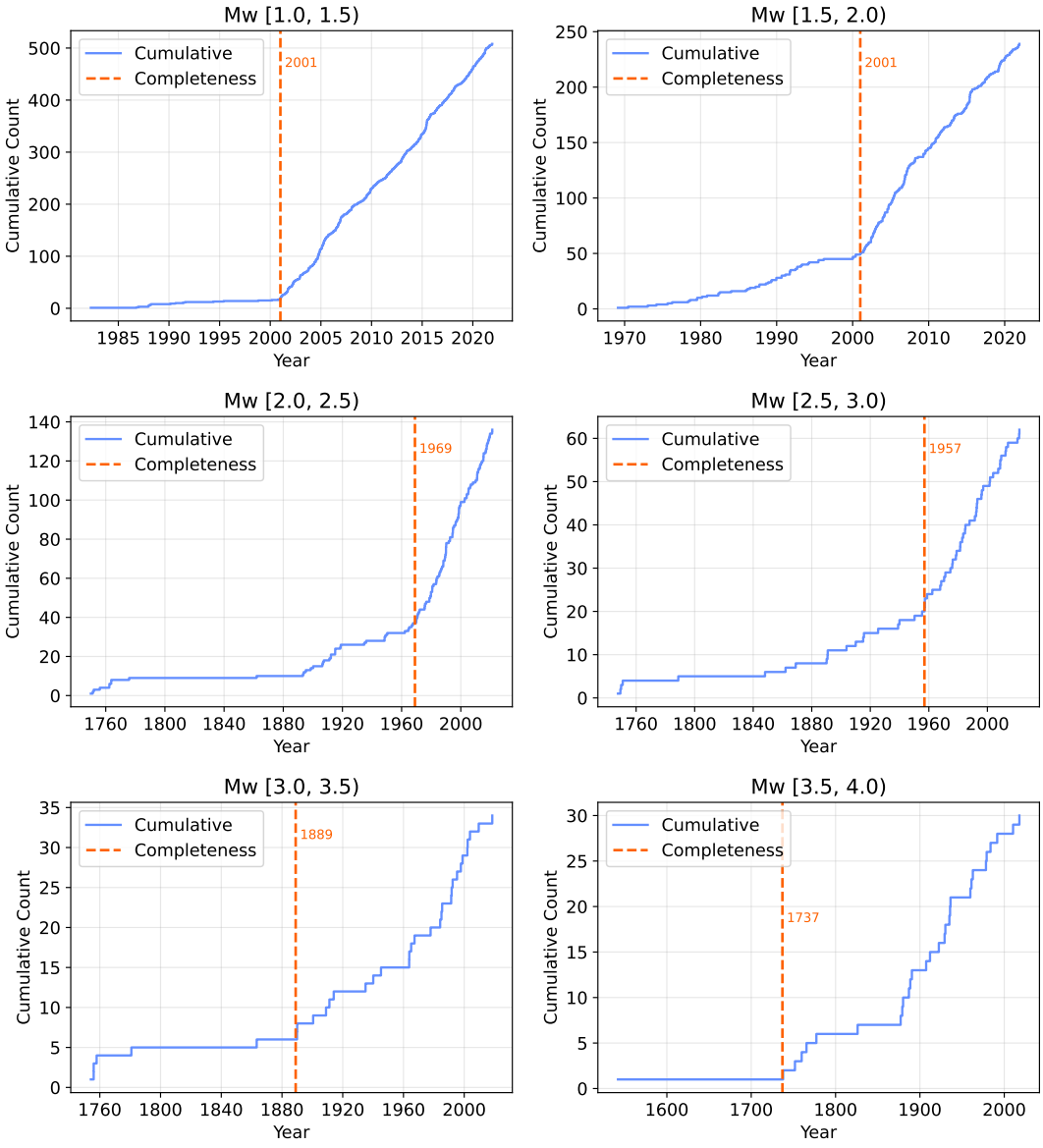

Figure C2: Start years of the completeness intervals by magnitude bin, estimated with the CUVI method for the meso-level BB zone.

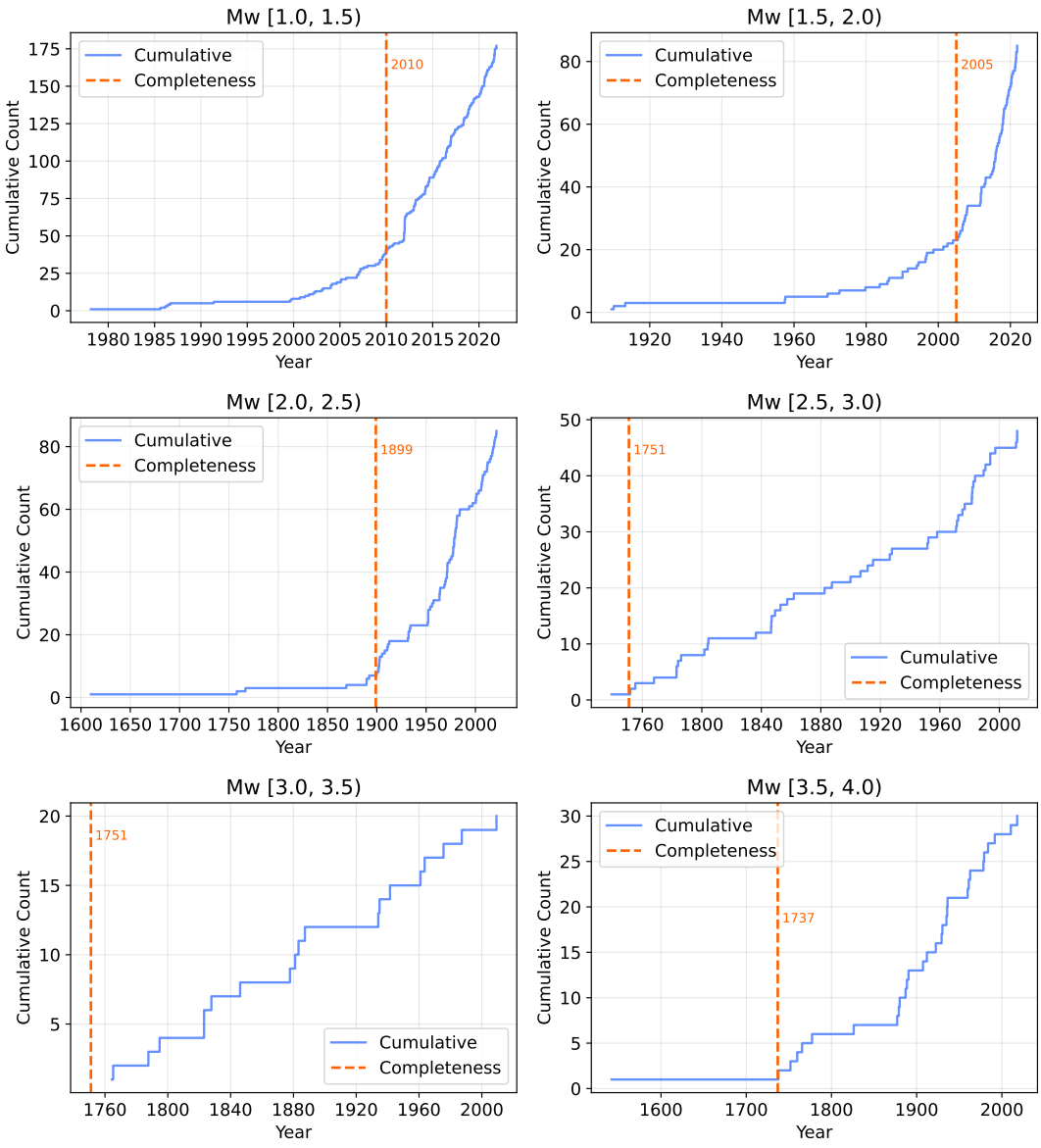

Figure C3: Start years of the completeness intervals by magnitude bin, estimated with the CUVI method for the meso-level FI-EE zone.

D Additional Seismic Hazard Estimate Results

This appendix presents complementary seismic hazard estimate results for the modelling alternatives investigated in this thesis. The contents are organised separately for Loviisa and Olkiluoto, followed by the results obtained using the suggested adaptation presented in Chapter 6 for both sites. All fractile values presented in this appendix were computed using an open-source post-processing tool [93] developed for the HAZ program [90].

D.1 Loviisa Hazard Estimate Sensitivity

Figure D1 presents the mean hazard curves at 100 Hz for all investigated alternatives: the 2025 micro and meso SSZ models, the three SSZ 10 subdivisions, and the updated maximum magnitude model. The tabulated UHRS for the micro and meso models are provided in Tables D1 and D2, respectively, with the corresponding hazard curves presented in Figures D2 and D3. The UHRS values for the three SSZ 10 subdivision alternatives are presented in Tables D3–D5, while their associated hazard curves appear in Figures D4–D6. Finally, the UHRS values and hazard curves obtained using the updated maximum magnitude distribution are given in Table D6 and Figure D7, respectively.

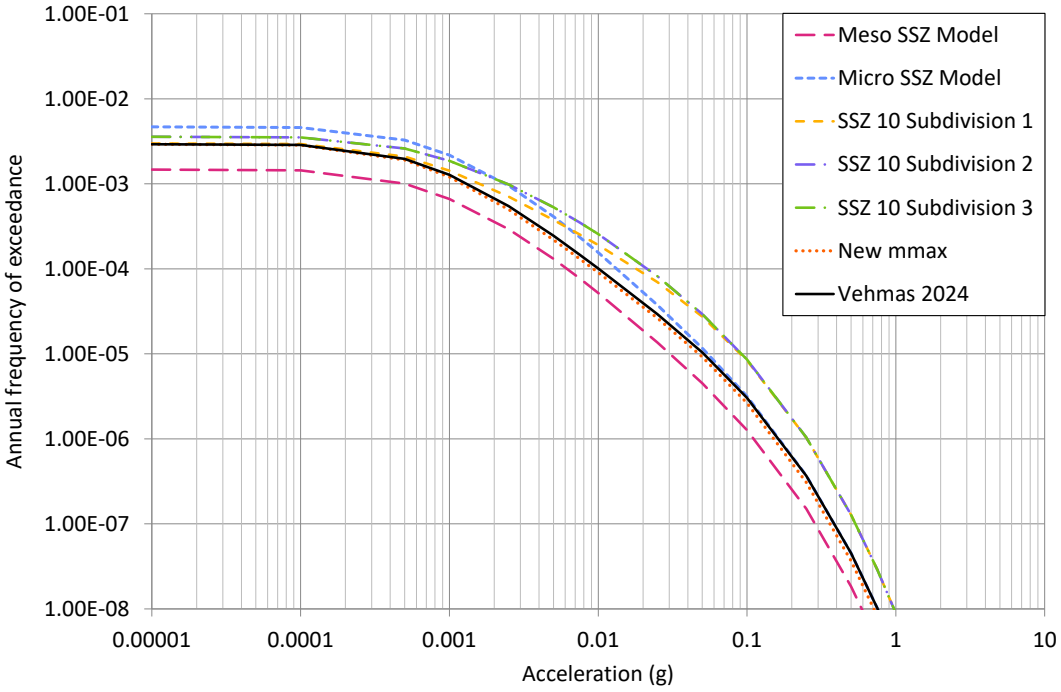

Figure D1: Loviisa mean hazard curve at 100 Hz for the different modelling decisions. The result of Vehmas [86] is included for comparison.

Table D1: Loviisa mean UHRS values using the micro model.

Frequency (Hz)	SA at mean AFE 10^{-3} (g)	SA at mean AFE 10^{-4} (g)	SA at mean AFE 10^{-5} (g)	SA at mean AFE 10^{-6} (g)	SA at mean AFE 10^{-7} (g)	SA at mean AFE 10^{-8} (g)
0.10	0.00000	0.00006	0.00025	0.00075	0.00178	0.00379
0.13	0.00002	0.00012	0.00046	0.00130	0.00312	0.00662
0.20	0.00004	0.00028	0.00104	0.00283	0.00655	0.01351
0.25	0.00007	0.00048	0.00161	0.00437	0.01008	0.02081
0.33	0.00013	0.00081	0.00276	0.00748	0.01719	0.03655
0.40	0.00018	0.00119	0.00397	0.01061	0.02473	0.05202
0.50	0.00031	0.00189	0.00629	0.01626	0.03788	0.07916
0.67	0.00057	0.00316	0.01017	0.02647	0.06130	0.12650
1.00	0.00123	0.00639	0.01933	0.05042	0.11559	0.23921
1.33	0.00198	0.00988	0.02952	0.07623	0.17444	0.35519
2.00	0.00352	0.01586	0.04808	0.12379	0.28581	0.56996
2.50	0.00447	0.01962	0.05941	0.15485	0.35715	0.71410
3.33	0.00575	0.02523	0.07578	0.20129	0.46364	0.90689
4.00	0.00635	0.02786	0.08586	0.23378	0.53776	1.04609
5.00	0.00734	0.03216	0.10207	0.27977	0.64137	1.22543
10.00	0.00856	0.04158	0.14545	0.42570	0.98969	1.90155
13.30	0.00833	0.04275	0.15690	0.47618	1.10301	2.15969
25.00	0.00591	0.03357	0.13406	0.41291	0.97008	1.86536
33.30	0.00443	0.02563	0.10544	0.32381	0.76482	1.44555
50.00	0.00296	0.01713	0.07146	0.22255	0.52255	1.00842
100.00	0.00236	0.01327	0.05439	0.16369	0.38484	0.75468

Table D2: Loviisa mean UHRS values using the meso model.

Frequency (Hz)	SA at mean AFE 10^{-3} (g)	SA at mean AFE 10^{-4} (g)	SA at mean AFE 10^{-5} (g)	SA at mean AFE 10^{-6} (g)	SA at mean AFE 10^{-7} (g)	SA at mean AFE 10^{-8} (g)
0.10	0.00000	0.00002	0.00012	0.00040	0.00113	0.00264
0.13	0.00000	0.00004	0.00020	0.00072	0.00197	0.00463
0.20	0.00000	0.00011	0.00051	0.00160	0.00427	0.00977
0.25	0.00001	0.00017	0.00080	0.00256	0.00665	0.01481
0.33	0.00002	0.00029	0.00137	0.00438	0.01148	0.02648
0.40	0.00002	0.00046	0.00201	0.00634	0.01629	0.03734
0.50	0.00004	0.00076	0.00324	0.01001	0.02578	0.05785
0.67	0.00011	0.00129	0.00541	0.01614	0.04200	0.09493
1.00	0.00020	0.00278	0.01080	0.03177	0.08097	0.17530
1.33	0.00039	0.00443	0.01652	0.04934	0.12355	0.27129
2.00	0.00079	0.00773	0.02793	0.08180	0.20425	0.43492
2.50	0.00105	0.00968	0.03475	0.10375	0.26143	0.54944
3.33	0.00129	0.01222	0.04488	0.13318	0.33443	0.70387
4.00	0.00141	0.01354	0.05085	0.15311	0.38814	0.81577
5.00	0.00162	0.01572	0.06014	0.18530	0.47160	0.97372
10.00	0.00181	0.02004	0.08524	0.28494	0.73013	1.47144
13.30	0.00169	0.02029	0.09099	0.31363	0.81839	1.67564
25.00	0.00118	0.01544	0.07650	0.27688	0.71721	1.44927
33.30	0.00092	0.01178	0.05899	0.21660	0.56390	1.14739
50.00	0.00061	0.00795	0.04004	0.14534	0.38063	0.79392
100.00	0.00051	0.00615	0.03037	0.11078	0.28603	0.59028

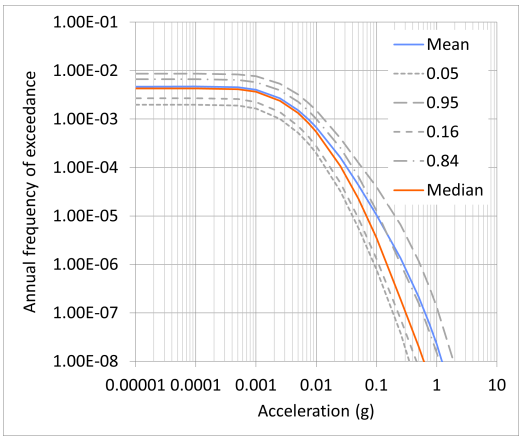

(a) 5 Hz

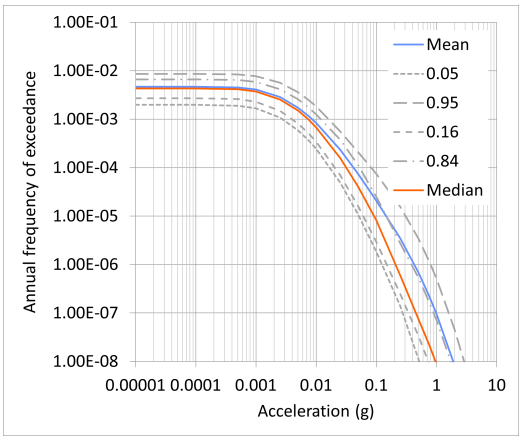

(b) 10 Hz

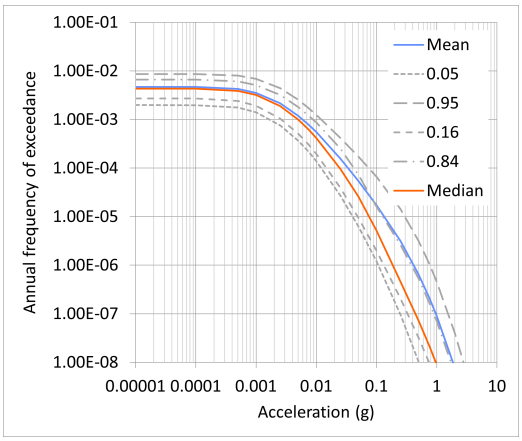

(c) 25 Hz

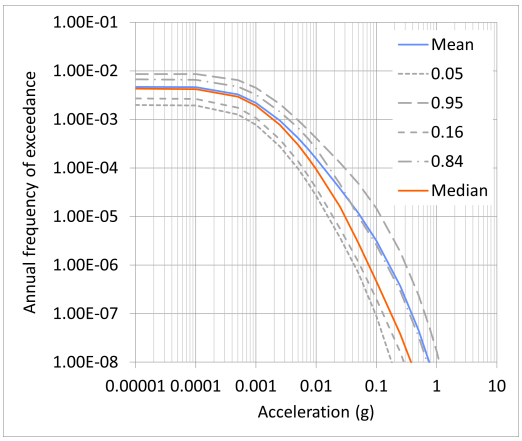

(d) 100 Hz

Figure D2: Loviisa mean, median, and 0.05, 0.16, 0.84, and 0.95 fractile hazard curves at different frequencies for the micro model.

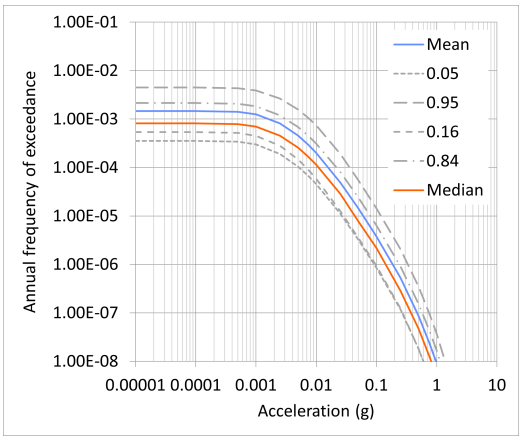

(a) 5 Hz

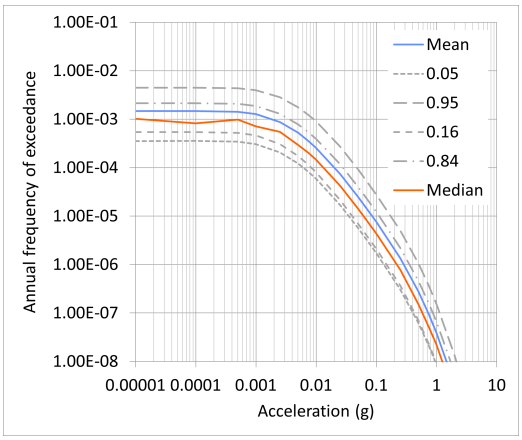

(b) 10 Hz

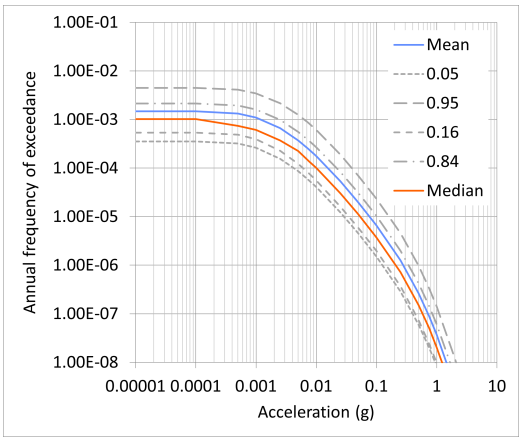

(c) 25 Hz

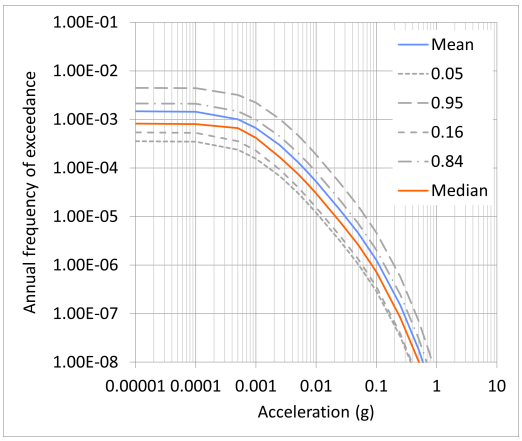

(d) 100 Hz

Figure D3: Loviisa mean, median, and 0.05, 0.16, 0.84, and 0.95 fractile hazard curves at different frequencies for the meso model.

Table D3: Loviisa mean UHRS values using the SSZ 10 Subdivision 1.

Frequency (Hz)	SA at mean AFE 10^{-3} (g)	SA at mean AFE 10^{-4} (g)	SA at mean AFE 10^{-5} (g)	SA at mean AFE 10^{-6} (g)	SA at mean AFE 10^{-7} (g)	SA at mean AFE 10^{-8} (g)
0.10	0.00000	0.00006	0.00028	0.00091	0.00230	0.00508
0.13	0.00001	0.00012	0.00053	0.00160	0.00405	0.00890
0.20	0.00003	0.00029	0.00121	0.00355	0.00870	0.01803
0.25	0.00005	0.00051	0.00192	0.00562	0.01325	0.02800
0.33	0.00011	0.00088	0.00337	0.00989	0.02380	0.05008
0.40	0.00016	0.00128	0.00496	0.01396	0.03361	0.06935
0.50	0.00026	0.00209	0.00789	0.02215	0.05259	0.10686
0.67	0.00049	0.00354	0.01294	0.03649	0.08558	0.16864
1.00	0.00109	0.00742	0.02612	0.07098	0.15910	0.31433
1.33	0.00175	0.01152	0.04038	0.10983	0.24897	0.47630
2.00	0.00321	0.01951	0.06775	0.17891	0.39416	0.75123
2.50	0.00409	0.02501	0.08607	0.22979	0.50237	0.93292
3.33	0.00540	0.03203	0.11195	0.29607	0.63826	1.16406
4.00	0.00601	0.03622	0.12771	0.34130	0.74274	1.33724
5.00	0.00702	0.04331	0.15327	0.41156	0.88204	1.58456
10.00	0.00855	0.06068	0.23704	0.63710	1.33008	2.45045
13.30	0.00843	0.06401	0.26104	0.71510	1.50360	2.79964
25.00	0.00616	0.05387	0.22722	0.62331	1.30550	2.40676
33.30	0.00466	0.04132	0.17505	0.49448	1.04256	1.89047
50.00	0.00309	0.02809	0.12038	0.33207	0.71539	1.27404
100.00	0.00244	0.02131	0.09180	0.25326	0.53463	0.97137

Table D4: Loviisa mean UHRS values using the SSZ 10 Subdivision 2.

Frequency (Hz)	SA at mean AFE 10^{-3} (g)	SA at mean AFE 10^{-4} (g)	SA at mean AFE 10^{-5} (g)	SA at mean AFE 10^{-6} (g)	SA at mean AFE 10^{-7} (g)	SA at mean AFE 10^{-8} (g)
0.10	0.00000	0.00006	0.00027	0.00087	0.00216	0.00476
0.13	0.00001	0.00012	0.00051	0.00152	0.00381	0.00835
0.20	0.00003	0.00028	0.00116	0.00336	0.00816	0.01692
0.25	0.00005	0.00050	0.00183	0.00530	0.01246	0.02642
0.33	0.00011	0.00085	0.00320	0.00925	0.02210	0.04676
0.40	0.00016	0.00125	0.00469	0.01309	0.03141	0.06520
0.50	0.00025	0.00202	0.00748	0.02059	0.04920	0.10120
0.67	0.00049	0.00342	0.01221	0.03390	0.07954	0.15861
1.00	0.00108	0.00712	0.02443	0.06574	0.14850	0.29725
1.33	0.00174	0.01107	0.03748	0.10218	0.23047	0.44764
2.00	0.00319	0.01850	0.06262	0.16495	0.36802	0.70891
2.50	0.00407	0.02355	0.07893	0.21051	0.46732	0.88287
3.33	0.00537	0.03025	0.10323	0.27443	0.59780	1.10813
4.00	0.00597	0.03403	0.11723	0.31519	0.69351	1.26985
5.00	0.00697	0.04037	0.13993	0.37851	0.82725	1.50106
10.00	0.00850	0.05596	0.21188	0.58703	1.24986	2.32723
13.30	0.00837	0.05862	0.23392	0.65616	1.40805	2.65052
25.00	0.00611	0.04864	0.20160	0.57434	1.22714	2.28634
33.30	0.00462	0.03700	0.15635	0.45151	0.98249	1.78636
50.00	0.00306	0.02531	0.10874	0.30656	0.66943	1.21275
100.00	0.00242	0.01908	0.08159	0.23120	0.50339	0.92103

Table D5: Loviisa mean UHRS values using the SSZ 10 Subdivision 3.

Frequency (Hz)	SA at mean AFE 10^{-3} (g)	SA at mean AFE 10^{-4} (g)	SA at mean AFE 10^{-5} (g)	SA at mean AFE 10^{-6} (g)	SA at mean AFE 10^{-7} (g)	SA at mean AFE 10^{-8} (g)
0.10	0.00000	0.00006	0.00027	0.00087	0.00212	0.00459
0.13	0.00001	0.00013	0.00052	0.00151	0.00372	0.00804
0.20	0.00003	0.00030	0.00117	0.00332	0.00793	0.01630
0.25	0.00006	0.00051	0.00185	0.00522	0.01210	0.02549
0.33	0.00012	0.00088	0.00321	0.00905	0.02125	0.04480
0.40	0.00017	0.00129	0.00469	0.01279	0.03026	0.06271
0.50	0.00027	0.00209	0.00746	0.02000	0.04713	0.09717
0.67	0.00053	0.00352	0.01211	0.03276	0.07614	0.15250
1.00	0.00115	0.00729	0.02397	0.06315	0.14231	0.28661
1.33	0.00186	0.01125	0.03660	0.09771	0.21951	0.42982
2.00	0.00339	0.01869	0.06067	0.15730	0.35212	0.68235
2.50	0.00435	0.02374	0.07600	0.19976	0.44577	0.85154
3.33	0.00570	0.03031	0.09907	0.26168	0.57291	1.07307
4.00	0.00636	0.03400	0.11232	0.29985	0.66331	1.22780
5.00	0.00747	0.04017	0.13352	0.35908	0.79357	1.44907
10.00	0.00913	0.05508	0.19902	0.55707	1.20046	2.25056
13.30	0.00902	0.05746	0.21841	0.62097	1.34959	2.55817
25.00	0.00662	0.04699	0.18784	0.54492	1.17914	2.21186
33.30	0.00504	0.03573	0.14603	0.42594	0.94078	1.72210
50.00	0.00330	0.02438	0.10211	0.29116	0.64130	1.17466
100.00	0.00261	0.01845	0.07603	0.21756	0.48106	0.88981

Table D6: Loviisa mean UHRS values using the updated maximum magnitude.

Frequency (Hz)	SA at mean AFE 10^{-3} (g)	SA at mean AFE 10^{-4} (g)	SA at mean AFE 10^{-5} (g)	SA at mean AFE 10^{-6} (g)	SA at mean AFE 10^{-7} (g)	SA at mean AFE 10^{-8} (g)
0.10	0.00000	0.00003	0.000132333	0.00042	0.00115	0.002692474
0.13	0.00000	0.00005	0.00023476	0.00077	0.00206	0.004774232
0.20	0.00002	0.00014	0.000586238	0.00175	0.00456	0.010230174
0.25	0.00003	0.00023	0.000945975	0.00279	0.00719	0.015629968
0.33	0.00005	0.00041	0.001607536	0.00491	0.01256	0.028342006
0.40	0.00008	0.00062	0.002404492	0.00716	0.01813	0.040484475
0.50	0.00014	0.00102	0.00384268	0.01133	0.02889	0.063083194
0.67	0.00023	0.00172	0.00648498	0.01894	0.04872	0.105215329
1.00	0.00060	0.00367	0.013101372	0.03833	0.09621	0.199182717
1.33	0.00102	0.00591	0.020690359	0.06051	0.14649	0.307456336
2.00	0.00180	0.01029	0.035618354	0.10444	0.25204	0.508061969
2.50	0.00239	0.01278	0.045434026	0.13169	0.31608	0.638100117
3.33	0.00307	0.01647	0.05951865	0.17355	0.41314	0.823860783
4.00	0.00340	0.01849	0.068206345	0.20344	0.48682	0.959534718
5.00	0.00393	0.02186	0.082721784	0.25198	0.58548	1.135474989
10.00	0.00460	0.02894	0.123180178	0.38786	0.91914	1.77414705
13.30	0.00441	0.02981	0.133867973	0.43639	1.03870	2.043566652
25.00	0.00306	0.02362	0.117621531	0.38363	0.91476	1.766720555
33.30	0.00231	0.01785	0.093006207	0.30305	0.72193	1.376470037
50.00	0.00150	0.01199	0.062552866	0.20540	0.49296	0.956854705
100.00	0.00121	0.00922	0.047361643	0.15095	0.35991	0.710353722

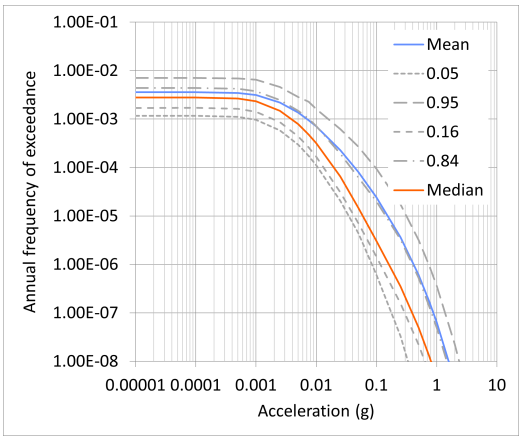

(a) 5 Hz

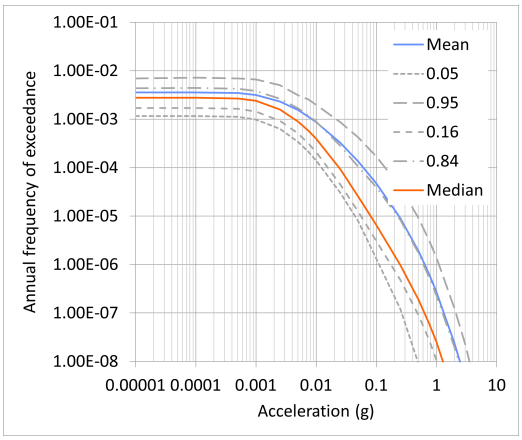

(b) 10 Hz

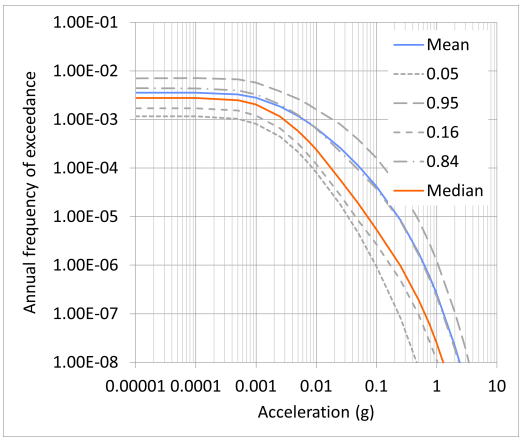

(c) 25 Hz

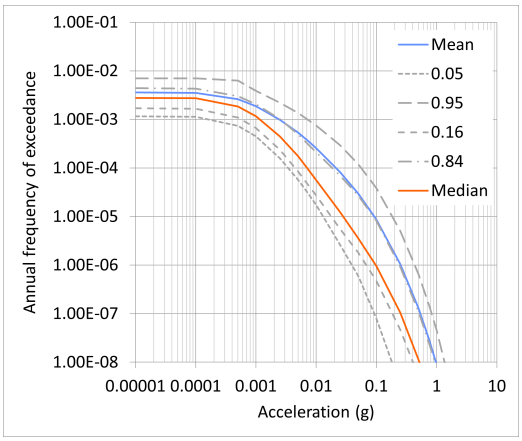

(d) 100 Hz

Figure D4: Loviisa mean, median, and 0.05, 0.16, 0.84, and 0.95 fractile hazard curves at different frequencies using the SSZ 10 Subdivision 1.

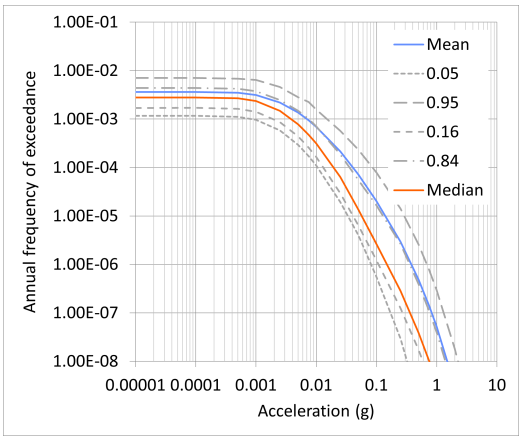

(a) 5 Hz

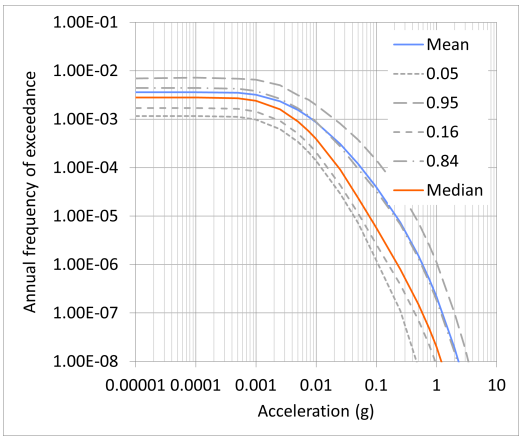

(b) 10 Hz

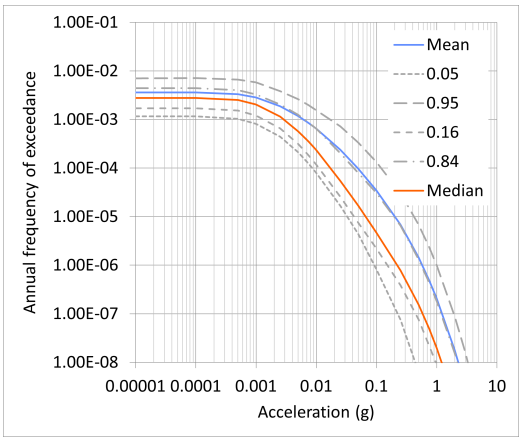

(c) 25 Hz

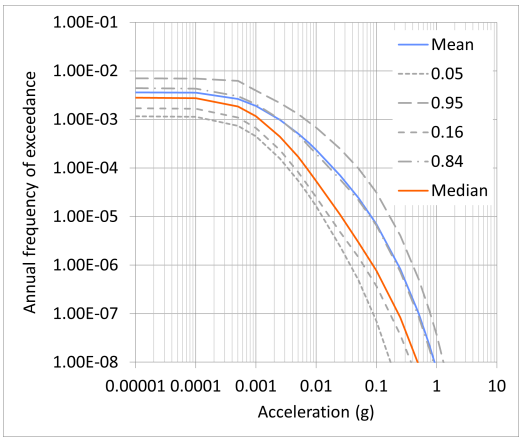

(d) 100 Hz

Figure D5: Loviisa mean, median, and 0.05, 0.16, 0.84, and 0.95 fractile hazard curves at different frequencies using the SSZ 10 Subdivision 2.

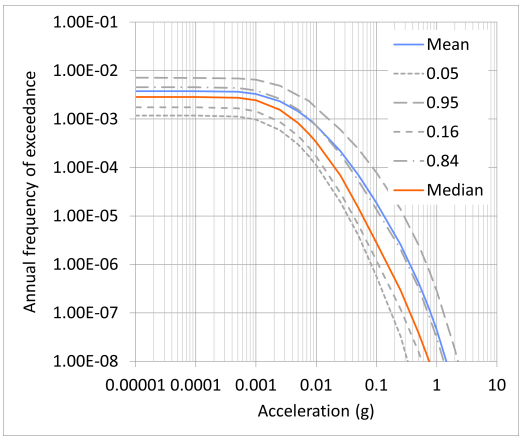

(a) 5 Hz

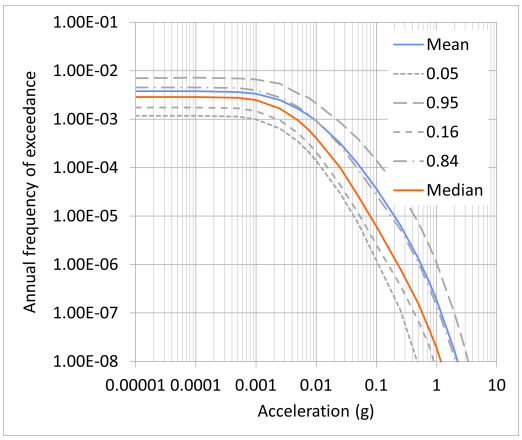

(b) 10 Hz

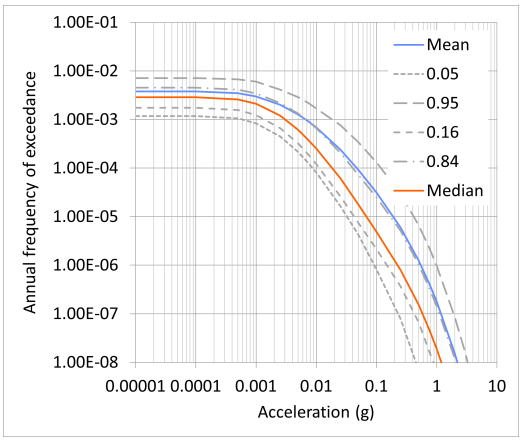

(c) 25 Hz

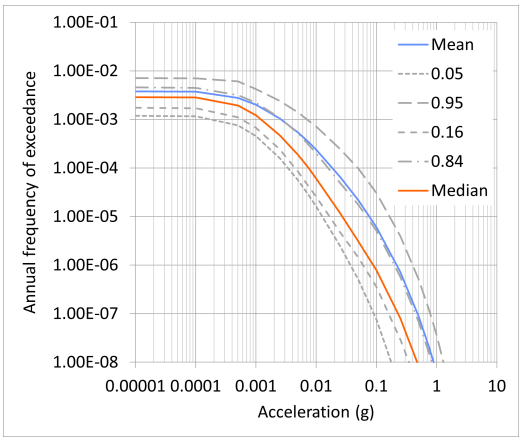

(d) 100 Hz

Figure D6: Loviisa mean, median, and 0.05, 0.16, 0.84, and 0.95 fractile hazard curves at different frequencies using the SSZ 10 Subdivision 3.

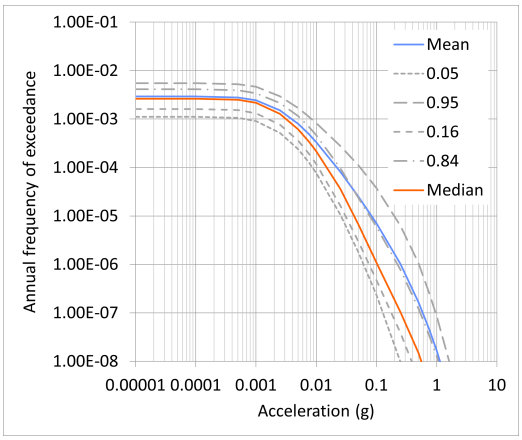

(a) 5 Hz

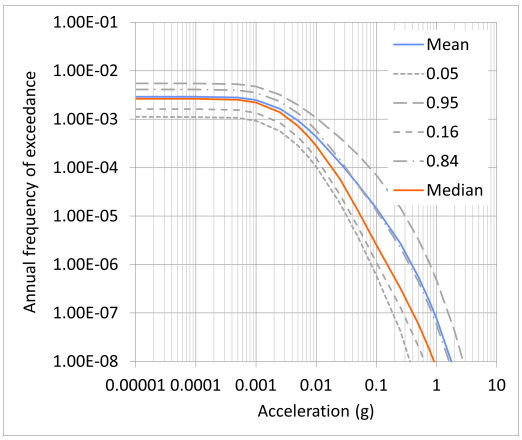

(b) 10 Hz

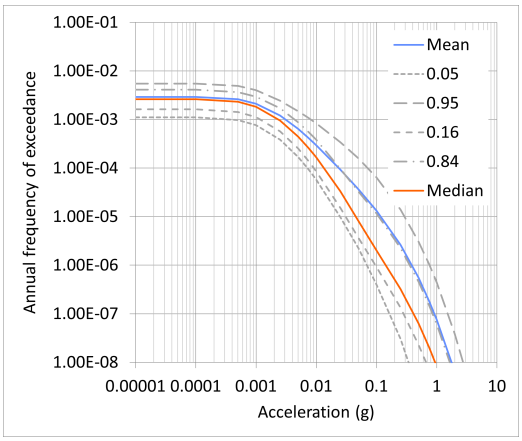

(c) 25 Hz

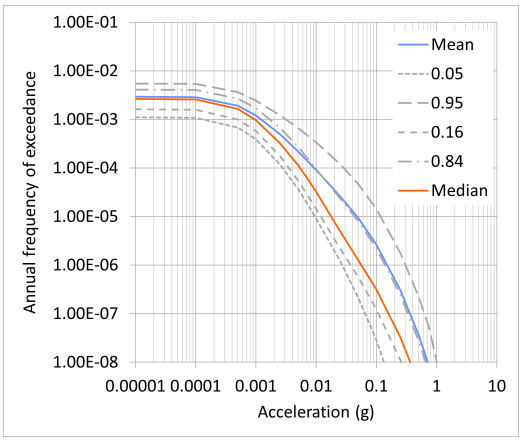

(d) 100 Hz

Figure D7: Loviisa mean, median, and 0.05, 0.16, 0.84, and 0.95 fractile hazard curves at different frequencies using the updated maximum magnitude.

D.2 Olkiluoto Hazard Estimate Sensitivity

Figure D8 presents the mean hazard curves at 100 Hz for Olkiluoto obtained with the 2025 SSZ models and the updated maximum magnitude. Tables D7 and D8 list the tabulated UHRS values for the micro and meso models, respectively, with the corresponding mean hazard curves given in Figures D9 and D10. The UHRS values and hazard curves obtained using the updated maximum magnitude distribution are presented in Table D9 and Figure D11, respectively.

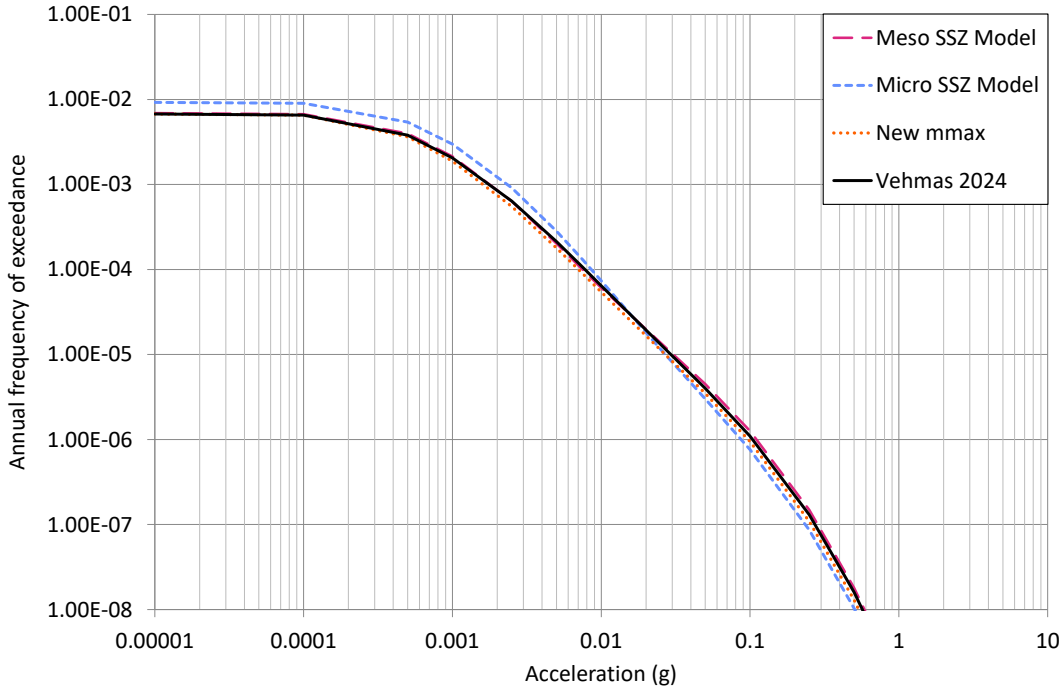

Figure D8: Olkiluoto mean hazard curve at 100 Hz for the different modelling decisions. The result of Vehmas [86] is included for comparison.

Table D7: Olkiluoto mean UHRS values using the micro model.

Frequency (Hz)	SA at mean AFE 10^{-3} (g)	SA at mean AFE 10^{-4} (g)	SA at mean AFE 10^{-5} (g)	SA at mean AFE 10^{-6} (g)	SA at mean AFE 10^{-7} (g)	SA at mean AFE 10^{-8} (g)
0.10	0.00001	0.00007	0.00024	0.00068	0.00146	0.00279
0.13	0.00002	0.00013	0.00044	0.00116	0.00253	0.00470
0.20	0.00006	0.00029	0.00097	0.00243	0.00506	0.00941
0.25	0.00010	0.00049	0.00147	0.00362	0.00757	0.01415
0.33	0.00016	0.00082	0.00248	0.00597	0.01232	0.02386
0.40	0.00024	0.00119	0.00350	0.00837	0.01704	0.03344
0.50	0.00042	0.00188	0.00548	0.01254	0.02607	0.05083
0.67	0.00073	0.00307	0.00854	0.01911	0.03989	0.08022
1.00	0.00152	0.00602	0.01538	0.03446	0.07224	0.14704
1.33	0.00250	0.00910	0.02284	0.05042	0.10716	0.22466
2.00	0.00420	0.01407	0.03506	0.07786	0.17104	0.35962
2.50	0.00525	0.01689	0.04202	0.09469	0.21484	0.45666
3.33	0.00654	0.02084	0.05159	0.11883	0.27628	0.58783
4.00	0.00716	0.02279	0.05647	0.13392	0.31756	0.68322
5.00	0.00805	0.02575	0.06426	0.15795	0.38189	0.81901
10.00	0.00879	0.02951	0.08201	0.23041	0.59418	1.25008
13.30	0.00838	0.02923	0.08517	0.25219	0.66698	1.41411
25.00	0.00569	0.02111	0.06800	0.21756	0.58578	1.23793
33.30	0.00423	0.01583	0.05155	0.16798	0.46158	0.99180
50.00	0.00286	0.01074	0.03499	0.11493	0.31194	0.67431
100.00	0.00233	0.00857	0.02698	0.08710	0.23508	0.50496

Table D8: Olkiluoto mean UHRS values using the meso model.

Frequency (Hz)	SA at mean AFE 10^{-3} (g)	SA at mean AFE 10^{-4} (g)	SA at mean AFE 10^{-5} (g)	SA at mean AFE 10^{-6} (g)	SA at mean AFE 10^{-7} (g)	SA at mean AFE 10^{-8} (g)
0.10	0.00000	0.00005	0.00020	0.00060	0.00138	0.00284
0.13	0.00002	0.00010	0.00036	0.00104	0.00239	0.00489
0.20	0.00004	0.00023	0.00082	0.00217	0.00490	0.01007
0.25	0.00007	0.00038	0.00127	0.00331	0.00746	0.01531
0.33	0.00012	0.00065	0.00211	0.00553	0.01251	0.02678
0.40	0.00018	0.00097	0.00304	0.00783	0.01761	0.03780
0.50	0.00030	0.00152	0.00478	0.01194	0.02723	0.05820
0.67	0.00055	0.00255	0.00757	0.01865	0.04347	0.09493
1.00	0.00117	0.00505	0.01403	0.03486	0.08215	0.17504
1.33	0.00186	0.00768	0.02093	0.05235	0.12424	0.27027
2.00	0.00327	0.01219	0.03317	0.08459	0.20432	0.43277
2.50	0.00407	0.01463	0.04024	0.10541	0.26070	0.54675
3.33	0.00520	0.01800	0.05004	0.13473	0.33323	0.69999
4.00	0.00566	0.01965	0.05556	0.15436	0.38654	0.81133
5.00	0.00636	0.02225	0.06448	0.18596	0.46945	0.96807
10.00	0.00694	0.02586	0.08716	0.28418	0.72668	1.46258
13.30	0.00656	0.02554	0.09221	0.31267	0.81477	1.66496
25.00	0.00440	0.01855	0.07686	0.27602	0.71366	1.44020
33.30	0.00328	0.01400	0.05911	0.21579	0.56120	1.14051
50.00	0.00221	0.00937	0.04019	0.14486	0.37867	0.78888
100.00	0.00177	0.00748	0.03055	0.11045	0.28477	0.58666

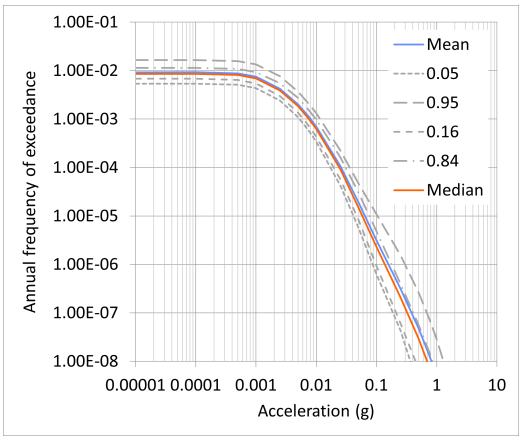

(a) 5 Hz

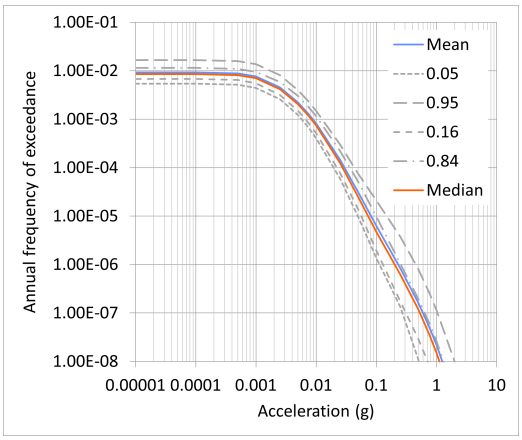

(b) 10 Hz

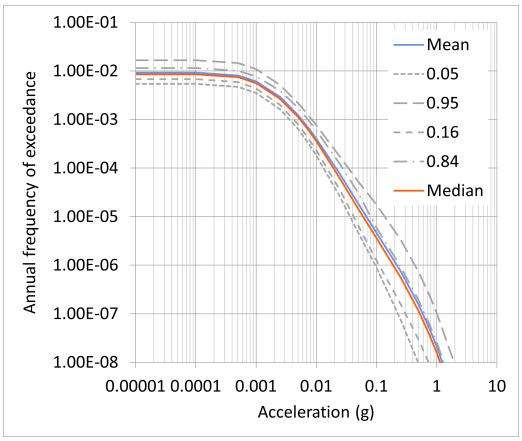

(c) 25 Hz

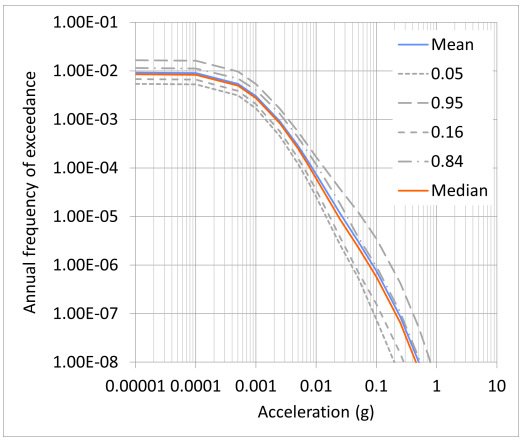

(d) 100 Hz

Figure D9: Olkiluoto mean, median, and 0.05, 0.16, 0.84, and 0.95 fractile hazard curves at different frequencies for the micro model.

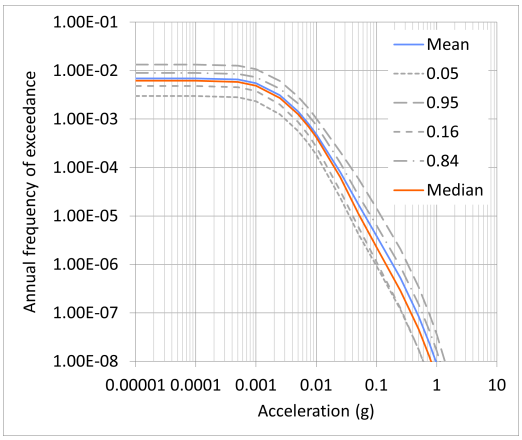

(a) 5 Hz

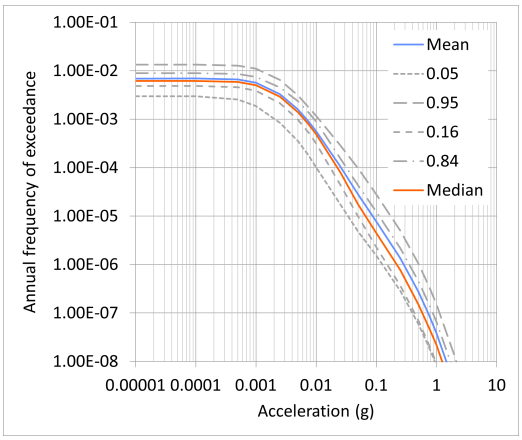

(b) 10 Hz

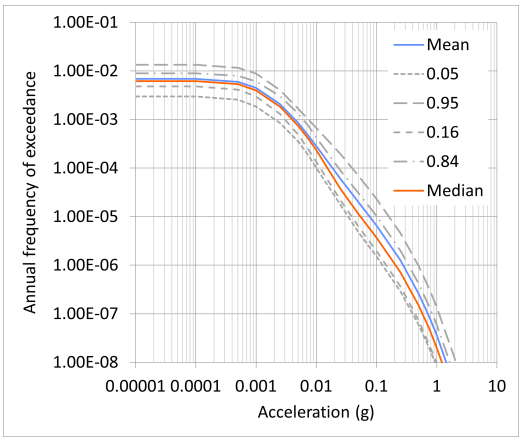

(c) 25 Hz

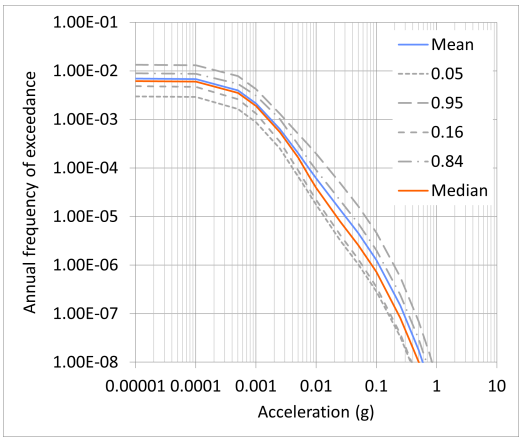

(d) 100 Hz

Figure D10: Olkiluoto mean, median, and 0.05, 0.16, 0.84, and 0.95 fractile hazard curves at different frequencies for the meso model.

Table D9: Olkiluoto mean UHRS values using the updated maximum magnitude.

Frequency (Hz)	SA at mean AFE 10^{-3} (g)	SA at mean AFE 10^{-4} (g)	SA at mean AFE 10^{-5} (g)	SA at mean AFE 10^{-6} (g)	SA at mean AFE 10^{-7} (g)	SA at mean AFE 10^{-8} (g)
0.10	0.00000	0.00004	0.00015	0.00041	0.00105	0.00222
0.13	0.00001	0.00007	0.00025	0.00073	0.00178	0.00382
0.20	0.00003	0.00018	0.00062	0.00160	0.00375	0.00798
0.25	0.00005	0.00028	0.00099	0.00250	0.00579	0.01214
0.33	0.00010	0.00051	0.00161	0.00419	0.00986	0.02115
0.40	0.00015	0.00075	0.00239	0.00603	0.01387	0.03015
0.50	0.00024	0.00121	0.00374	0.00942	0.02166	0.04709
0.67	0.00044	0.00201	0.00608	0.01498	0.03503	0.07668
1.00	0.00099	0.00409	0.01168	0.02876	0.06762	0.14566
1.33	0.00156	0.00638	0.01753	0.04378	0.10490	0.22844
2.00	0.00285	0.01056	0.02858	0.07204	0.17310	0.37234
2.50	0.00353	0.01276	0.03495	0.09056	0.22281	0.47760
3.33	0.00455	0.01584	0.04398	0.11681	0.29054	0.61628
4.00	0.00504	0.01737	0.04899	0.13371	0.33640	0.72011
5.00	0.00567	0.01985	0.05725	0.16114	0.40842	0.86368
10.00	0.00624	0.02394	0.07806	0.24985	0.64319	1.32678
13.30	0.00594	0.02392	0.08255	0.27437	0.72734	1.50983
25.00	0.00399	0.01762	0.06828	0.24286	0.63854	1.32080
33.30	0.00299	0.01328	0.05228	0.18684	0.50656	1.05401
50.00	0.00198	0.00891	0.03534	0.12696	0.33910	0.72212
100.00	0.00160	0.00701	0.02690	0.09698	0.25658	0.53602

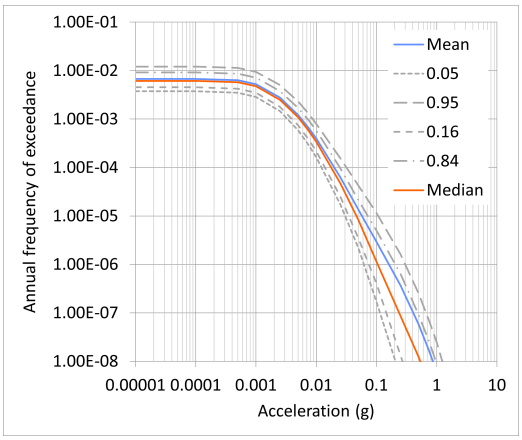

(a) 5 Hz

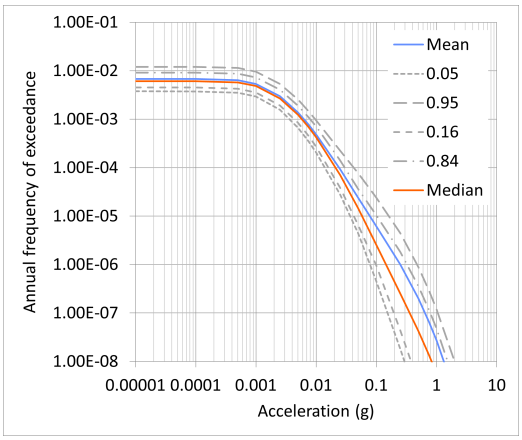

(b) 10 Hz

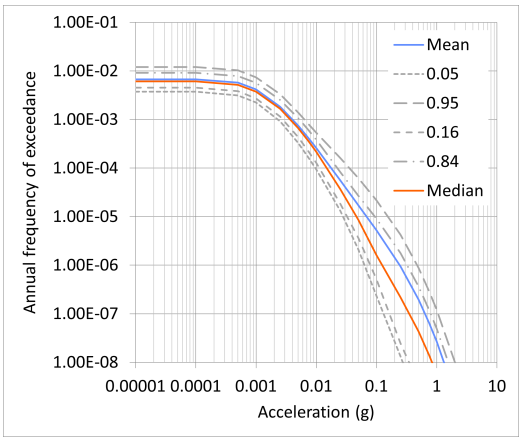

(c) 25 Hz

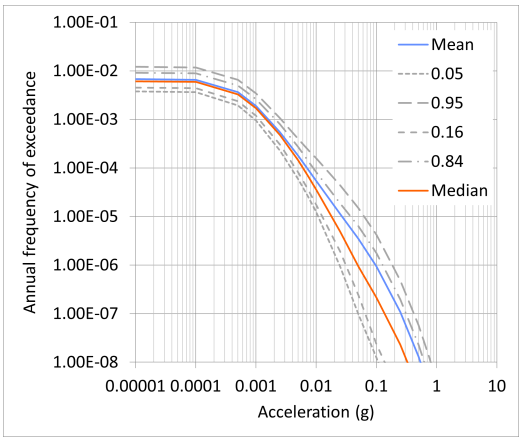

(d) 100 Hz

Figure D11: Olkiluoto mean, median, and 0.05, 0.16, 0.84, and 0.95 fractile hazard curves at different frequencies using the updated maximum magnitude.

D.3 Seismic Hazard Estimate with the Suggested Adaptation

This section presents the hazard estimates obtained using the suggested PSHA logic tree configuration introduced in Chapter 6, but without applying any subdivision of the Loviisa source zone. As before, the results are shown separately for the Loviisa and Olkiluoto sites.

For Loviisa, Figure D12 displays the mean hazard curves together with the 90 % confidence intervals (CIs) that represent the 0.05 and 0.95 fractiles. The corresponding results for Olkiluoto are shown in Figure D14. The resulting UHRS are provided in Figure D13 and Table D10 for Loviisa, and in Figure D15 and Table D11 for Olkiluoto.

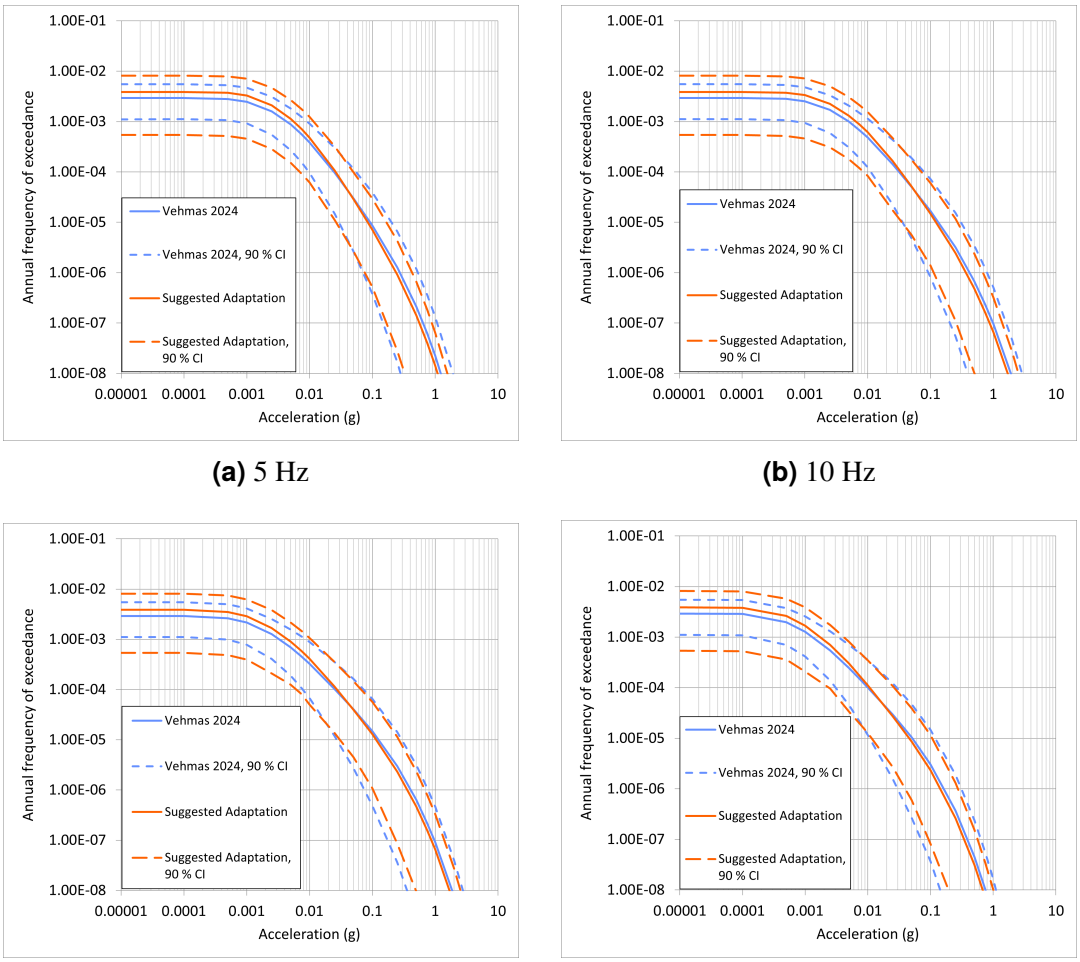

(a) 5 Hz

(b) 10 Hz

(c) 25 Hz

(d) 100 Hz

Figure D12: Loviisa mean hazard curves and their 90 % confidence intervals (0.05 and 0.95 fractiles) at different frequencies using the suggested adaptation without SSZ 10 subdivision. Results from Vehmas [9] are included for comparison.

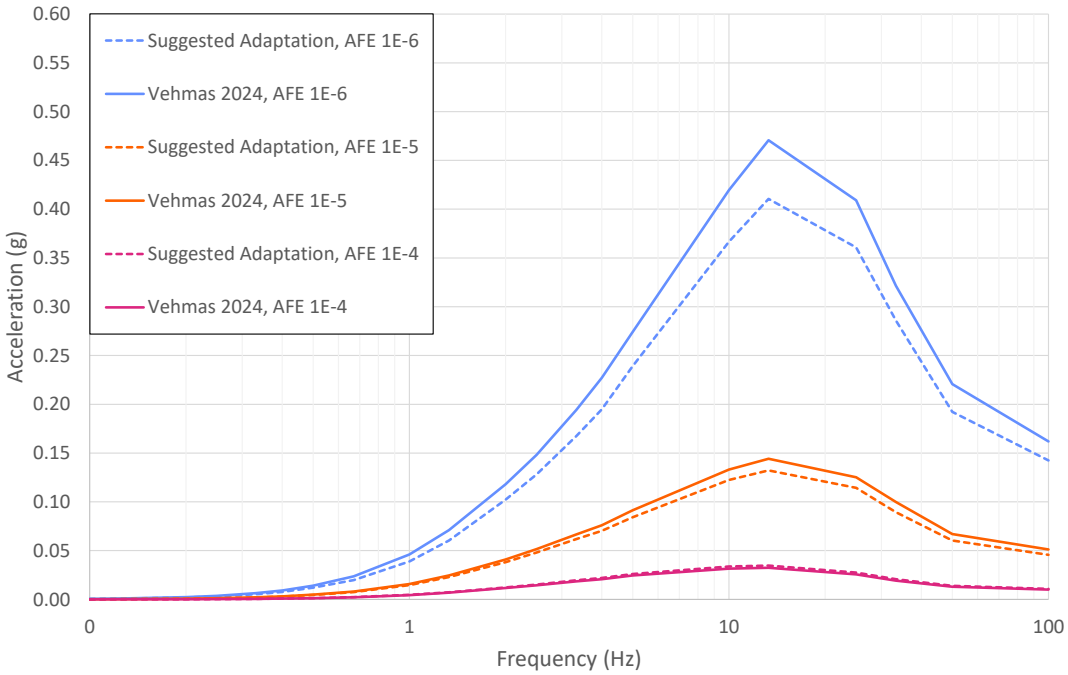

Figure D13: Loviisa mean UHRS at different AFEs using the suggested adaptation without SSZ 10 subdivision. The results of Vehmas [9] are shown for comparison.

Table D10: Loviisa mean UHRS values using the suggested adaptation without SSZ 10 subdivision.

Frequency (Hz)	SA at mean AFE 10^{-3} (g)	SA at mean AFE 10^{-4} (g)	SA at mean AFE 10^{-5} (g)	SA at mean AFE 10^{-6} (g)	SA at mean AFE 10^{-7} (g)	SA at mean AFE 10^{-8} (g)
0.10	0.00000	0.00004	0.00016	0.00049	0.00124	0.00276
0.13	0.00001	0.00008	0.00029	0.00087	0.00220	0.00484
0.20	0.00003	0.00018	0.00071	0.00194	0.00473	0.01017
0.25	0.00004	0.00030	0.00113	0.00306	0.00737	0.01544
0.33	0.00008	0.00055	0.00192	0.00530	0.01267	0.02768
0.40	0.00013	0.00082	0.00283	0.00767	0.01818	0.03932
0.50	0.00020	0.00131	0.00452	0.01200	0.02867	0.06111
0.67	0.00036	0.00225	0.00749	0.01971	0.04753	0.10157
1.00	0.00087	0.00467	0.01464	0.03889	0.09263	0.19060
1.33	0.00140	0.00737	0.02284	0.06037	0.14104	0.29493
2.00	0.00263	0.01231	0.03811	0.10215	0.23972	0.48553
2.50	0.00328	0.01523	0.04798	0.12813	0.30195	0.61080
3.33	0.00429	0.01959	0.06187	0.16748	0.39293	0.79005
4.00	0.00483	0.02202	0.07031	0.19486	0.46116	0.91823
5.00	0.00557	0.02595	0.08425	0.23918	0.55750	1.09209
10.00	0.00653	0.03368	0.12244	0.36673	0.87314	1.69651
13.30	0.00634	0.03467	0.13222	0.41052	0.99014	1.95758
25.00	0.00447	0.02740	0.11435	0.36080	0.86863	1.68984
33.30	0.00334	0.02066	0.08930	0.28579	0.68420	1.32138
50.00	0.00223	0.01386	0.06034	0.19227	0.46577	0.91700
100.00	0.00173	0.01073	0.04572	0.14238	0.34197	0.68022

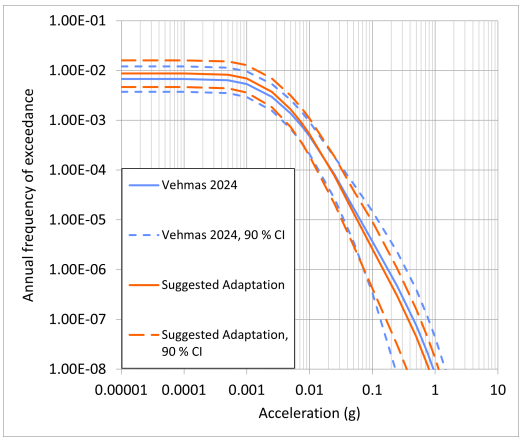

(a) 5 Hz

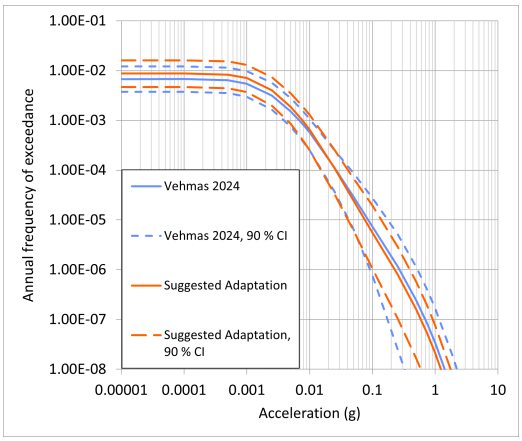

(b) 10 Hz

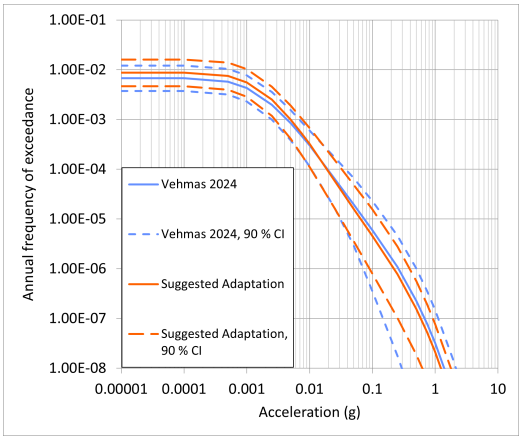

(c) 25 Hz

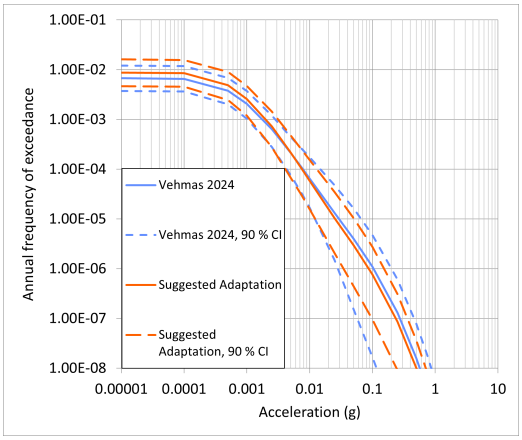

(d) 100 Hz

Figure D14: Olkiluoto mean hazard curves and their 90 % confidence intervals (0.05 and 0.95 fractiles) at different frequencies using the suggested adaptation without SSZ 10 subdivision. Results from Vehmas [9] are included for comparison.

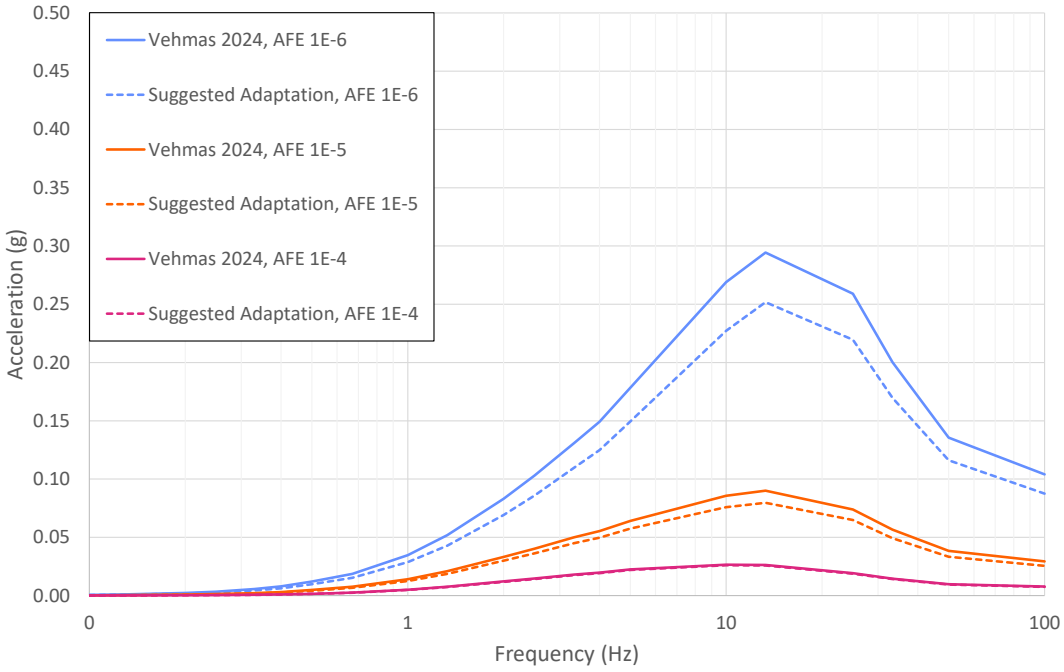

Figure D15: Olkiluoto mean UHRS at different AFEs using the suggested adaptation without SSZ 10 subdivision. The results of Vehmas [9] are shown for comparison.

Table D11: Olkiluoto mean UHRS values using the suggested adaptation without SSZ 10 subdivision.

Frequency (Hz)	SA at mean AFE 10^{-3} (g)	SA at mean AFE 10^{-4} (g)	SA at mean AFE 10^{-5} (g)	SA at mean AFE 10^{-6} (g)	SA at mean AFE 10^{-7} (g)	SA at mean AFE 10^{-8} (g)
0.10	0.00000	0.00005	0.00017	0.00046	0.00111	0.00224
0.13	0.00002	0.00009	0.00029	0.00080	0.00186	0.00379
0.20	0.00004	0.00021	0.00070	0.00171	0.00383	0.00774
0.25	0.00007	0.00035	0.00110	0.00266	0.00585	0.01165
0.33	0.00013	0.00061	0.00180	0.00441	0.00975	0.01975
0.40	0.00019	0.00090	0.00266	0.00630	0.01360	0.02804
0.50	0.00031	0.00142	0.00415	0.00978	0.02094	0.04313
0.67	0.00057	0.00239	0.00666	0.01523	0.03316	0.06943
1.00	0.00122	0.00478	0.01252	0.02866	0.06259	0.13166
1.33	0.00197	0.00735	0.01865	0.04287	0.09596	0.20433
2.00	0.00347	0.01181	0.02990	0.06912	0.15776	0.33771
2.50	0.00436	0.01422	0.03618	0.08575	0.20166	0.43195
3.33	0.00557	0.01761	0.04498	0.10966	0.26567	0.56487
4.00	0.00609	0.01929	0.04973	0.12484	0.30692	0.65882
5.00	0.00691	0.02199	0.05745	0.14954	0.37193	0.79682
10.00	0.00768	0.02604	0.07590	0.22719	0.59029	1.23495
13.30	0.00733	0.02589	0.07962	0.25176	0.66639	1.40360
25.00	0.00499	0.01878	0.06478	0.21960	0.58916	1.23644
33.30	0.00367	0.01412	0.04928	0.16960	0.46468	0.99066
50.00	0.00250	0.00949	0.03334	0.11608	0.31310	0.67184
100.00	0.00198	0.00752	0.02544	0.08742	0.23473	0.50108